Excitons and Polarons in resonant Auger decay processes

Von der Fakultät für Mathematik, Naturwissenschaften und Informatik
der Brandenburgischen Technischen Universität Cottbus

zur Erlangung des akademischen Grades
Doktor der Naturwissenschaften
(Dr. rer. nat.)
genehmigte Dissertation
vorgelegt von

Diplom-Physiker

Matthias Hermann Richter

geboren am 03.11.1984 in Hoyerswerda (Deutschland)

Gutachter:	Prof. Dr. rer. nat. habil. Dieter Schmeißer
Gutachter:	Juniorprof. Dr.-Ing. Marcus Bär
Gutachter:	Apl. Prof. Dr. habil. Ulrich Starke

Tag der mündlichen Prüfung: 24.01.2014

Kurzfassung

Im Rahmen dieser Arbeit wird die elektronische Struktur von organischen Halbleitern, Graphen und Übergangsmetall (TM)-Oxyden (Co-PI als Katalysator für die Wasserspaltung), unter Nutzung von Synchrotron-Strahlung basierter Spektroskopie, untersucht. Der Schwerpunkt liegt hierbei bei den exzitonischen und polaronischen Effekten. Für eine genaue Beschreibung der elektronischen Struktur dieser Materialien müssen auch Elektron-Phonon- und Elektron-Elektron-Wechselwirkungen, sowie Polarisation und exzitonische Effekte in Betracht gezogen werden. Von Exzitonen und Polaronen als lokalisierte Bandlückenzustände ist bekannt, dass diese die optischen Materialeigenschaften beeinflussen können. Dieser Einfluss kann im resonanten Auger Zerfall aufgedeckt werden.
Sogar in TM-Oxyden können Polaronen und Exzitonen als Konsequenz von einem Sauerstoff 2p nach TM3d Ladungstransfer beobachtet werden.

Hierfür sind die folgenden drei Materialklassen für die Untersuchungen des Einflusses von Exzitonen und Polaronen im resonanten Auger Zerfall ausgewählt worden.

Erstens wird die Existenz von lokalisierten polaronischen und exzitonischen Zuständen anhand von Poly(3-hexylthiophene-2,5-diyl) (rr-P3HT) und Phenyl-C61-butyric acid methyl ester (PCBM) untersucht, welche als Lichtabsorber in organischen Solarzellen eingesetzt werden. Die Existenz von 2D-Polaronen, Singulett-Exzitonen und Triplett-Exzitonen wird für rr-P3HT belegt, wohingegen für PCBM nur Singulett-Exzitonen beobachtet werden. Singulett-Exzitonen zeigen ihren Einfluss auf den resonanten Auger Zerfall durch einen kombinierten Spectator-Participator (S+P) Auger Zerfall im π*-Band.

Zweitens wird für eine ausführliche Diskussion der (S+P) Zerfälle hoch orientierter pyrolytischer Graphit (HOPG) untersucht. Für Graphen, als eine Monolage HOPG, in dem keine Van-der-Waals-Kräfte wirken, können weitere Kombinationen von Auger Zerfällen beobachtet werden: ein Doppel Spectator (S+S) und ein Doppel Spectator (S+S)* Auger-Gain Zerfall im π*-Band.

Drittens wird Co-PI (Kobaltoxyd-Verbindung) untersucht. Es handelt sich hierbei um ein TM-Oxyd welches als Katalysator für die Sauerstoffentwicklung in photoelektrochemischen Zellen verwendet wird. Selbst lokalisierte Exzitonen werden durch resonante Anregung eines Rumpfelektrons in einem selbst lokalisierten Lochzustand erzeugt und ermöglichen dadurch einen kombinierten Auger Zerfall (S+P).

Für jeden der neuartigen Auger Zerfallsprozesse {(S+P), (S+S) und (S+S)*} wird ein Zerfallsmodell vorgestellt.

Abstract

In the framework of this thesis synchrotron radiation spectroscopy is applied to study the electronic structure of organic semiconductors, of Graphene, and of transition metal (TM) oxide water splitting catalysts (Co-PI) with emphasis on excitonic and polaronic effects.

For a correct theoretical description of the electronic structure of these material classes electron-phonon and electron-electron coupling as well as polarization and excitonic effects have to be considered. Excitons and Polarons are localized in-gap states. They are known to affect the optical properties of the material. Their influence can also be revealed in the resonant Auger decay profile.

Even in TM-oxides Polarons and Excitons are observed as a consequence of an oxygen 2p to TM3d charge transfer.

Therefor, the following three material classes are chosen for the fundamental study of Excitons and Polarons in resonant Auger decay processes.

First, the existence of localized polaronic and excitonic states is investigated for regioregular-Poly(3-hexylthiophene-2,5-diyl) (rr-P3HT) and Phenyl-C61-butyric acid methyl ester (PCBM) used as a light absorber in organic solar cells. The existence of 2D-Polarons, singlet Exciton, and triplet Exciton is demonstrated for rr-P3HT whereas for PCBM only singlet Excitons are observed. Singlet Excitons show an influence on the resonant Auger decay by a combined spectator-participator (S+P) Auger decay in the π^*-band.

Second, for a more detailed study of the (S+P) decay Highly Ordered Pyrolytic Graphite (HOPG) is chosen. For Graphene as a single layer of HOPG without van der Waals force another combination of Auger decays can be observed: a double spectator Auger (S+S) and a double spectator Auger-Gain (S+S)* decay.

Third, Co-PI (cobalt oxide compound) is investigated. It is a TM-oxide catalyst used for the oxygen evolution reaction in photo-electrochemical cells. Self-trapped Excitons formed by resonant core electron excitation into self-trapped hole states give rise to a combined Auger decay process (S+P).

For all three novel Auger decay processes {(S+P), (S+S), and (S+S)*} a model is proposed.

Table of Contents

Introduction

Nowadays, organic semiconductors and Graphene are of interest for flexible electronics and high-speed transistor devices. The fundamental work on these two classes of materials led to the 2000 Nobel Prize in chemistry and 2010 Nobel Prize in Physics [GEI07], [HEE01].
These carbon thin films are known to exhibit localized states such as Polarons or Excitons which can be observed in X-ray absorption studies [BRA81], [PSI09], [ROB02].
Localized gap states cannot be described by Bloch wave functions. Polarization, electron-phonon, electron-electron, electron-phonon-electron, and excitonic effects have to be taken into account in order to describe the data properly. Standard DFT calculations (LDA, Norm-conservation pseudo potential, Plane-wave) have to be improved by Gutzwiller (GW) approximation and Bethe-Salpeter equation [CUD10], [WEI12], [WEI13]. Crystal local field effects, e-h interaction, e-e interaction, and charge transfer excitonic effects as many-body effects have to be included. Examples are calculations of Graphane (hydrated Graphene with a large band gap) [WEI12] and Graphene [LIA11], [YAN09] which include e-h interaction. Only with e-h interaction the prominent excitonic features are captured which give rise to absorption peaks at low excitation energies below the band gap. In Graphane the hole is localized on the C-C bonds whereas the electron is mainly localized over several lattice constants on top of the H-atoms [CUD10].

In Graphene, without e-h coupling the simulated absorption spectrum resembles a Gaussian distribution which peaks at the π-π* transition at the M-point of Graphene. With e-h coupling the spectra is red shifted and is described by a FANO type transition. This has also been shown by optical conductivity and transmission measurements [CHA11], [MAK11], [YAN09]. Remarkable is that the absorption limit for zero excitation energy approaches a finite value, which is defined as a multiple integer of $\pi\alpha$ (α is the fine structure constant) that is basically the inverse of the quantum resistivity h/e^2 [NAI08].

Consequences of Excitons and charge transfer (CT) states are that band gaps obtained from optical measurements (UV-Vis) do not resemble the valence band (VB)-conduction band (CB) transition. They rather probe VB-Polaron, VB-Exciton, or VB-CT transitions. These can be in the order of a few eV lower than the real VB-CB band gap.

In oxides, especially transition metal oxides, excitonic and polaronic effects also have to be considered. It was found that many wide band gap semiconductors exhibit n-type conductivity. P-type conductivity is in most cases difficult to achieve [JAN06], [JAN10], [POZ11]. The reason for this is the fact that the O2p holes are not highly mobile and delocalized over many lattice constants. They are trapped by local lattice distortions and can be referred to self-trapped holes or more general small Polarons [MCK12], [VARL12]. The lattice displacement and thus the localization of the self-trapped hole are in the order of one lattice constant. Self-trapped holes are stable if their energy is lower than the one of a delocalized mobile hole. O2p hole states can be created by an O2p to metal 3d charge transfer.

If an electron is coulombically attracted to the self-trapped hole even self-trapped Excitons can form.

Hence, under resonant excitation at the O1s resonance self-trapped Excitons can be formed in the presence of self-trapped holes. Without self-trapped holes the excited electron can only form a self-trapped electron.

As many-body effects have a huge influence on the optical properties in the UV-Vis region they also affect the X-ray absorption spectroscopy (XAS) at the core level threshold. Especially near the core level and ionization threshold the decay of the resonantly excited core level is highly influenced. Auger resonant Raman scattering shows a linear dispersion of the kinetic energy of the Auger electrons below the core level threshold. Small dips of the spectator Auger electron kinetic energy are observed at van Hove singularities [FOE02]. Post collision interaction, the interplay of a low-energy photoelectron with a high-energy Auger electron, blue shifts the kinetic energy of the spectator Auger electron. These effects are still noticeable up to 100 eV above threshold [COW00].

Ohno describes the effect of post collision interaction (PCI) before the ionization threshold in terms of localized metallic or CT gap states [OHN01]. This inherent PCI is discussed in this work in terms of the combined spectator-participator Auger decay involving localized excitonic or CT gap states.

The individual contributions of sp^2-, sp^3-hybridization, the existence of localized states like Polarons, Excitons, and CT states and their differences in the resonant behaviour of carbon films and oxides need to be comprehended. These are relevant for understanding the electronic properties of thin carbon films as well as transition metal (TM) oxides.

In this work the resonant behaviour of sp^2 hybridized systems (organic semiconductors and Graphene) is investigated. The focus is on the existence of localized in-gap states (Excitons and Polarons) that affect the optical (band gap) and electronic properties (conductivity, mobility, catalysis). The resonant Auger decay processes are highly influenced by these localized states. As a consequence combinations of multiple Auger decays are observed. By analysis of the resonant decay profile at the core level threshold the interlayer interaction, the substrate hybridization, the substrate screening, and the properties of pristine Graphene as well as organic semiconductors can be deduced. Resonant Auger decay combinations are also observed in oxides because of the existence of self trapped hole in-gap states. These states are characterized for the oxygen evolution reaction catalyst Co-PI.

In Chapter 1 the investigated sp^2 hybridized carbon systems and TM-oxide (Co-PI) will be introduced and a description of the charge carriers in organic semiconductors will be given. Chapter 2 deals with the experimental setup, the applied techniques of resonant photoemission and X-Ray absorption spectroscopy, the background of the resonant excitation process (Kramers-Heisenberg) and Auger decay processes, as well as the sample preparation. This is followed in Chapter 3 by the results of Poly(3-hexylthiophene-2,5-diyl) (P3HT), Phenyl-C61-butyric acid methyl ester (PCBM), Graphene and Co-PI. These results will be discussed in Chapter 4 in terms of charge carriers in organic semiconductors (Excitons and Polarons). Their lifetime will be evaluated and as a consequence the concept of the different combinations of Auger decays at the carbon resonance will be discussed. Models for each of the new combined (S+P), (S+S), and (S+S)* Auger decay processes will be introduced. On this basis the resonant behaviour of the oxygen evolution reaction catalysts Co-PI will be described. The new combined Auger decay processes and systematic findings of the Auger decay at resonance are used to identify CT states and the spin state of the catalyst by a parallel resonant photoemission (resPES) at the Co2p and O1s edge. An overall conclusion follows in Chapter 5.

Chapter 1 Materials

In this chapter the three material systems organic semiconductors, Graphene, and the oxygen evolution reaction (OER) catalyst Co-PI are briefly introduced. The focus will be on the respective charge carriers i.e. Excitons and Polarons. Their existence and properties are of particular interest for the later discussion on multiple Auger decay processes at the core level threshold.

1.1 Organic Semiconductors

P3HT and PCBM are widely applied in organic solar cells and organic field effect transistors. P3HT is a thiophene. Its carbon backbone is similar to polyacetylene (all-cis-polyacetylene), which is conductive. This observation led to the 2000 Nobel Prize in chemistry awarded to Alan J. Heeger, Alan G. MacDiarmid, and Hideki Shirakawa for their work on organic semiconductors in 1977 [CHI77], [HEE01].

Doping, Excitons, and Polarons are well-established properties. Interchain and inter-lamellae interaction are accepted properties, which are necessary for a high conductivity not only along a single chain but also through the complete organic crystal.

The Fullerene PCBM is a 0D-Material that can be build up by wrapping up Graphene, the 2D building block for many sp^2 bonded materials. Graphene can also be stacked into 3D Highly Ordered Pyrolytic Graphite (HOPG) a reference system with only sp^2 character, which can be easily cleaved to prepare a clean surface.

Depending on the chemical structure organic materials can exhibit insulating, semiconducting or even metallic behaviour. The special case of Graphene, which exhibits ballistic conduction, is discussed in Chapter 1.2.

In order to obtain conducting organic materials the carbon atoms have to be sp^2 hybridized (Figure 1.1). Two C2p (p_x, p_y) orbitals and the C2s orbital form three sp^2 orbitals (σ-orbitals). One σ-orbital and the single C2p_z orbital (π-orbital) take part in the C=C bonding. The structure is held together by the trigonal planar σ-orbitals. The one remaining electron per carbon atom in the p_z orbital is delocalized in the π-system made up by the overlapping p_z orbitals of neighbouring atoms, which are perpendicular to the σ-system. Due to the delocalized π-system and weak interchain interaction the conjugated polymers are able to conduct charges.

A metallic state is not formed in C=C bonding due to electron-phonon coupling. A structure with equal bond length is not stable against k_F (Fermi wave vector) phonons and the structure will form long and short bonds (dimerization) [PEI55].

In fact the π and σ states split into occupied π- and σ-bands and unoccupied π*- and σ*-bands with a band gap in between (Peierls distortion). In the Su, Schrieffer and Heeger (SSH) model the band gap is given by the electron-phonon coupling α and the dimerization distance u_0 (difference between long and short bonds) [HEE88], [SU79]:

$$E_{gap} = 8 \cdot \alpha \cdot u_0 \tag{1}$$

Organic semiconductors can be classified into two categories: conjugated polymers (e.g. polythiophene) and macromolecules (e.g. fullerenes).

Functionalization by additional side groups is used to increase e.g. solubility, light absorption efficiency, and sensitivity or modifies the electronic properties.

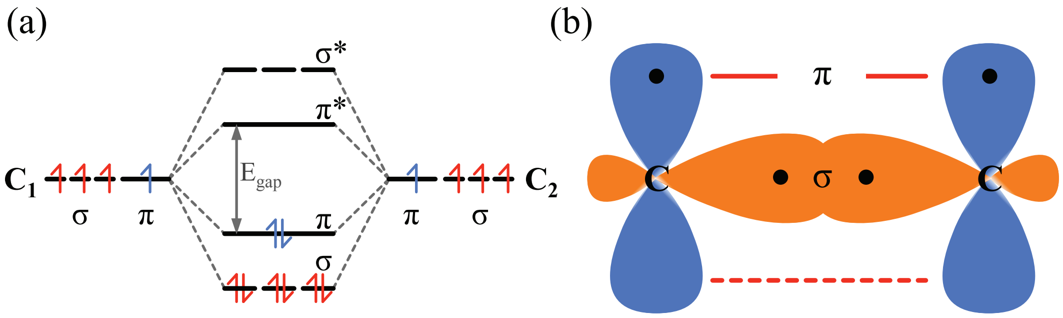

Figure 1.1: *Bonding of sp2 hybridized carbon atoms develop molecular bands. The π-band originates from the Highest Occupied Molecular Orbital (HOMO) and the π*-band originates from the Lowest Unoccupied Molecular Orbital (LUMO) with a band gap in between due to Peierls distortion (a). π- and σ-bonds of a simple conjugated electron-system (b). The Figures were reproduced from [BRU08].*

1.1.1 P3HT

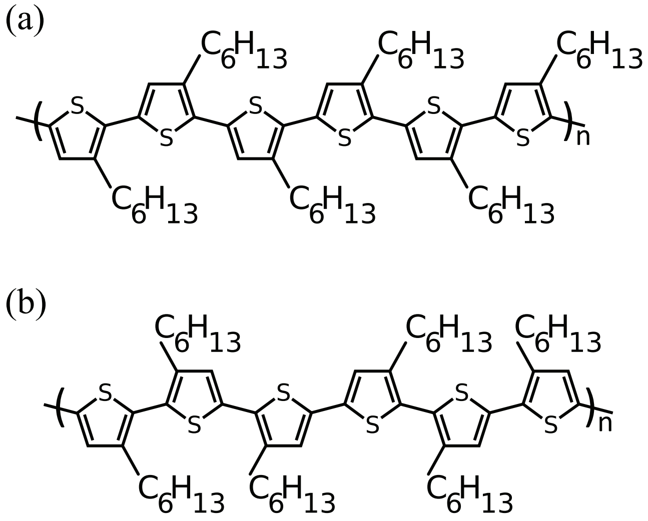

Figure 1.2: *Schematic structure of (a) regioregular (rr)- and (b) regiorandom (rra)-P3HT.*

In organic electronics, especially organic solar cells, poly(3-hexylthiophene) is an ideal p-type semiconductor and a widely used conjugated polymer which exists in two main phases (Figure 1.2) [DEN09], [MA05], [SET08], [SHE07]. Regioregular-P3HT (rr-P3HT) is noted for its low photoluminescence and high carrier mobility in contrast to regiorandom-P3HT (rra-P3HT). These properties are assigned to the formation of a self-organized nanostructure due to the regio-regularity (Figure 1.3) [SHE07]. The rr-P3HT 1D chains are separated by a inter-chain distance of A= 0.38 nm and the 2D lamellae are separated by 1.64 nm (B) (Figure 1.3) [MA05].

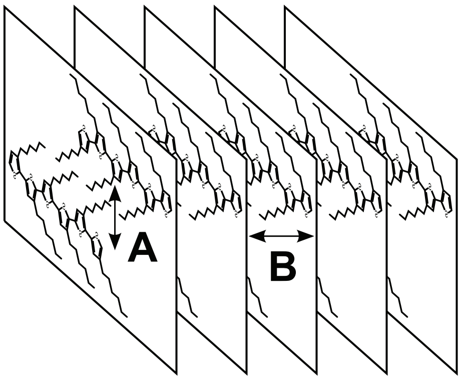

Figure 1.3: *Lamellae structure of rr-P3HT with the inter-chain distance A and the inter-lamellae distance B.*

1.1.2 PCBM

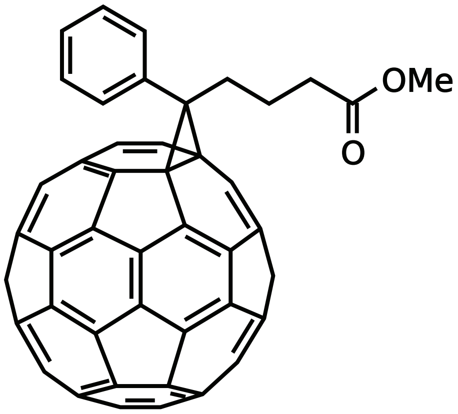

Figure 1.4: Schematic structure of (6,6)-Phenyl C61 butyric acid methyl ester.

Fullerenes and their derivatives are widely used as electron acceptors in organic solar cell applications because of their high electron affinity. In particular, (6,6)-Phenyl C_{61} butyric acid methyl ester is a well-known and extensively applied candidate (Figure 1.4). In the field of organic bulk heterojunction solar cells PCBM is commonly used as the electron acceptor [CHI10]. In organic field effect transistors (OFET) Fullerenes function as electron transporting semiconductor (n-channel) [ANT06].

Fullerenes are also extensively investigated for ultra low-k applications because of their ability to form porous frameworks [BRO10], [KLO12a], [KLO12b]. Replacing C_{60} with the better soluble derivative PCBM showed positive effects on the reduction of the dielectric constant [KLO12a], [KLO12b].

In Bioscience Fullerenes are used e.g. as antioxidants because of their ability to add and remove electrons without any significant energy cost and for slow-release drug delivery [QUI08], [ZAK05].

In a recent publication the influence of functional groups onto the π-system of fullerenes was investigated [Frie11]. The π states are drastically reduced in consequence of the addition of functional OH groups ($C_{60}OH_x$, x= 20-28).

1.1.3 Charge carriers in organic semiconductors

In contrast to classical inorganic semiconductors (e.g. Si, Ge, GaAs) free electrons or holes do not exist in organic semiconductors as charge carriers, which can move freely through the material. In fact a respectable number of quasiparticles do exist.

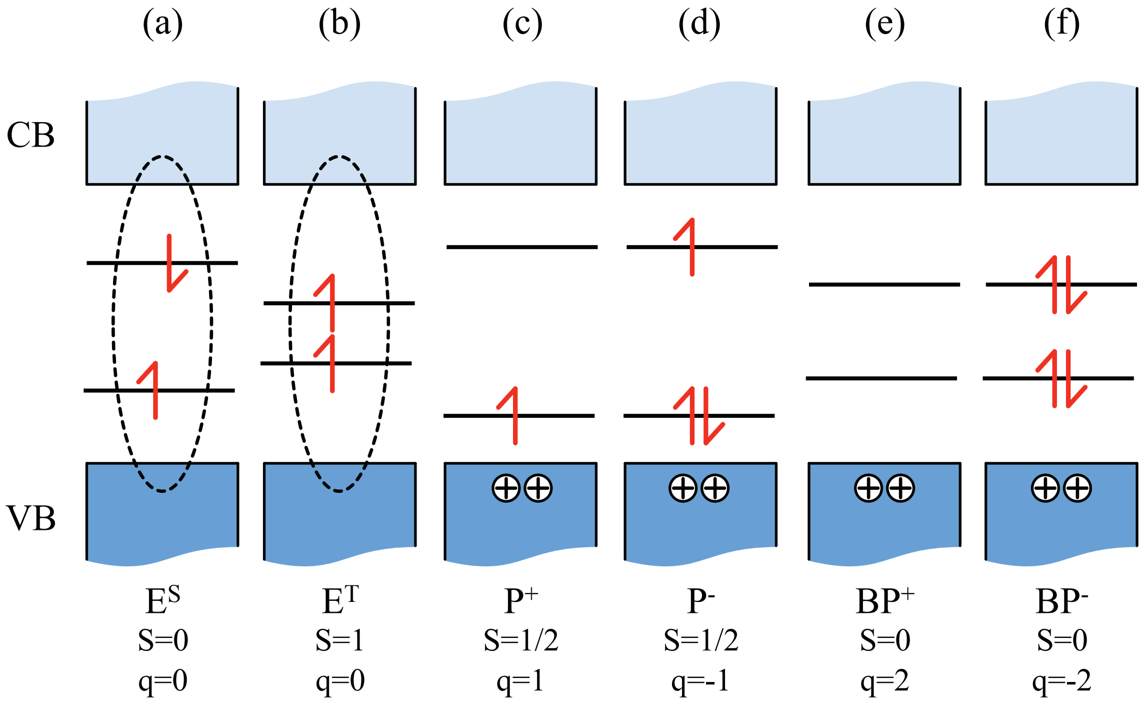

Figure 1.5: *Electronic energy-level diagrams of singlet Exciton (a), triplet Exciton (b), positive Polaron (c), negative Polaron (d), positive Bipolaron (e), and negative Bipolaron (f).*

1.1.3.1 Exciton

Photo-excitation of organic semiconductors does not lead to free charge carriers at first. Upon photo-excitation a bound localized electron hole pair is formed which can freely move through the organic material. This pair of an electron and a hole is bound by Coulomb attraction and has opposite spin (Figure 1.5a). The formation of an Exciton is accompanied by a modification in the local polymer geometry.

Depending on the degree of localization it will be distinguished between a Wannier-Mott Exciton (r= 4 – 10 nm; $E_{Bind}\approx 1$ eV) and a Frenkel Exciton (r < 0.5 nm; $E_{Bind}\approx 0.1$ eV). Whether a Wannier-Mott or Frenkel Exciton will be formed depends on the permittivity ε of the material, which defines the coulomb interaction U.

$$U = \frac{1}{4\pi\varepsilon}\frac{Q}{r} \tag{2}$$

Hence, in organic materials most of the photo-excitations lead to Frenkel type Excitons due to a small ε.

Equation 3 can calculate the binding energy of an Exciton in correspondents to the hydrogen-like atom with μ as the reduced effective mass.

$$E_{bind} = \mu \cdot 13.6\ \mathrm{eV}/\varepsilon^2; \quad \mu \propto \left[\frac{d^2E}{dk^2}\right]^{-1} \tag{3}$$

Excitons in solids are only accessible at low temperatures as their binding energy is in the order of $\frac{1}{10}kT$ (T= 300 K), for instance in InP. They are considerable smeared out at room temperatures and thus hardly are noticeable [TUR64].

In contrast, Excitons in organic semiconductors have a binding energy of about 0.5 eV for the singlet excitonic state and are thus clearly visible even at room temperatures. Triplet Excitons (Figure 1.5b) have even higher binding energies in the range up to 2 eV (see Chapter 4.1.1). They are more localized than their counterparts in inorganic crystals.

Localized singlet Excitons (Figure 1.5a) can dissociate at boundaries, interface defects, or virtual Polarons [Mue12a] into Polarons. A competing process is the relaxation into a triplet excitonic state by intersystem crossing (Figure 1.5b) [KOE09]. Triplet Excitons have a longer lifetime than singlet Excitons. Still organic solar cells based on singlet Excitons are up to now more efficient due to higher dissociation barrier for triplet Excitons which wastes a fraction of the collected solar energy.

Core-hole excitonic effects (the resonantly excited core electron is still coulomb bound to its core hole) are of particular importance when referencing XAS measurements to the Fermi level by using the core level binding energy. Excitonic effects can red shift the XAS spectrum by several eV due to Coulomb interaction. This fact has to be kept in mind when referencing XAS spectra to the Fermi energy. ResPES diagrams have the special feature to estimate the particular influence of core-hole Excitons on the XAS spectrum (see Chapter 2.3.4).

In case of resonant excitation the excited electron can also bind to a valence hole that is stabilized by local polarization. In this case the core Exciton is replaced by a highly localized

Exciton. This reflected in its high lifetime and the excitonic shift in XAS can be neglected (see Chapter 2.3.4).

In polar systems Excitons can be conceived as a combination of a negative and a positive Polaron, which are interacting with each other. This is especially of importance for organic solar cells were Excitons are primarily formed upon light absorption and need to be dissociated into two Polarons with opposite charge in order to contribute to the photocurrent [Mue12a].

1.1.3.2 Polarons and Bipolarons

Polarons and Bipolarons are established charge carriers in organic semiconductors [BRE85], [BRE87], [NOW89]. They are formed by adding or removing charges from or to the π-system and are stabilized by electronic and geometric relaxation along the polymer chain. These are self-localized electrons or holes together with their self-induced polarization (e-ph coupling).

From the interaction between two electrons or holes via Coulomb force and e-ph-e interaction two Polarons or a Bipolaron state could arise. The latter is a possible state for High-T_C superconductors because of its analogy to Cooper-pairs [MIC90].

Polarons cause two energy levels to appear within the electronic band gap (Figure 1.5c, d). They carry a single charge and can merge along the chain to form 1D-Bipolarons, which carry a double charge (Figure 1.5e, f). For high concentration of Polarons the localized levels will evolve into broad bands [BAE90].

Small Polarons are of particular interest for transition metal oxides. Here an electron or hole is trapped by a self-induced lattice displacement, which is in the order of one lattice constant. These are also called self-trapped holes (STH) or self-trapped electrons (STE) [VARL12]. The stability of STH depends on the total energy of localized holes and delocalized holes. STHs are stable if their energy is lower than that of a delocalized hole. An excited electron trapped by a STH is considered as a self-trapped Exciton (STX).

STHs, STEs, and STXs are identified in this study by a FANO transition (Chapter 2.3.5) and CT states {(S+P) Auger decay} (Chapter 1.3.1) in resonant photoemission diagrams at the O1s edge.

1.1.3.3 2D-Polarons

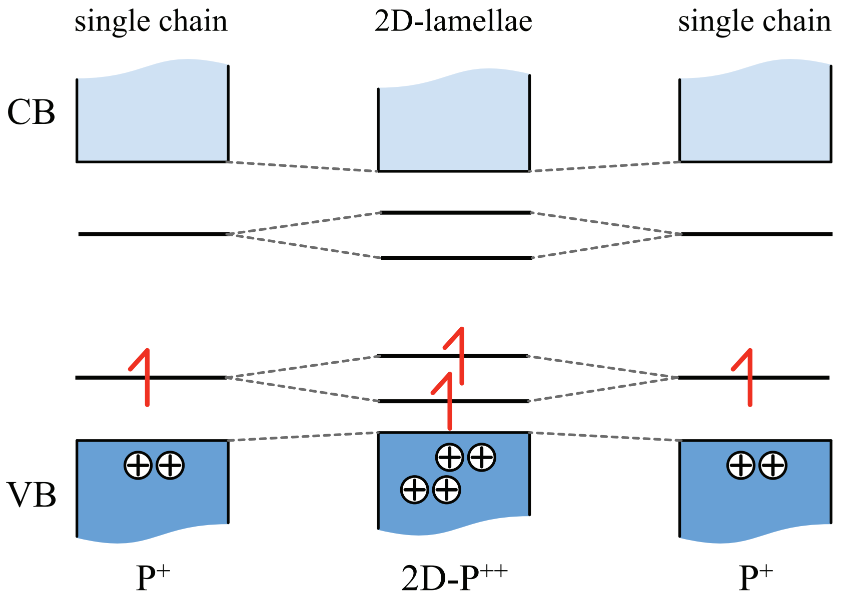

Figure 1.6: *Electronic energy-level diagram of a 2D-Polaron. The two positive Polarons on two neighbouring polymer chains can overlap and create a two dimensional Polaron.*

2D-Polarons form from the polaronic energy levels of two cofacial oligomers delocalized over two adjacent lamellas (Figure 1.6). This interaction leads to a splitting of the two 1D-Polaron levels into four levels within the band gap [BEL01]. They are observed in optical data and confirmed by theoretical studies for poly(para-phenylenevinylene) [BEL01].

The concept of 2D-Polarons can also be applied for P3HT because of a similar structural configuration in its quasi-crystalline domains [BEL01], [PSI09]. Several groups have observed such additional optical absorption features of 2D-Polarons in rr-P3HT films (lamellae structure), while they are absent in rra-P3HT, isolated polymer chains or disordered rr-P3HT films [BEL01], [JIA02], [OST00], [OST01].

1.1.3.4 Doping

Very early it was recognized that the conductivity of organic semiconductors could be increased by several orders of magnitude if they are doped [CHI77]. Doping of organic semiconductors differs from inorganic crystals as no lattice atoms are substituted but occurs via charge transfer reaction from a counter-ion.

This can either be done chemically, electrochemically or photochemically (organic solar cells). Organic semiconductors can be even doped by a charge transfer to the substrate [XU09]. Oxidation or reduction of the organic material will result in p- or n-doping, respectively.

E.g. the conductivity of trans-$[CH]_n$ can be increased by oxidation with AsF_5 from $10^{-5}\,\Omega^{-1}cm^{-1}$ to $220\,\Omega^{-1}cm^{-1}$. Reduction by NH_3 reduces the conductivity to $10^{-9}\,\Omega^{-1}cm^{-1}$ [CHI77].

The oxidation removes electrons from the π-orbitals of the conjugated polymer whereas the reduction adds additional electrons. The achievable doping percentage of the polymer is limited by the fact that only electrons can be removed or added to π_Z-orbitals until they are empty or full, respectively. Further doping will also affect the σ-orbitals and results in broken C=C bonds.

1.2 HOPG and Graphene

The interests of physicists, chemists, and material engineers in Graphene and Graphene like materials demonstrate the wide field of carbon-based materials, which has grown in the last couple of years [GEI07], [GEI12].

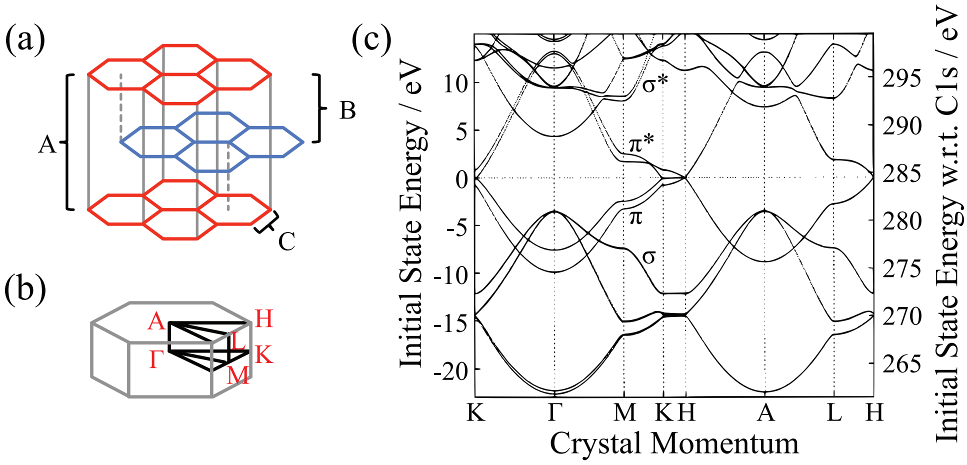

Figure 1.7: *Schematic structure of the lattice of HOPG (A= 6.7 Å; B= 3.35 Å; C= 1.42 Å) [ROB91] (a), the Brillouin zone of HOPG (b), and the corresponding band diagram of HOPG (c). The band diagram (c) was modified from [CAR99], [CAR00].*

Highly Oriented Pyrolytic Graphite is a semimetal and has only sp^2 hybridization because of its planar conjugated structure. HOPG is made out of stacks of Graphene layers that are weakly coupled by van der Waals forces (Figure 1.7a).

Therefore it resembles the 2-dimensional band structure of Graphene except some band dispersions along $\overline{\Gamma A}$, $\overline{KH}$, and $\overline{ML}$ directions (Figure 1.7c and Figure 1.8c). Deviations from this ideal 2-dimensional system however occur, as a high surface planarity with large terraces is not obtained by the fresh surface preparation by the scotch tape method [GEI07]. Also, step bunching, pinholes, and bubbles are visible in atomic force microscopy (AFM) studies of the HOPG surfaces [KAM08], [NIC03].

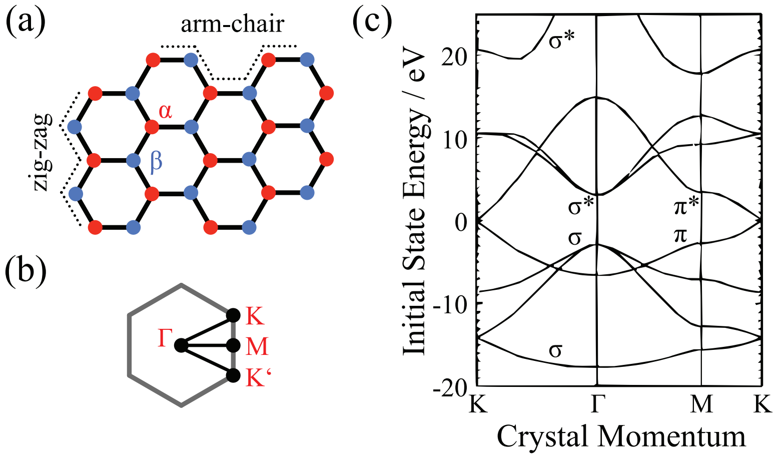

Figure 1.8: *Schematic structure of the honeycomb lattice of Graphene (sub-lattices α and β) (a), the Brillouin zone of Graphene (b), and the corresponding band diagram of Graphene (c). The band diagram (c) was modified from [SAI98].*

Graphene (2D) is the building block of various carbon materials: HOPG (3D), carbon nanotubes (1D), and Fullerenes (0D) [GEI07].

Graphene's ballistic conduction, mechanical strength, elasticity, impermeability, transparency, and thermal conductivity open a wide field for potential new applications [CAS09]. Indeed, a single layer sheet of HOPG (Graphene) represents a material that once could replace Si in many areas of communication technologies.

Graphene's extraordinary properties are given by its sp^2 hybridization. The sp^2 hybridization induces a hexagonal planar structure with two equivalent sub-lattices α and β (Figure 1.8a). The σ-bonds are responsible for robustness and the half filled π-bonds for the conductivity of Graphene. The band structure can be quite accurately described by the tight binding approximation [SAI98]. Ab initio calculation including wave function overlap, first, second, and third nearest neighbour interaction produce a more accurate description of the band dispersion of Graphene [REI02].

However, Graphene has a peculiarity at the K-point where π- and π*-band meet each other (Dirac point). The zero-gap is due to the fact that the involved electrons are from different sub-lattices. For Graphene the π- and π*-band exhibit a linear dispersion at the K-point as a result of the periodic potential of the honeycomb lattice. The linear dispersion can be described by massless Dirac-Fermions, which in consequence implies that an infinite conductivity σ and mobility μ can be expected: $\sigma = ne\mu \propto \frac{1}{m}$.

A fundamental understanding of the electronic processes that give rise to the unique properties of these class of materials is necessary in order to obtain high quality films [GEI07].

For integrated circuits, especially for transistors, p-doping, n-doping, and contacts to Graphene become necessary. A key question is how to create an electronic contact to the Graphene sheet without destroying its free carrier properties. Direct contact of Graphene with metals or highly doped semiconductors could either introduce screening effects or even open a band gap. The hybridization of Graphene π–states with metal d- and s- states could cause a pinning of the π–cloud to the metal substrate [MIT11], [VAN10], [VAR08].

It is an analytical challenge for these films to determine parameters such as the fraction of sp^3 in relation to sp^2 hybridization [ROB02], the amount of C-H bonds [ROB02], the size of Graphene-like flakes or the relative content of structural defect sites. More general it may be discussed whether their properties are determined by the extended π-system (Bloch wave function) or by localized states (molecular orbital picture). Furthermore, carbon thin films are known to exhibit localized states such as Polarons or Excitons as possible to detect by X-ray absorption studies [BRA81], [PSI09], [ROB02].

Recent absorption measurements and calculations on the optical response of Graphene and Graphite showed strong excitonic effects [CHA11], [MAK11], [YAN09].

Excitons are found to give rise to a new prominent peak near 4.5 to 4.9 eV. It is red-shifted and shows a different line shape than interband transitions at the π-band saddle point at the M-point in the Brillouin zone (Figure 1.8c). The experimental data can be well described by a FANO type transition [FAN66]. The binding energy of the Exciton extracted from the data is the difference of the resonance energy (Exciton energy) to the energy of the van Hove singularity (inter-band transition). It is in the range of 420 meV for monolayer Graphene and 270 meV for bilayer Graphene [CHA11]. This indicates that there is a dependency of the binding energy on the number of Graphene layers N. The net energy of the Exciton only shows a slight dependence on N because of effective cancelation of repulsive e-e and attractive e-h Coulomb interaction. From Graphene to Graphite it is only shifted by about 0.1-0.2 eV to lower energies [MAK11]. On the other hand the position of the van Hove singularity is lowered by interlayer interactions, thus drastically decreasing the binding energy of the Exciton (compare Figure 1.7c and Figure 1.8c).

By applied uniaxial strain the π- and π*-symmetry can be broken. Depending on the polarization direction a single or double excitonic peak can be observed with increased e-h interaction [LIA11].

A very detailed description about Graphene can be found in [BAT12], [GEI07], [RIE10].

1.3 OER catalysts

Solar hydrogen will be the key for the realization of a number of related renewable fuel production processes, such as hydrodeoxygenation of biomass into fuels and chemicals, or the reduction of CO_2 into methanol or other carbonaceous fuels [NEW12]. An important step for such applications is the availability of catalysts that enable water oxidation at potentials close to the thermodynamic limit.

Transition metal composites are candidates for cheap and efficient catalysts for the oxygen evolution reaction [GAR11], [SUB12], [WAN05].

Especially the complex OER limits the efficiency of photocatalytic cells. Recently cobalt-based catalysts (Co-PI, PI = electrodeposited from pH 7 phosphate electrolyte) have been introduced by the Nocera group which are promising candidates for OER because of their stability and reasonable efficiency for the OER at neutral pH [ESS11], [KAN08a], [KAN08b], [REE11], [SUR09].

In addition, there is particular challenge in the understanding of the basic mechanism during the photo catalytic reaction by the structural similarity to the Mn based Photosystem II active centrum in natural photosynthesis [KAN10], [MUK12], [RIS09b].

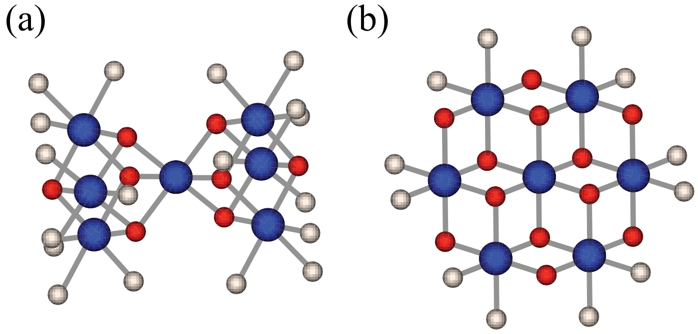

Figure 1.9: *Structural models of Co-PI: corner-sharing cubane model (a) and edge-sharing molecular cobaltate cluster (MCC) model (b). Cobalt atoms are shown in blue, oxygen atoms in red, and oxygen ligands (including water,*

hydroxide, and phosphate) in white. The Figures were reproduced from [KAN10].

The structure and valency was revealed by Extended X-ray Absorption Fine Structure (EXAFS) investigations for thin surface and thick bulk Co catalyst layers [KAN10], [RIS09b]. Two possible structural motifs for the cobalt catalysts could be identified. One are corner-sharing cubane clusters $\{Co_x(\mu\text{-}O)_y$ units$\}$ (Figure 1.9a) [RIS09b]. The other possible configuration is based on edge-sharing CoO_6 octahedra (Figure 1.9b) [KAN10]. In both cases the valency of Cobalt deduced from the position of the Co1s edge within the EXAFS data is greater or equal to 3+. Only for ultrathin layers the catalyst is reduced to Co^{2+} [KAN10].

In catalysis the knowledge of the particular oxidation state of the active metal ions certainly is of importance. In addition also the spin state plays a significant role as reported by recent theoretical and experimental studies [BUC04].

The spin and oxidation state of Co-PI catalysts is already investigated by several groups. X- and Q-band electron paramagnetic resonance (EPR) measurements indicate a low spin Co^{3+} for Co-PI [MCA10], [MCA11]. In X-ray absorption studies also a Co^{3+} state is reported [KAN10], [RIS09a], [RIS09b] to exist in bulk layers of Co-PI which are attributed to be more active and stable due to their larger Co-PI clusters [KAN10], [SUR10].

The particular OER mechanism involving Co-PI was studied by electro kinetic and ^{18}O isotope experiments by the Nocera group [SUR10]. A possible proton-coupled electron transfer reaction for the catalysis of the OER by Co-PI was proposed by Surendranath et al. and is given in Figure 1.10 [SUR10].

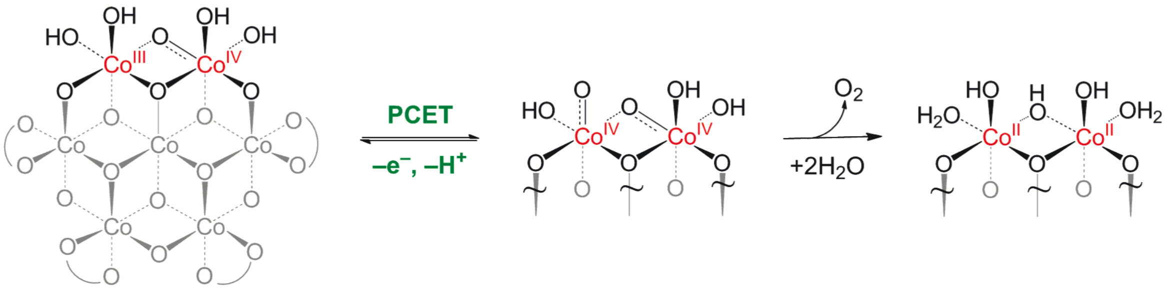

Figure 1.10: *A possible proton-coupled electron transfer reaction for the catalysis of the OER by Co-PI. The Figure was taken from [SUR10].*

1.3.1 Charge transfer

In transition metal oxides the excitation of a ligand electron from an oxygen 2p to the transition metal ion 3d state is described by the energy Δ, the charge-transfer energy. The other possibility is the excitation of a TM3d electron of one ion and electron transfer to another transition metal ion defined by U_{dd}, the correlation energy between 3d electrons.

In case of $U_{dd}<\Delta$ the TM-oxide is a Mott-Hubbard insulator and for $U_{dd}>\Delta$ it is considered to be a charge transfer insulator.

In the framework of this work the charge transfer process is of importance denoted in the following as $3d^{n+1}L$ with a one-electron transfer from the O2p (L) valence state to an empty transition metal 3d state. In general, such CT states are stabilized by the strong Coulomb interaction between the metal ion and the oxygen ligand. They also have a weak but significant hybridization between the occupied TM3d states and the O2p states from the VB.

All of these facts require sophisticated theoretical models for their description [OKA92a], [OKA92b]. In a more recent calculation such states are considered as self-trapping electron and hole polaronic states [MCK12], [VARL12].

Chapter 2 Experimental basics and details

In this chapter the basics of the utilized techniques are described. More details on this topic can be found in [STO03] and [HUE03]. A short description of the experimental setup at the synchrotron BESSY II is included as well as a comment on the preparation of the samples.

2.1 X-ray photoelectron spectroscopy (XPS)

Photoemission probes the occupied density of states. When matter is excited by X-rays with the proper energy electrons from core levels and valence band states will be excited into the vacuum where they can be described as free electrons. The kinetic energy of these electrons with reference to the vacuum level will be analysed by an electron analyser and quantified by the electron detector. The kinetic and binding energies of the electron have the following relation:

$$\hbar\omega = E_{\mathrm{Kin}} + \left|E_{\mathrm{Bind}}\right| + \phi_{\mathrm{Sample}} \qquad (4)$$

With respect to Koopmans' Theorem the excitation of one electron does not induce a change in the energies of the remaining electrons [KOO34]. Hence, photoelectron spectroscopy (PES) spectra can then be interpreted as the occupied density of states where PES is a one-electron process.

As the work function (the energy difference between vacuum level and Fermi energy) of the individual material under investigation is not always known the Fermi energy is used as point zero instead of the vacuum level:

$$\hbar\omega = E_{\mathrm{Kin}} + \left|E_{\mathrm{Bind}}\right| \qquad (5)$$

The binding energy of the electrons depends not only on their particular core level or valence band state but also on the chemical environment (next neighbour) of the atom (ΔE_{Chem}), the next but one neighbour – influence of the lattice (ΔE_{Mad}), and the relaxation and/or screening of the core hole – multi electron effects ($\Delta E_{\mathrm{Relax}}$):

$$E_{\mathrm{Bind}} = E_{\mathrm{Atomic\text{-}BE}} + \Delta E_{\mathrm{Chem}} + \Delta E_{\mathrm{Mad}} + \Delta E_{\mathrm{Relax}} \tag{6}$$

The oxidation or reduction of an atom removes or adds electrons to valence band states (complete or partial charge transfer), respectively. After excitation the remaining hole is screened less effectively for oxidized atoms and the binding energy increases. For reduced atoms it is the other way around; here the higher effective core hole screening decreases the binding energy.

On the other hand final states effects also shift the binding energy (e.g. spin-spin and spin-orbit coupling) and lead to a splitting of the atomic lines. The most prominent candidate is the spin-orbit coupling. As the spin of s can be parallel (lower binding energy) or antiparallel (higher binding energy) to the angular momentum l two states are possible, $j = l + s$ and $j = l - s$. The intensity ratio corresponds to the multiplicity $M = 2J + 1$, for example we have for p-orbitals a doublet of $p_{1/2}$ and $p_{3/2}$ with an intensity ratio of 1:2. The energy splitting of both emission lines depends on the electron interaction and increases with n and l.

2.1.1 Stoichiometry

PES can also be used to determine the specific atomic ratio of a sample. Due to different photoionization cross sections σ, inelastic mean free path λ, and electron transmission function T of the analyser the peak intensity I_X of the individual atomic lines have to be weighted by an atomic sensitivity factor ASF_X which includes these corrections. The cross section and inelastic mean free path can be obtained from data tables [TAN94], [YEH85]. Because the electron transmission function is a property of the analyser it has to be measured separately. Equation 7 then gives the atomic ratio of two species A and B. In summary the atomic ratio will have an error of about 5 %.

$$\frac{N_A}{N_B} = \frac{I_A / ASF_A}{I_B / ASF_B} \tag{7}$$

2.2 X-ray absorption spectroscopy (XAS)

X-ray absorption probes the absorption cross-section σ_X of the material as a function of the excitation energy of the X-ray beam. The intensity of the transmitted X-ray beam through a sample is given by the Beer-Lambert law (Equation 8).

$$I = I_0 e^{-\int \mu(x)dx} \tag{8}$$

The absorption coefficient μ(x) has a linear dependence on the absorption cross-section σ_X of the material. The absorption cross section can be derived from Fermi's Golden rule (Equation 9).

$$\sigma_x \propto P_{if} = \frac{2\pi}{\hbar}\left|\langle f|\overline{V}|i\rangle\right|^2 \cdot \delta\left(E_f - E_i - \hbar\omega\right) \tag{9}$$

A finite transition probability per unit time P_{if} is given only if $\hbar\omega = E_f - E_i$ is fulfilled. For an excitation from a discrete state into a discrete state this would give a delta function. On the other hand the excitation from a discrete state into the continuum (vacuum for PES) would give a step-function. Its height is proportional to the concentration of the specific atom of the initial discrete state.

As XAS probes the transitions from a core level into unoccupied state absorption appears only if both, core level and unoccupied state, have an overlap in their wave functions. Due to this XAS is very element specific and probes the partial density of states (pDOS). By hybridization and/or charge transfer the absorption into additional states of neighbour atoms is possible due to a now excising overlap in the wave function of both atoms. The next neighbour must not be necessarily of the same atomic species but can be any other element. The wave-function overlap of unoccupied states of neighbouring atoms is of high importance for the subsequent decay processes of the excited atom, which are one of the key aspects of this work.

2.2.1 Dipole selection rules

In Equation 9 $\overline{V}$ is the perturbation between final and initial states $\langle f|$ and $|i\rangle$, respectively. For the interaction of spinless particles with a charge e and mass m with an electromagnetic field (optical excitation) the perturbation $\overline{V}$ is proportional to the dipole operator $e \cdot \overline{r}$.

As a consequence the dipole selection rules have to be taken into account for the transitions, especially when polarized radiation is utilized. I.e.:

1. Angular momentum quantum number: Δl= ±1
2. Magnetic quantum number: Δm= 0, ±1
3. Spin quantum number: Δs= 0
4. Parity of wave-functions has to change: $\pi_f = -\pi_i$

But also spin-orbit coupling has to be taken into account. Light and heavy atoms are treated here separately, both having different selection rules.

Atoms as multi electron systems are described by their primary quantum number n, angular momentum number L, spin quantum number S and total angular momentum J and are thus represented by the term symbol $^{2S+1}L_J$. L is always an upper character of "S, P, D, F, G, H, I, K,...".

For light atoms as the interaction between an electron's angular momentum and orbital momentum is weak it can be treated by a perturbation of the Hamiltonian (LS-coupling). Thus for light atoms as multi electrons system the following rules with J= L+S ($J = |L - S|, ..., L + S$) have to be considered:

1. Orbital angular momentum: ΔL= 0, ±1 (transition from L= 0 to L= 0 is not allowed)
2. Spin: ΔS= 0
3. Total angular momentum: ΔJ= 0, ±1 (transition from J= 0 to J= 0 is not allowed)

In case of intermediate coupling:

- If ΔS= 0 then ΔL= 0, ±1, ±2

For heavy atoms the coupling term cannot be considered as a perturbation anymore. Here jj-coupling is a better way to quantify the electron energy states. Instead of coupling of the total L and S the individual single l couple to their corresponding s ($J = \sum_i j_i = \sum_i l_i + s_i$):

1. Total angular momentum: ΔJ= 0, ±1 (transition from J= 0 to J= 0 is not allowed)
2. Angular momentum quantum number: Δj= 0, ±1

2.3 Resonant photoemission (resPES)

Resonant photoemission can be considered as photoelectron energy resolved XAS. The integral XAS spectrum will be split into its individual PES spectra contributions for each excitation energy value.

ResPES is based on the fact that at the particular core level absorption edge the absorption cross section for the particular element increases drastically. It is of several orders of magnitude higher than for the other elements present in the material. Due to the increased absorption cross section and the decay processes of resonantly created core holes the particular density of states of the element probed are amplified. Hence, resPES valence bands give evidence about the partial density of valence band states (occupied states). For a complete set of resPES VB spectra, where the excitation energy over the core level absorption edge is scanned, also the partial density of states of the CB is probed.

2.3.1 Kramers-Heisenberg

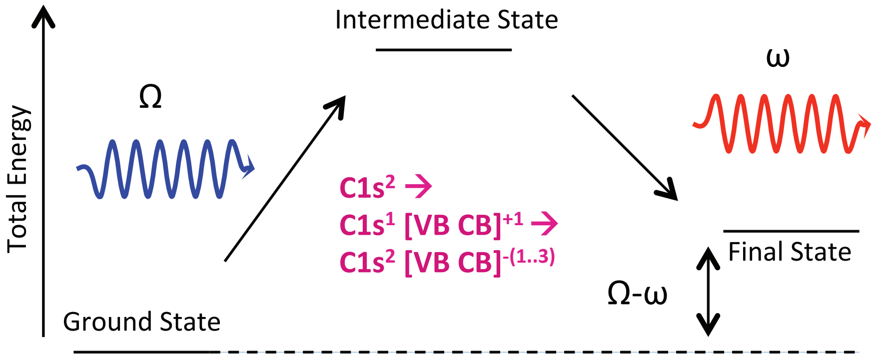

Figure 2.1: *Schematic picture of the Kramers-Heisenberg mechanism. The Figure was reproduced from [GLA09].*

The resonant excitation and decay mechanisms can be described by the Kramers-Heisenberg mechanism (Figure 2.1 and Equation 10) [GLA09]. An electron from the ground state $|g\rangle$ is excited into an intermediate state $\langle n|$ modulated in intensity by the transition operator T_1. The lifetime of the intermediate state Γ_n determines the full width of these resonances. The intermediate state $|n\rangle$ will then decay under the emission of electrons into a final state $\langle f|$.

A second transition operator T_2 describes this decay process. In particular T_2 describes the Auger decay processes.

$$F(\Omega,\omega)=\sum_f \left| \sum_n \frac{\langle f|T_2|n\rangle\langle n|T_1|g\rangle}{E_g-E_n+\Omega-i\frac{\Gamma_{\mathrm{INT}}}{2}} \right|^2 \cdot \frac{\frac{\Gamma_{\mathrm{FIN}}}{2\pi}}{\left(E_g-E_f+\Omega-\omega\right)^2+\frac{\Gamma_{\mathrm{FIN}}^2}{4}} \tag{10}$$

The Kramers-Heisenberg formulation of resonant photoemission already indicates that the absorption and de-excitation process occurs on the same atom.

2.3.2 Decay of the excited state

The understanding of core and valence hole decay processes plays an important role for the interpretation of PES spectra, especially under resonant excitation. In particular lifetime, screening, hybridization, and bonding arrangements influence the decay of core and valence holes.

Two competing processes do take part in the complex process of the core hole decay. First of all the core hole is refilled by an electron from a higher (sub)shell. Inverse to PES the energy difference can be emitted as a photon. As this is an optical process the dipole selection rules have to be fulfilled.

The emission of an electron after the core hole decay is more complex e.g., via spectator or participator Auger decay. The Coulomb operator describes these Auger decays rather than the dipole operator and therefore the Auger decay do not have to obey the dipole selection rules.

The fraction of the kind of decays via emission of photons or electrons depends on the atomic number Z [KRA79a].

For light elements (Z< 15) the Auger decay is the dominant decay mechanism for K-level transitions (> 90 %), but the fluorescence yield gradually increases with Z and is dominant for Z> 60 (equal at Z= 30).

In the following only the Auger decay processes will be discussed as the radiative decay processes are not of relevance for this thesis with focus on PES.

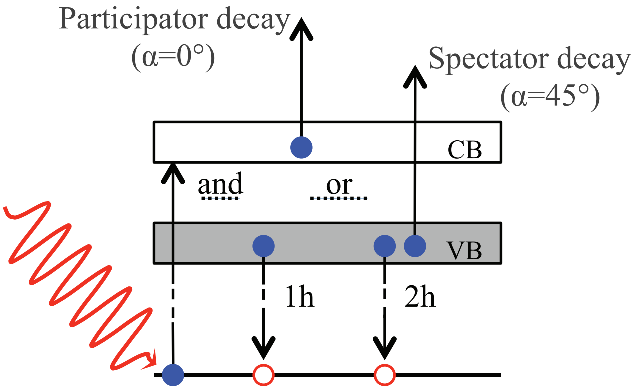

Figure 2.2: *Schematic picture of the Participator Auger decay with a 1h final state and the Spectator Auger decay with a 2h final state. The slope in a* $E_{Bind}(\hbar\omega)$ *diagram defines the angle α.*

2.3.2.1 Participator Auger decay

After the excitation of a core level into an unoccupied state above the Fermi energy (in this example at the C1s resonance) the atom is in an excited intermediate state (denoted by the asterisk in Equation 11). The minimum energy required to excite from a core level into unoccupied states is determined by its binding energy.

$$\left[1s^2 2s^2 2p^n\right] + \hbar\omega \rightarrow \left[1s^1 2s^2 2p^{((n)+1)^*}\right] \tag{11}$$

In case of the participator Auger decay the initial excited core electron will "take part" in the decay process of the core hole (Equation 12). In consequence we have only one valence hole in the final state (Figure 2.2).

$$\left[1s^1 2s^2 2p^{(n+1)^*}\right] \rightarrow \left[1s^2 2s^2 2p^{(n-1)}\right] + e^- \tag{12}$$

The final state of a participator Auger decay is identical to the one of direct photoemission of the particular valence electron (Equation 13).

$$\left[1s^2 2s^2 2p^n\right] + \hbar\omega \rightarrow \left[1s^2 2s^2 2p^{(n-1)}\right] + e^- \tag{13}$$

Hence, the kinetic energy of the emitted Auger electron depends on the excitation energy. The participator Auger decay lines appear as well as core level and valence state photoemission lines at constant binding energy (α= 0°, Figure 2.2).

2.3.2.2 Spectator Auger decay

$$\left[1s^1 2s^2 2p^{(n+1)^*}\right] \rightarrow \left[1s^2 2s^2 2p^{((n-2)+1)^*}\right] + e^- \qquad (14)$$

In case of the spectator Auger decay the atom will stay in an excited state. The core hole will be refilled by one valence electron under emission of a second valence electron. As a result we have to deal with two valence holes in the final state. The kinetic energy of the emitted Auger electron is only determined by the energy difference of the initial core level and the energy level of the refilling electron. It is therefore independent on the provided excitation energy. Thus a spectator Auger decay appears under constant kinetic energy ($\alpha = 45°$, Figure 2.2).

Spectator Auger transitions ($\tau \approx 1$ fs) are slower than Participator Auger transitions ($\tau \approx 500$ as) as one more electron is involved in the decay process (see Table 2.1).

As already discovered in 1935 by D. Coster and R. Kronig there exist two other faster Auger decay processes, which can reduce the intensity of the normal Auger decay process [COS35]. A low normal Auger decay intensity does not necessarily mean that the decay of the core hole took place by a fluorescence process. Here, if possible, the Coster-Kronig decay can be responsible. The following two Coster-Kronig decays are not possible for K shell holes but for higher subshells.

2.3.2.3 Coster-Kronig decay

If the initial hole and one of the two initial electrons involved in the decay process have the same principal quantum numbers (e.g. $L_2L_3M_{45}$) the Auger transition is called a Coster-Kronig transition [MCG72].

2.3.2.4 Super Coster-Kronig

On the other hand if the initial hole and both initial electrons involved have the same principal quantum numbers (e.g. $M_{23}M_{45}M_{45}$) the Auger transition is called a Super Coster-Kronig transition [MCG72]. In contrast to the Coster-Kronig transition Super Coster-Kronig transitions are only possible for M shell electrons and upward.

A short summary about the lifetimes of these Auger decay processes is given in Table 2.1.

Table 2.1: *Overview of the typical lifetime of the different core hole decay processes.*

Process	**Holes in final sate**	**Lifetime τ**	**Reference**
Excitation	-	< 1 as	-
Participator	1h	500 as	-
Spectator	2h	1 fs	[KRA79b]
Coster-Kronig	2h	< Spectator	-
Super Coster-Kronig	2h	1/10 Coster Kronig	-
Core hole	-	< 6 fs	[FOE06]

2.3.2.5 Auger decay – selection rules

A KVV Auger transition c → jk where the primary core hole c decays via two valence states j and k under emission of an Auger electron e is described by the coulomb and exchange matrix elements J_{jk} and $K_{jk} = J_{kj}$, respectively. J_{jk} (K_{jk}) depends on the four orbitals of e, c, j, and k and is given by Equation 15 [SIE75], [UMB84].

$$J_{jk} = \left\langle \varphi_j \varphi_k \middle| \frac{e^2}{r} \middle| \varphi_c \varphi_e \right\rangle \tag{15}$$

Approximating the continuum by a spherical wave centred at the atom and neglecting matrix elements with contributions of neighbouring atoms can simplify these matrix elements. This assumption is only valid if most of the charge density is located on the same atom as the primary core hole for instance oxygen in water.

The orbital wave function can just be described in this simple approximation by the quantum numbers l and m. It is now possible to calculate the intensity of the Auger decay transition by the sum over all channels of l and m. For the involved valence states j and k it is then given by Equations 16, 17, and 18 [SIE75].

$$I_{jk}(\text{singlet}) \propto \sum_{lm} \left| J_{lm,jk} + K_{lm,jk} \right|^2, \quad \text{j} \neq k \tag{16}$$

$$I_{jk}(\text{triplet}) \propto 3\sum_{lm} \left| J_{lm,jk} - K_{lm,jk} \right|^2, \quad \text{j} \neq k \tag{17}$$

$$I_{jk} \propto 2\sum_{lm} \left| J_{lm,jk} \right|^2, \quad \text{j}=k \tag{18}$$

In the one-electron picture the kinetic energy of the Auger decay line with the Intensity I_{jk} can be approximated by Equation 19 [UMB84].

$$E_{\mathrm{kin}} = E_{\mathrm{bind,\,c}} - E_{\mathrm{bind,\,j}} - E_{\mathrm{bind,\,k}} - U_{eff}(j,k;s) \tag{19}$$

The kinetic energy depends on the binding energy of the core hole ($E_{\mathrm{bind,\,c}}$), the valence electron j ($E_{\mathrm{bind,\,j}}$), the valence electron k ($E_{\mathrm{bind,\,k}}$), and U_{eff}, which includes spin-dependent interaction, coulomb repulsion, and static relaxation.

As the coulomb operator is a scalar operator the angular momentum quantum numbers are preserved in the Auger decay. For the final state consisting of the atom and the emitted Auger electron with Π_b and Π_a as their combined parity of the initial and final ionic state the selection rules of the coulomb matrix element are given in Equation 20 [CLE01].

$$\Delta S = \Delta L = \Delta J = \Delta M_S = \Delta M_L = 0, \quad \Pi_a = \Pi_b \tag{20}$$

2.3.3 ResPES diagram

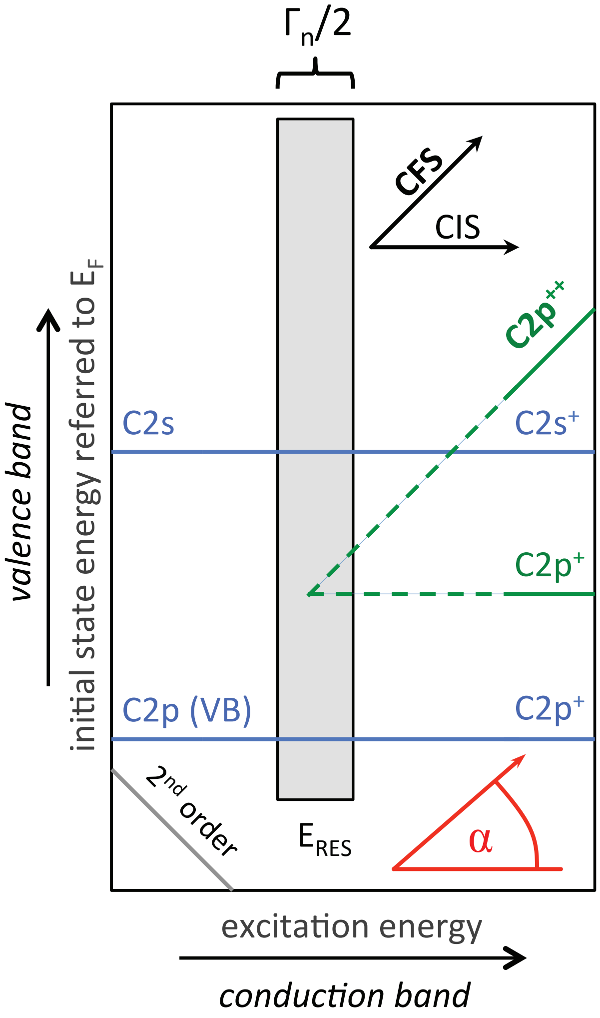

Figure 2.3: *Schematic picture of the 2D resPES diagram. The initial state energy (valence band) is the ordinate and the abscissa reflects the excitation energy (conduction band). The 2nd order core level excitation is indicated in the lower left corner by the grey line. Valence band state photoemissions are shown in blue, the spectator Auger (α= 45°) and participator Auger decay (α= 0°) are indicated by green lines. The angle α is defined by the slope in this* $E_{Bind}(\hbar\omega)$ *diagram (red). Constant initial state (CIS; α= 0°) and constant final state (CFS; α= 45°) spectra are indicated by black arrows.*

The resPES diagram, which consists of typically 100 valence band spectra, reflects the full resPES dataset used in this thesis (Figure 2.3).

The initial valence state energy is the ordinate and the abscissa reflects the excitation energy. The electron yield intensity is usually given in a colour coded logarithmic contour plot, where the brightness corresponds directly to the intensity. In this resPES diagram the Auger, constant initial state (CIS), constant final state (CFS), and XAS data are displayed simultaneously. In terms of such a $E_{Bind}(\hbar\omega)$ diagram valence band features appear at constant binding energy (α= 0°, blue line in Figure 2.3). The two-hole final state Auger decay (spectator decay) is propagating under constant kinetic energy (α= 45°, green $C2p^{++}$ line in Figure 2.3). A participator Auger decay (one-hole final state) appears at constant binding energy and leads to resonances in the valence band states (α= 0°, green $C2p^{+}$ line in Figure 2.3). The second order core electron excitation is found in the lower left corner and can be used to identify the Fermi energy position for XAS.

2.3.4 Determination of Fermi energy in resPES diagram

A special case for resPES is the parallel excitation of the core level by 1st and 2nd order light at synchrotron beamlines with a PGM monochromator. At resonant excitation the 2nd order line can be used to deduce the position of E_F in XAS spectra (Figure 2.3).

The energy of the first and second diffraction order of the monochromator, meeting both the requirements of the exit slit and optics to reach the sample, have the following relation taking into account core level excitation and "Fermi” excitation:

$$E_{\text{Kin. Core}} = 2\cdot\hbar\omega_{\text{1st order}} + E_{\text{Bind. core}} = \hbar\omega_{\text{2nd order}} + E_{\text{Bind. core}} \cong E_{\text{Kin. Fermi}} \qquad (21)$$

As both, the XAS and 2nd order line spectrum are recorded in the same spectra and influenced by the same potential they also see the same Exciton shift. If the second order core level – at core level resonance – and a first order core level – far away from resonance – show the same core level binding energy no Exciton shift is present and the approximation in the XAS spectra is valid.

Hence, the excitation energy of the zero initial state crossing of the 2nd order line determines the Fermi energy in a resPES diagram. For instance, this is the case when the core Exciton is replaced by a localized Exciton, i.e. the excited electron is bound to a valence hole localized by polarization of charges rather than to the initial core hole.

2.3.5 FANO resonance

A FANO resonance is the interference of two excitation channels. The interference is possible when for both emission channels the final state electron configuration is the same [FAN66].

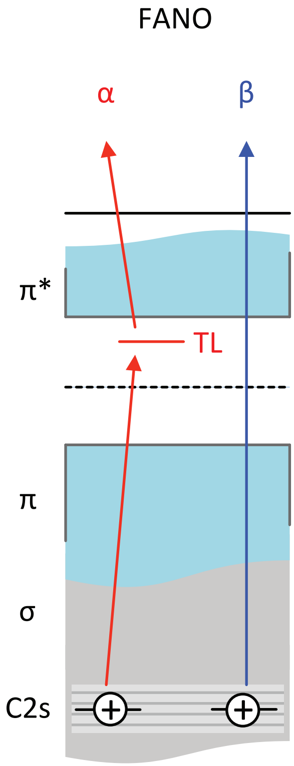

Figure 2.4: *FANO resonance mechanism. The channel α corresponds to a photoemission of a C2s valence band state involving an intermediate trapping level TL and channel β to a direct photoemission of a C2s valence band state.*

Under resonant excitation for instance at the carbon 1s resonance the emission of carbon 2s valence band states is resonantly enhanced as both states are coupled together: $\left|\gamma\right|1s+2s\rangle$.

For a trap state TL near a continuum of states the photo emitted electron from a C2s VB state can be excited into in this trapping level as an intermediate state before it is further emitted into the continuum. This is considered as channel α of the FANO resonance (Figure 2.4). Channel β is simply the direct photoemission without involving the trapping level.

In both processes the initial state of the C1s atom and the final state with a VB hole in the C2s level are the same. Both emitted electrons by channel α and β have the same kinetic energy and can interfere. The result is a FANO profile at the C2s VB level.

The intensity of the emission can be described by the FANO line shape (Equation 22) [FAN66].

$$I(\hbar\omega) \simeq \frac{(\varepsilon + q)^2}{\varepsilon^2 + 1} \tag{22}$$

The FANO parameter q describes the ratio of the transition probabilities into channel α or β $\left(q^2 = \frac{|\alpha|^2}{\delta \cdot |\beta|^2} \right)$ with δ as the number of unperturbed continuum states for direct photoemission β. The reduced energy ε depends on the excitation energy ħω, the binding energy (TL_{BE}) and the Full Width at Half Maximum (FWHM) of the particular trapping state (TL_{FWHM}):

$$\varepsilon = \frac{\hbar\omega - TL_{BE}}{TL_{FWHM}/2} \tag{23}$$

2.4 Experimental setup

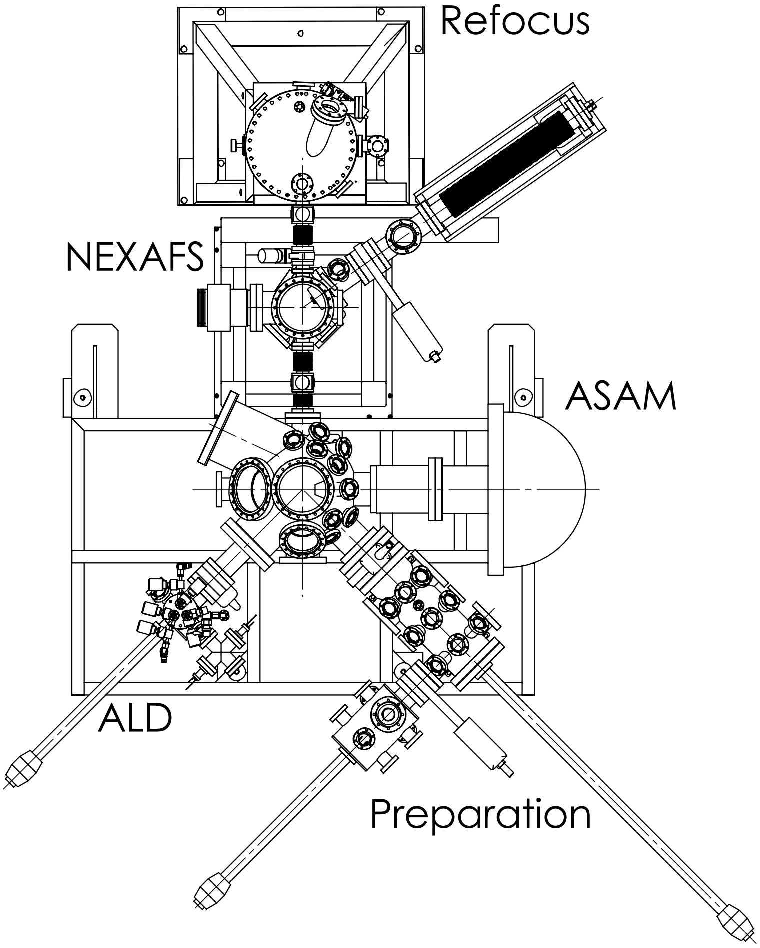

Figure 2.5: *Experimental Setup of the ASAM Endstation at the beamline U49/2-PGM2 at BESSY II, Helmholtz-Zentrum Berlin.*[†]

The U49/2-PGM2 beamline at BESSY II is based on a planar hybrid Undulator with a period length of 49.4 mm and 84 periods. It is equipped with a Jenoptik collimated plane grating monochromator with switchable gratings of 1000 l/mm and 300 l/mm [FOL01]. The resolving power of the monochromator is $E/\Delta E = 10.000$ and it is aligned via N_2 gas phase $1s \rightarrow \pi^*$ core hole absorption. An automatic switching ability between 1st, 3rd, and 5th harmonic covers an excitation energy range of 85 eV to 1890 eV. The accuracy of the excitation energy setting is better than 0.1 eV.

[†] CAD draw of Experimental Setup by Guido Beuckert.

In addition the resolution of the photon beam depends on the setting of the exit slit.
For the experiments an exit slit of 10 µm for photoemission measurements and an exit slit of 20 µm for XAS and resPES diagram measurements both in multi-bunch hybrid mode of the synchrotron (≈ 300 mA ring current at 1.7 GeV) was used. The most common exit slit settings with possible energy resolution are given in Table 2.2.

Table 2.2: *Overview of the most common energy settings. The values in meV represent the experimental broadening of the beamline without additional broadening by the experimental station.*

		Exit slit	
Excitation energy	**10 µm**	**20 µm**	**30 µm**
150 eV	2.6	5.2	7.8
285 eV	6.8	13.6	24
300 eV	7.4	14.7	22.1
530 eV	17.3	34.6	51.9
640 eV	22.9	45.9	68.8
780 eV	30.9	61.7	92.6
900 eV	38.3	76.5	114.8
1000 eV	44.8	89.6	134.4
1200 eV	58.9	117.8	176.7

The Near Edge X-ray Absorption Fine Structure (NEXAFS) chamber (Figure 2.5) consists of a Multi Channel Plate (MCP) detector for the fluorescence yield (TFY) at an angle of 55° with respect to the incident photon beam. A Keithley picoammeter[‡] is used for measuring the sample current {total electron yield (TEY)}. Another Keithley picoammeter is used for measuring the photon flux (I_0) obtained from the refocusing mirror as the mirror-current or a gold-mesh that was put into the beam.

[‡] Keithley Model 487 Picoammeter/Voltage Source.

An ARM interface controller (SPECS Armin 10) collects the digital count signal of the MCP and the analogue signals from the picoammeters and is connected to the measurement computer.

In case of the ASAM system (Figure 2.5) the MCP detector is replaced by a SPECS Phoibos 150 hemispherical electron analyser with a 2D-CCD (10 virtual channels) or by a Surface-Concepts 1D-DLD[§] electron detector (100 virtual channels). TEY and I_0 measurements are carried out in the same way as for the NEXAFS system.

The SpecsLab2 measurement software allows the parallel measurement of TFY or PES, TEY and I_0. It also controls the selection of the desired excitation energy via a connection to the beamline computer. Automatic selection of the excitation energy is a necessary requirement for X-ray absorption measurements.

This enables the use of PES, resPES, CIS, and CFS measurement modes. An external program can create templates for resPES diagram measurements routinely for SpecsLab2.

[§] Delay Line Detector.

2.5 Data normalization

Due to the contamination of X-ray optics in the synchrotron beamline by nitrogen, oxygen, and especially carbon the recorded X-ray absorption spectra do not show the real spectra of the pure substance under investigation. The contamination can produce artefacts and can even dominate the as-recorded spectra. Therefore it is necessary to correct the spectra regarding these contaminations.

A correction spectra which contains the flux intensity of the storage ring and the contaminations from the beamline optics was obtained from either the photocurrent of a GaAs diode that was put into the beam (before the installation of the Refocusing-Mirror at the U49/2-PGM2), by using the mirror current of the installed refocusing-mirror (after its installation at the U49/2-PGM2), a gold-mesh (90 % transmittance), or by using the sample current of a sputter cleaned gold reference sample. Each of these reference signals is equivalent and is referred in the following only as I_0. Detailed information on the XAS normalization process can also be found in [WAT06].

2.5.1 XAS normalization

For standard XAS measurements the recorded raw spectra have to be divided by an offset, slope, and energy shift corrected I_0 spectrum. The offset and slope compensate for the different detector sensitivity and gain of the used detectors. An energy shift in the wavelength space (the monochromator energy drift is linear in the wavelength space) is necessary to compensate time dependent drifts of the energy if I_0 and raw spectrum are not measured in parallel. This process has been automated in OriginPro as shown in Figure 2.6. After the I_0 correction each spectrum was normalized before the absorption edge to zero and to one at the high excitation energy side of the recorded spectra (0-1 edge-jump normalization).

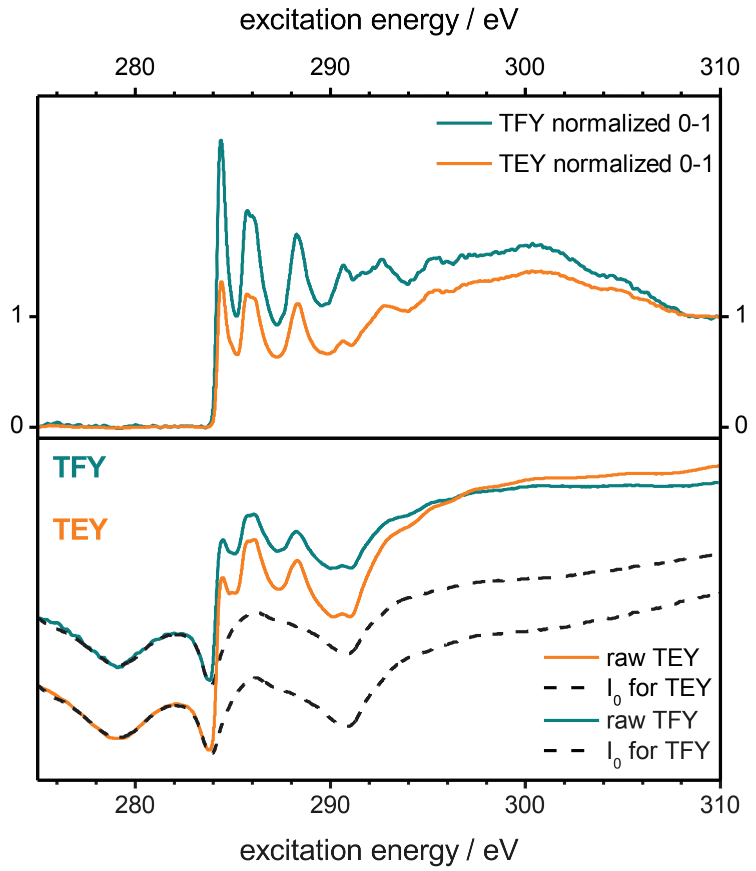

Figure 2.6: *Example of the XAS normalization process of PCBM at the C1s edge. The TFY and TEY spectra are shown in green and orange, respectively. The bottom panel depicts the raw data spectrum (solid line) and the offset, gain, and energy shift corrected* I_0 *spectrum (dashed line). In the top panel the* I_0 *corrected and 0-1 edge jump normalized raw data are shown.*

2.5.2 ResPES diagram normalization

Resonant photoemission diagrams have to be corrected in the same way as the XAS spectra. This is done by dividing the raw data matrix by an appropriate I_0 spectrum. The appropriate I_0 spectrum is obtained by normalizing the integrated resPES diagram. In addition, especially at the C1s edge, the 2nd order excitation line of the core level has to be taken into account. As the 2nd order excitation line is excited by second order light the flux is different and in principle the I_0 of the double excitation energy has to be used only to correct this single line. For the sake of convenience, and also because the 2nd order light shows monotone behaviour or is of low intensity at the absorption edges under investigation in this work the additional correction by a 2nd order I_0 spectrum is neglected.

Only at the C1s edge a correction for the 2nd order excitation line was performed.

In Figure 2.7 this three step process is displayed: (a) the uncorrected raw resPES diagram, (b) the I_0 corrected resPES diagram, and (c) the I_0 and 2nd order corrected resPES diagram. This process is applied to all measured C1s edge resPES diagrams in this work.

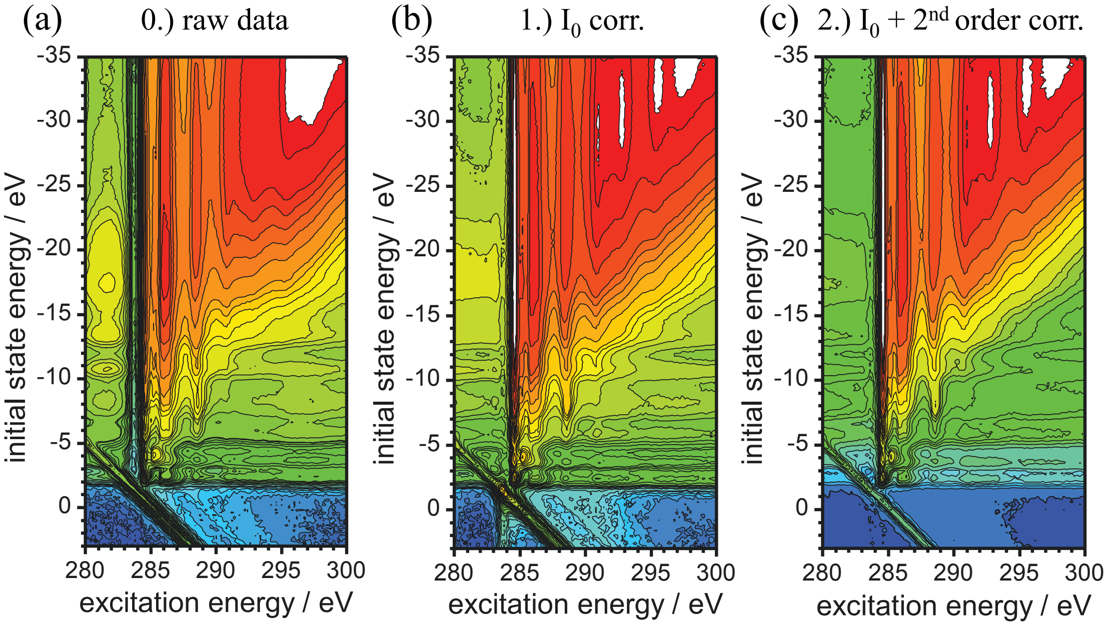

Figure 2.7: *Example of resPES diagram normalization in two steps at the C1s edge of PCBM: (a) the raw uncorrected resPES diagram, (b) the raw* I_0 *corrected resPES diagram, and (c) the raw* I_0 *and 2nd order corrected resPES diagram.*

2.5.3 PES normalization

Photoemission spectra are simply divided by the parallel measured current from the flux monitor (refocusing-mirror or gold mesh in the gas-cell).

2.6 Sample preparation

2.6.1 Organic material

PCBM (purity 99.5 %), rr-P3HT (purity 99.995 %, M_n= 54000-75000), rra-P3HT {1:1 (head-to-head):(head-to-tail) linkages of regioisomers}, and Indium tin oxide (ITO) coated glass slides with a surface resistivity of 30-60 Ω/□ were purchased from Sigma-Aldrich.

P3HT and PCBM layers were prepared using the spin-coating technique. ITO glass slides of 1x1cm^2 were used as the substrate.

P3HT was dissolved in chloroform giving film thickness of about 100 nm for 1 wt% and 170 nm for 2 wt% (15 sec at 1500 rpm).

Chloroform was used as solvent for PCBM (2 wt%). The chosen spin coating speed (15 sec at 1500 rpm) led to film thicknesses of about 50 nm after drying.

All samples were annealed at 140 °C for 30 min to improve the crystallinity. The preparation and the transport of the samples were done under inert argon atmosphere.

2.6.2 HOPG

The HOPG sample (supplied by Veeco) was cleaved several times using Scotch tape right before the introduction into the vacuum system and the measurement [GEI11]. In this way a fresh surface without contamination was obtained (under the detection limit of synchrotron radiation photoelectron spectroscopy).

2.6.3 Graphene

Graphene flakes grade AO-2 and AO-4 were obtained from Graphene-supermarket[**]. The powder was annealed at 1000 °C under nitrogen atmosphere for 30 min. In this way high quality Graphene flakes were obtained.

[**] http://graphene-supermarket.com/

A high quality Graphene reference sample on Ni(111) was prepared by a CVD process (prepared and delivered by MPI Stuttgart). The Ni(111) substrate layer was grown epitaxial on an MgO(111) substrate [IWA11].

Graphene layers on Cu were prepared by a CVD process and while those on SiO_2 are transferred from the Graphene-on-Cu process. Both, monolayer Graphene on Cu and SiO_2 were obtained from Graphenea[††].

2.6.4 OER Catalyst

The Co-PI catalysts were prepared as described in literature [ESS11]. Anodized Nickel was used as a substrate (2 mA cm^{-1} in 1M KOH for 5 min), a Pt foil as the counter electrode, and a Ag/AgCl reference electrode. The deposition of the cobalt catalyst was performed in an electrolyte containing 0.5mM $Co(NO_3)_2 \cdot 6H_2O$, 0.1M potassium phosphate (K_2HPO_4, and KH_2PO_4) (pH= 7.0). Cyclic voltammetry sweeps were performed with a VersaSTAT 4 potentiostat in a potential range of -1.5 V to 1.5 V with a sweep rate of 0.5 V/s until a steady state was reached.

The catalyst films were deposited at a constant potential of 1.1 V. By increasing the deposition time at the given potential the deposited amount of Co ions is increased. The as deposited charge is normalized to the surface area of the sample (0.38 cm^2) and can be used as a measure of the film thickness of each sample (0.3 C/cm^2 up to 4.5 C/cm^2). For increased deposition time of the Co-PI layer – the charge density (C/cm^2) – the Co-PI layer thickness is increased and a bulk-like Co-PI catalyst is grown.

After preparation the samples were rinsed with ultra-pure water (18 MΩ) before the introduction into the UHV system.

[††] http://www.graphenea.com/

Chapter 3 Results

In this chapter the results on the three different systems organic semiconductors, Graphene, and OER catalyst Co-PI will be described in detail.

Beginning with charge carriers (Polarons and Excitons) in P3HT and PCBM the first combination of a new multiple Auger decay {spectator-participator (S+P)} is observed.

This is followed by Excitons in HOPG and Graphene. Another two new combinations of Auger decay processes {double spectator (S+S) Auger and double spectator (S+S)* Auger-Gain decay} are observed here which are characteristic for free-standing Graphene.

Last, the results on Co-PI will be presented. Core level PES is used to deduce the structural motif and oxidation state. Parallel study of the Co2p and O1s resPES give evidence about the spin and oxidation state of the particular cobalt and oxygen states. By the use of the multiple Auger combinations the existence of localized in-gap states (localized charge transfer states – a special class of Polaron and exciton states in TM-oxides) is evident.

3.1 P3HT

3.1.1 XRD and UV-Vis

The as prepared regioregular-Poly(3-hexylthiophene-2,5-diyl) films were characterized by optical (UV-Vis) and surface characterizing methods {AFM, X-ray diffraction (XRD)}. The results are briefly summarized here. Atomic force microscopy showed no pinholes and is also used to give an estimation of the film thickness with a roughness of RMS= 10 nm.

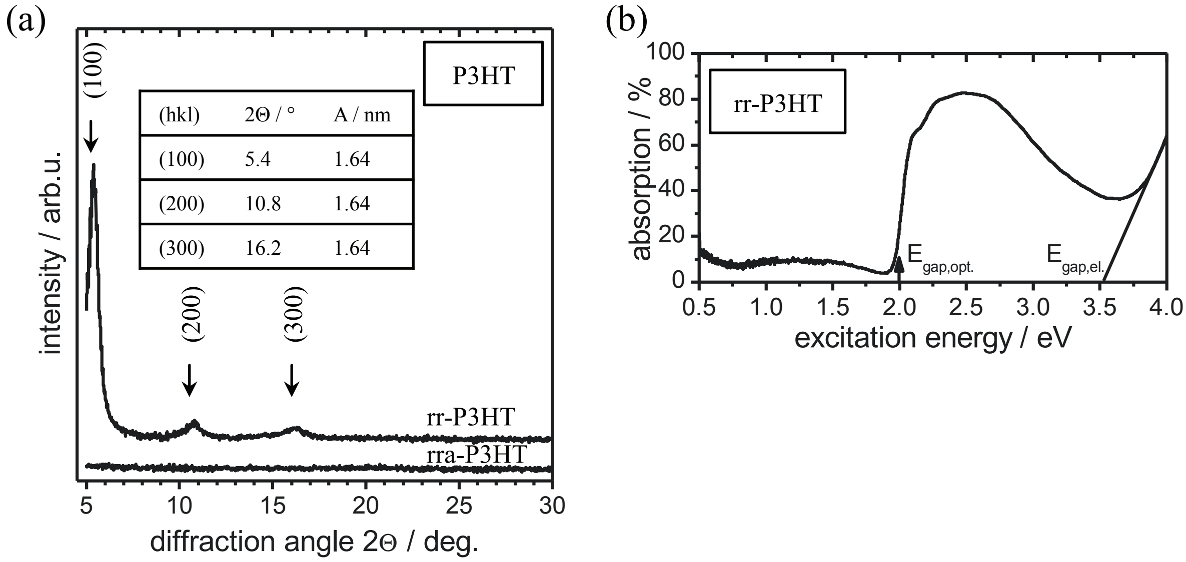

Figure 3.1: *X-ray Diffraction (Cu Kα) measurements*[‡‡] *of annealed rr-P3HT and annealed rra-P3HT (a). ITO background was subtracted from a separate measured sample. UV-Vis absorption spectra of rr-P3HT*[§§] *(b). The electronic ($E_{gap,el.}$) and optical ($E_{gap,opt.}$) band gaps are indicated.*

In X-ray Diffraction (Cu Kα) measurements rr-P3HT showed reflexes at 2Θ= 5.4°, 10.8°, and 16.2° resulting in an inter-chain distance of A= 1.64 nm (Figure 3.1a). In contrast rra-P3HT did not show any features. The correlation length LC of 10 nm was determined using Scherrer's equation and the FWHM of the (100) peak [YAN96]. It can be identified as the crystallite size and its value is in agreement with the literature [JOS09].

From the UV-Vis absorption data of the samples an optical band gap of 2.0±0.1 eV could be extracted (Figure 3.1b). The π-π* absorption, starting at 2 eV, also shows vibronic fine structure. This indicates as well that π-π stacking occurred in rr-P3HT [FAN11], [YAM98].

The optical transitions of 2D- and 1D-Polarons are represented through the weak peak below 0.5 eV and the weak broad absorption centred on 1.3 eV. The particular transition energies for 2D-Polarons are determined in more sensitive data (TFY and TEY-XAS). They are

---

[‡‡] XRD measurements by Mathias Kappa (BTU Cottbus).

[§§] UV-Vis measurements of rr-P3HT were performed by Shine Philip (BTU Cottbus) at HZB, Berlin-Wannsee.

calculated by the energetic position of Polaron features in the high resolution XAS data. The Polarons are originating from the charge transfer at the interface as discussed later.

3.1.2 Core level

The core level spectra of rr-P3HT give evidence about correct composition of the layer and possible oxidation of the layer. For referencing the C1s X-ray absorption spectra and resPES profile to the Fermi level the binding energy of the C1s core level has to be known.

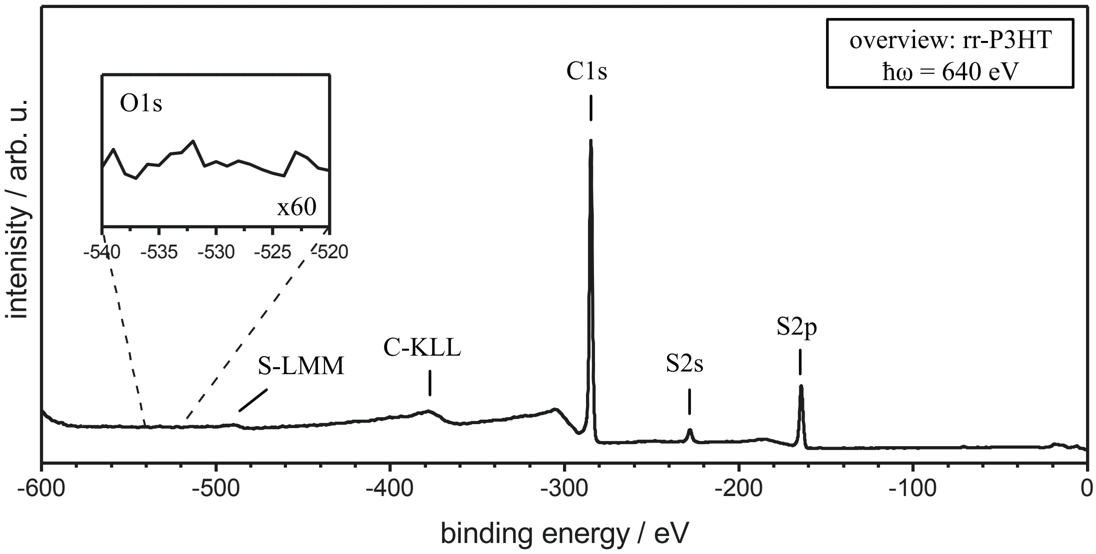

Figure 3.2: *Overview spectrum of rr-P3HT at an excitation energy of 640 eV. The inset shows the range where the O1s core level would be expected. The oxygen content is under the detection limit of synchrotron radiation photoemission (SR-PES).*

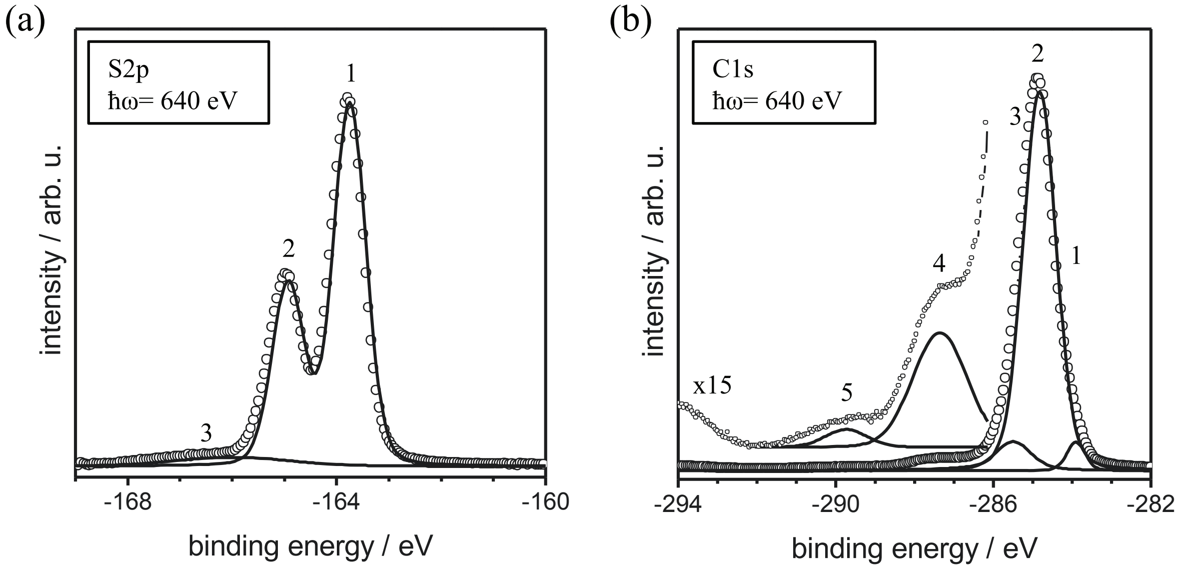

Figure 3.3: *S2p (a) and C1s (b) core level spectra of rr-P3HT taken at an excitation energy of 640 eV. The circles represent the measurement data whereas the solid lines show the peak decomposition. Carbon 1s peaks 4 and 5 are shown magnified (x15) in addition.*

An overview spectrum of rr-P3HT is shown in Figure 3.2. No traces of oxygen are detectable (inset of Figure 3.2).

In Figure 3.3 the S2p and C1s core level spectra of a pristine rr-P3HT film are shown. A peak decomposition of the corresponding core level spectra was performed and is included in Figure 3.3. Voigt-profiles were used in this process. The peak position and FWHM values of all contributions of the C1s and S2p core level that are obtained from the peak decomposition are listed in Table 3.1.

In the S2p core level spectrum the $S2p_{3/2}$ component is found at -163.75 eV. A small satellite feature is observed at the higher binding energy side at -166 eV, which can be attributed to oxidized sulphur species [FAN11].

The main C1s core level line is found at a binding energy of -284.83 eV. Satellites are visible on the higher binding energy side at about -287.36 eV and -289.74 eV, which can be attributed to π-π* shakeup transitions [KEA90], [SAL88].

From the X-ray photoemission spectroscopy (XPS) peak intensities the stoichiometry was determined, which is found to be in excellent agreement with the expected composition of rr-P3HT films (C/S= 10±0.5).

Table 3.1: *Peak decomposition data of the C1s and S2p core level shown in Figure 3.3.*

Peak	**Assignment**	**Peak Position / eV**	**Area / % (FWHM / eV)**
S2p (1)	$S2p_{3/2}$	-163.75	65 (0.75)
S2p (2)	$S2p_{1/2}$	-164.93	33 (0.75)
S2p (3)	ox. S	-166.00	2 (2.6)
C1s (1)	-	-283.90	3.6 (0.55)
C1s (2)	C=C	-284.83	85.5 (0.99)
C1s (3)	-	-285.50	7.7 (1.06)
C1s (4)	π-π* shakeup	-287.36	2.8 (1.63)
C1s (5)	π-π* shakeup	-289.74	0.4 (1.24)

3.1.3 C1s resPES

For the identification of Excitons, Polarons, and especially in order to observe the propagation of the resonant Auger decay a full resPES profile at the C1s edge of rr-P3HT is necessary.

For rr-P3HT the resPES diagram is shown Figure 3.4. The photoelectron intensity is color-coded and scaled logarithmic.

The 2h final state Auger (spectator decay) is propagating under 45° (constant kinetic energy) as indicated by the black arrows.

Below 292 eV and above 287 eV an additional Auger transition (white arrow) is observed.

This Auger propagates under 67.5° and is assigned to a 3h final state, for which the model is given in Chapter 4.2.2.1 and is referred from here on as the (S+P) Auger decay.

In the presence of the (S+P) Auger decay the spectator Auger decay (2h) is shifted by 5 eV towards higher kinetic energy from E_{kin}= 258 eV to E_{kin}= 263 eV.

The 67.5° Auger decay does not start with the first absorption resonance at 285 eV (E_T). It is obvious that the 67.5° Auger decay is starting at higher excitation energies at 287 eV (E_S). The feature at 285 eV is therefore of different nature and will be discussed later on.

In the resPES two valence bands – C2p π and C2p π-σ band – are marked. These are used further in the next section for the identification of excitonic states, polaronic states, and the conduction band minimum (CBM).

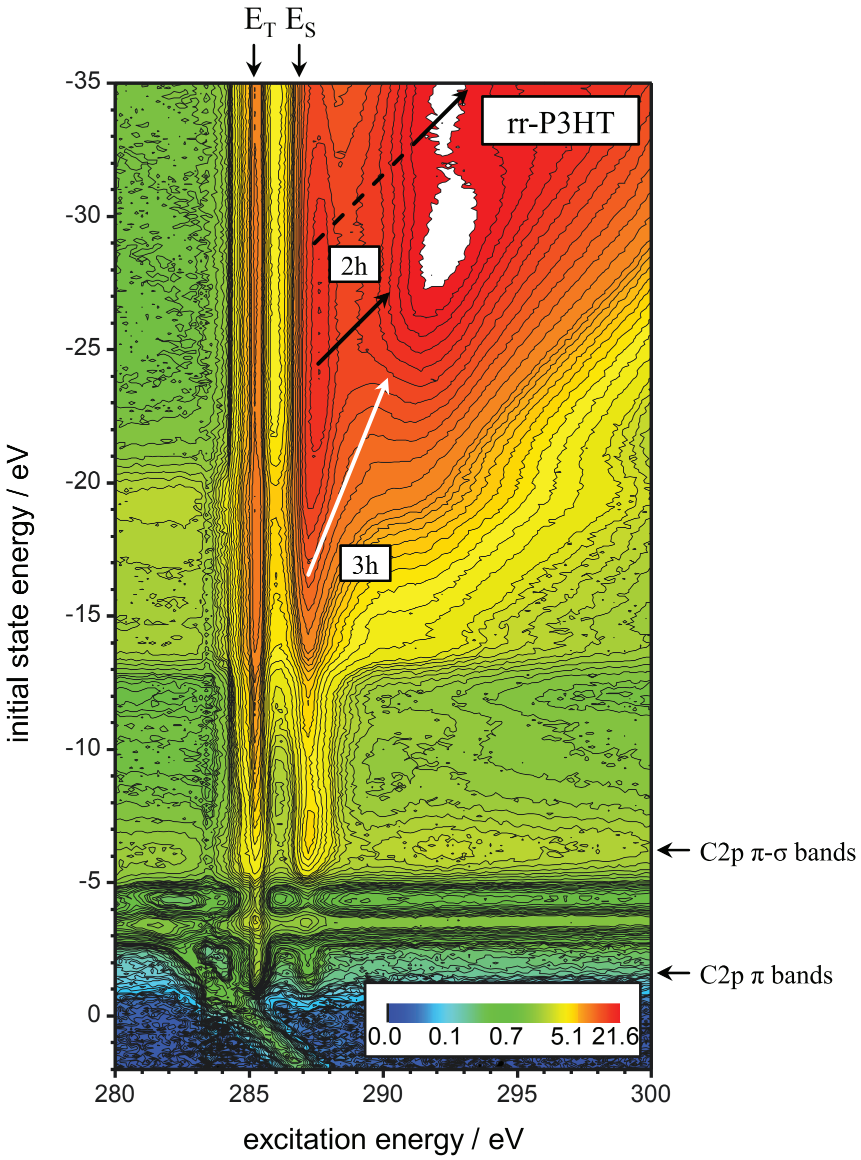

Figure 3.4: *resPES diagram of rr-P3HT on ITO. The intensity of the signal is color-coded in a logarithmic scale. The white and black arrows indicate the 67.5° 3h (S+P) Auger and 45° 2h (S) Auger process, respectively. Indicated by the dashed line is the shift of the 2h (S) Auger between π*- and σ*-band. The position of the singlet (E_S) and triplet (E_T) Exciton is indicated on top. The CIS spectra are taken by horizontal cuts as indicated by the corresponding arrows.*

3.1.4 Conduction and valence band

Valence band and constant initial state spectra (conduction band) taken from the C1s resPES diagram (Figure 3.4) can be further use to evaluate the nature of the prominent features E_T and E_S of rr-P3HT.

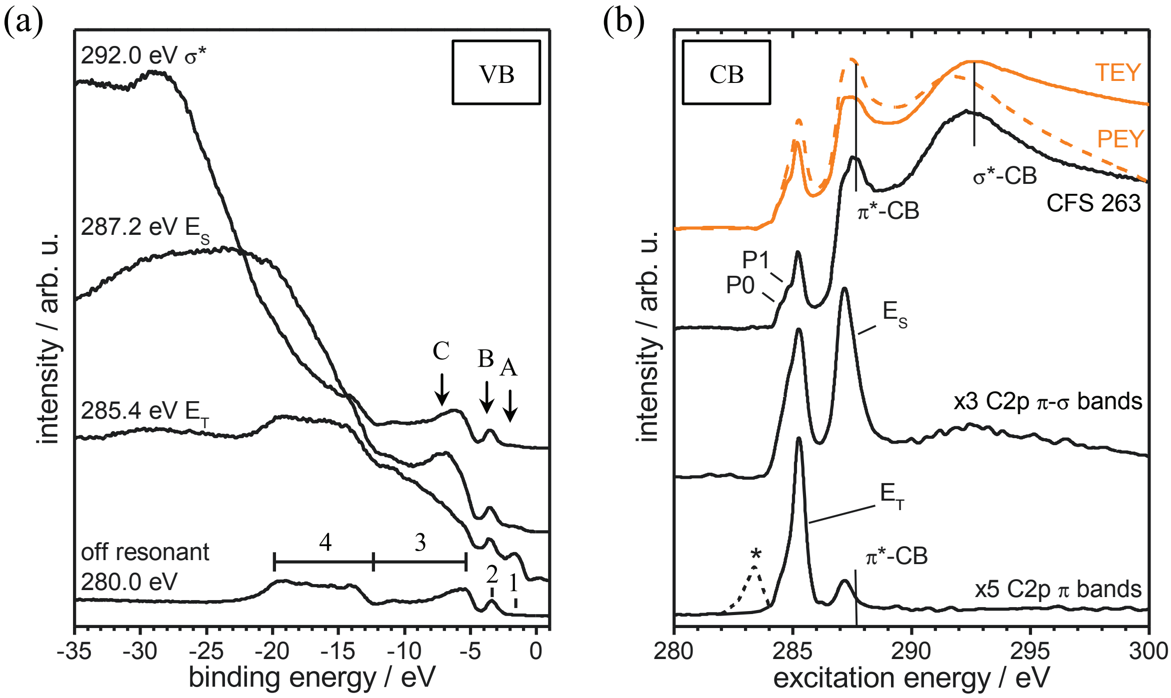

Figure 3.5: *The valence band spectra of rr-P3HT recorded at an excitation energy of 280.0 eV (off-resonance), 285.4 eV (triplet π* Exciton resonance E_T), 287.2 eV (CBM, singlet π* Exciton E_S) and 292.0 eV (σ* Exciton) (a). XAS spectra in constant initial state mode, in constant final state mode and the total electron and partial electron yield (TEY and PEY) of rr-P3HT (b). The excitonic levels are marked with E_T (285.4 eV), E_S (287.2 eV) and σ* (292 eV). P_0 and P_1 are related to polaronic contributions.*

In Figure 3.5a the Valence band spectra of rr-P3HT taken off-resonant at ħω= 280 eV, at the resonance of E_T (285.4 eV), E_S (287.2 eV), and σ* (292.0 eV) are shown.

In the off-resonant spectra the valence band maximum is found at -0.43 eV, the C2p π/HOMO (1) between -0.5 eV and -2.5 eV, the S3p π (2) at -3.4 eV, the S3p-C2p states (3) between -5 eV and -12 eV, and the C2s-S3s bands (4) between -12 eV and -20 eV [DAN93], [FUJ90], [GHI96], [SAL88].

All resonant VB-spectra show three resonances labelled A, B, and C in Figure 3.5a. They correspond to the HOMO (A), S3p π (B), and onset to the C2p/S3p (C) band. Feature A is especially pronounced for E_T (attributed to a triplet Exciton as discussed in Chapter 4.1.1). The increase in intensity is due to participator Auger decays (1h final state). Aside from that the major difference is found in the spectator Auger decay, as expected. From previous observations the contribution to each of the three VB-spectra should be fundamentally different due to the fact that at E_T no spectator decay is observed, at E_S the spectator Auger decay is following an angle of 67.5° and for the σ* spectrum the normal spectator is observed (Figure 3.4).

Indeed, for the VB taken at the threshold of the σ* resonance at 292 eV the normal C-KLL Auger feature is found at a kinetic energy of 263 eV (Equation 5). At the π* threshold of 287.2 eV this feature is broadened due to the observed 67.5° Auger decay, which is neither at constant kinetic energy nor at constant binding energy. In contrast the contribution to the first resonance at 285.4 eV, where no 67.5° or 45° Auger decay is observed, is broad and unstructured. From its profile the decay into the KLL Auger decay channels can be excluded. Therefore there must be different mechanisms or states involved.

In Figure 3.5b several cuts of the rr-P3HT resPES diagram (Figure 3.4) at constant initial state energy (CIS) and constant kinetic energy (CFS) are shown. In addition, XAS spectra in the total electron and partial electron yield (TEY and PEY) are included. For TEY, the total electronic signal during the scan is measured, the PEY represents the integral over the corresponding resPES diagram. In all modes, a sharp resonance with a main peak at an excitation energy of 285.4 eV (E_T) and a second feature as a sharp resonance for an excitation energy of 287.2 eV (E_S) is present for rr-P3HT.

Except for the excitation out of the C2p π band also a third resonance for an excitation energy of 292 eV (σ*) is observed. Smaller contributions on the low excitation energy side of E_T are related to the polaronic states P_0 and P_1.

Focusing on these resonances in rr-P3HT the first resonance E_T is found to remain at constant excitation energy without any further intensity variation going to higher initial state energies. Instead the resonances at 287.2 eV (E_S) and 292 eV (σ*) show a shift in excitation energy and an increase in their intensity for higher binding energies (from π towards σ states). The shift for E_S and σ* is due to an increase in intensity of the π*-CB and σ*-CB peak, the overall intensity increase is due to the Auger decay.

It can be concluded that E_T, E_S, and σ* (292) are localized features. The energy shift of E_S and σ* is due to the appearance of the π*- and σ*-bands. In particular, the apparently shifted E_S feature is attributed to the CBM at 287.6 eV (Figure 3.5b).

The localized features E_S and σ* can be attributed to the singlet π* and σ* Excitons. From the energy shift of these peaks their binding energy can be extracted. A value of 0.4 eV is obtained for the π* Exciton and 1 eV for the σ* Exciton. These values are in agreement with the literature [DEI10], [HOR02].

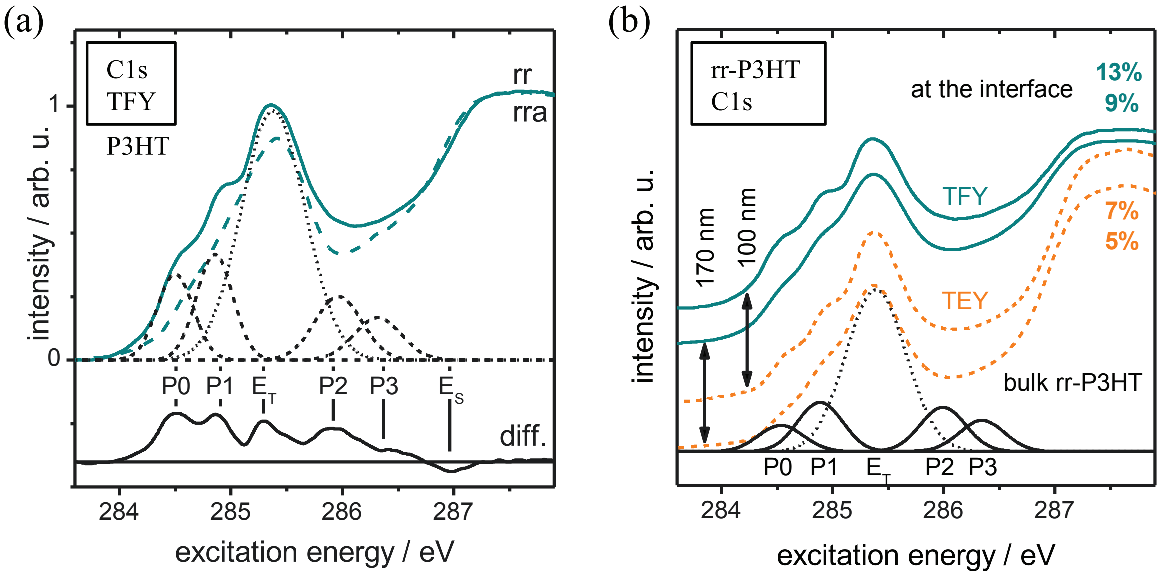

Figure 3.6: *XAS spectra of rr- and rra-P3HT as measured in TFY mode (a). The difference curve (bottom) of these two spectra shows the existence of six peaks (P_0, P_1, P_2, P_3, E_T, and E_S). For a quantitative analysis the spectra are normalized to the absorption at 287.6 eV. The contributions of P_0, P_1, P_2, and P_3 are decomposed by Gaussian curves for the quantitative analysis. The contributions marked E_T and E_S are assigned to Excitons.*

TEY/TFY-XAS spectra for two different rr-P3HT layer thicknesses (b). When increasing the information depth relative to the substrate interface, the 2D-Polaron intensity decreases. This gives evidence for a doping gradient. The extracted 2D-Polaron doping concentration for each spectra is labelled.

For both, the rr- and rra-P3HT films the XAS (TFY) spectra are shown in direct comparison in Figure 3.6a. The dominant features at the C1s edge are the peaks at 285.4 eV and around 287.6 eV, in agreement with energies reported in literature [TOU88], [WAT11]. Very remarkable is the double peak structure (P_0, P_1) on the rise of the leading absorption band for rr-P3HT. It is readily observed that these features are much weaker in the rra-P3HT films. Focusing on these peaks the difference curve of both data sets {Figure 3.6a (bottom)} is shown in addition in order to identify the major distinction between the two polymer structures in the region below 287 eV. The additional peaks of rr-P3HT in comparison to rra-P3HT are labelled P_0 (284.50 eV), P_1 (284.85 eV), P_2 (285.96 eV), P_3 (286.32 eV), E_T (285.4 eV), and E_S (287.2 eV) (Table 3.2).

In Figure 3.6b XAS data for two rr-P3HT films with different thickness are shown. The data clearly depict that the intensity of the polaronic states exhibit a gradient with distance to the interface. Here the bulk sensitive TFY probes the electronic structure closer to the interface. The surface sensitive TEY mode analyses the polymer apart from the interface. It is evident that the P_0 and P_1 features are more pronounced in the TFY mode rather than in the TEY mode of the same sample.

Table 3.2: *Energy positions and FWHM values of the Polaron and Exciton levels evaluated from Figure 3.6a.*

Level	**Excitation energy / eV**	**FWHM / eV**
P_0	284.50	0.4
P_1	284.85	0.4
P_2	285.96	0.5
P_3	286.32	0.5
E_T	285.40	0.6
E_S	287.20	1.9
CBM	287.6	-

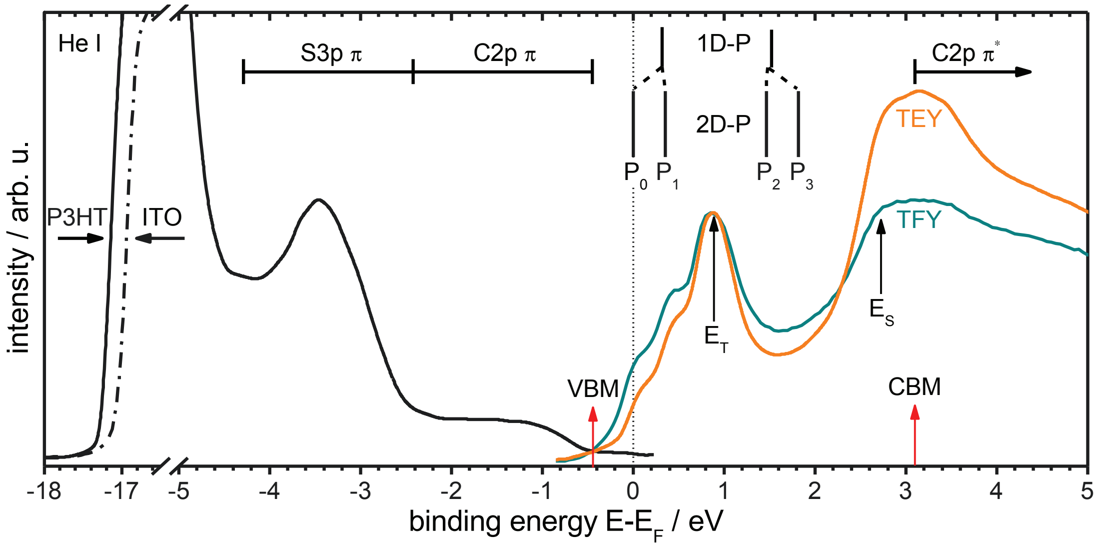

Figure 3.7: *Combined UPS (He I) and C1s XAS spectra for doped rr-P3HT. The solid lines show the TFY (green), TEY (orange) and UPS (black) spectra. Red arrows mark the VBM and CBM. The energy levels of 1D (P_1 and P_2) and 2D-Polarons (P_0, P_1, P_2, and P_3) are indicated by vertical lines; the features E_T and E_S are of excitonic nature and marked by black arrows. The SEO of P3HT on ITO and of plain ITO substrate (dashed line) are depicted.*

The combination of both the XAS and the UPS data enables the construction of the band scheme with the energy scale referred to the Fermi energy (Figure 3.7). The He-I valence band spectrum for rr-P3HT on ITO is also included in Figure 3.7. For the XAS spectra the Fermi energy is defined by $E_F = \hbar\omega - E_{C1s} \pm \Delta$. Some screening of the core hole is expected which is included in Δ. It is used to adjust the data to the differences that are expected by comparison with optical data as well as by the use of different physical pictures. In these data the term $E_{C1s} \pm \Delta$ was set to 284.5 eV. The screening Δ is about 0.3 eV and is in the order of the binding energy of E_S (0.4eV).

The position of the valence band minimum (VBM) is found to occur at -0.43 eV in agreement with previous work in our group [SCH03]. A work function of 3.93 eV for rr-P3HT on ITO is determined from the secondary electron onset (SEO). It is in good agreement with Xu et al. [XU09].

The CBM is assigned to the peak at 287.6 eV [FEN07], [DEI10]. From the VBM and the CBM difference an electronic band gap of about 3.5±0.2 eV is obtained for the doped rr-P3HT.

The observation of Polaron and Exciton features in the resPES profile, a photon in – electron out process, can be confirmed by resonant inelastic X-ray scattering (RIXS), a photon in – photon out process, in the next section.

3.1.5 RIXS

Resonant inelastic X-ray scattering as a photon in – photon out process is well suited to further clarify the existence of the polaronic and excitonic in-gap states.

In Figure 3.8a a RIXS map of rr-P3HT is shown. The emission signal only covers the region of the π- and σ-bands (285 eV – 270 eV). Here emission contributions of valence band π and σ states are found over the complete excitation energy range (284 eV – 300 eV).

In contrast, in the resPES spectra (Figure 3.4 and Figure 3.5b) these valence band π and σ states only show contributions at the two resonances E_T and E_S.

In respect to Figure 3.7 the position of the Fermi energy E_F, VBM, and CBM are indicated. RIXS agrees very well to these results obtained from UPS and XAS (TEY). Especially the CBM position is shown in RIXS by a characteristic branch of the Rayleigh line at an excitation energy of 287.6 eV.

Remarkably, the modulation of the elastic scattering channel (Rayleigh scattering; Figure 3.8b) is in agreement with the peak position of the polaronic (P_0 – P_3) and excitonic features (E_T and E_S). The elastic channel of RIXS gives further evidence about the assignment of these six features to Polarons and Excitons as they act as scattering centres in RIXS. This is another evidence for their localized nature.

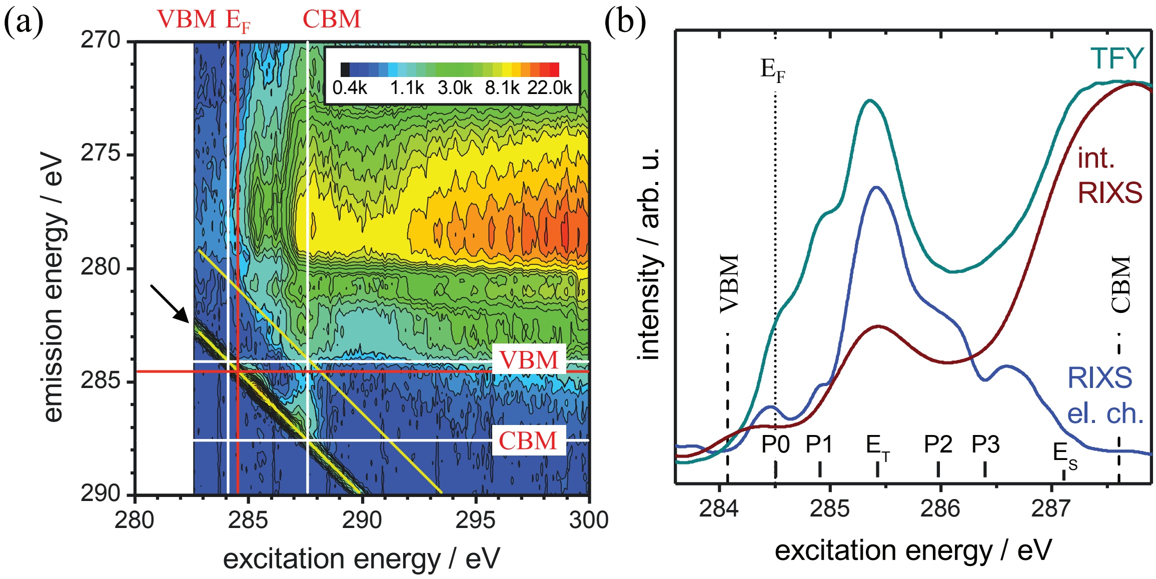

Figure 3.8: *Resonant Inelastic X-ray Scattering diagram of rr-P3HT*[***] *(a). Vertical and horizontal red lines indicate the position of the Fermi energy. In addition vertical and horizontal white lines depict the VBM and CBM. The black arrow marks the Rayleigh line (yellow line). A second yellow line parallel to the Rayleigh line depicts the Raman loss of the π-π* transition.*

Comparison of the elastic RIXS channel {Rayleigh line, indicated by the black arrow in (a)} to the TFY spectrum (green) and integrated RIXS spectrum (dark red) of rr-P3HT (b). Indicated are the peak positions of the polaronic (P_0 - P_3) and excitonic features (E_S and E_T), which are obtained by a quantitative analysis of the spectra in Figure 3.6 *(see* Table 3.2*).*

[***] RIXS measurements have been performed by Marcus Bär and Regan Wilks at beamline 8.0 (Advanced Light Source, Lawrence Berkeley National Laboratory, Berkeley, USA).

3.2 PCBM

3.2.1 XRD and UV-Vis

Phenyl-C61-butyric acid methyl ester was as well as P3HT briefly characterized by XRD and UV-Vis (Figure 3.9).

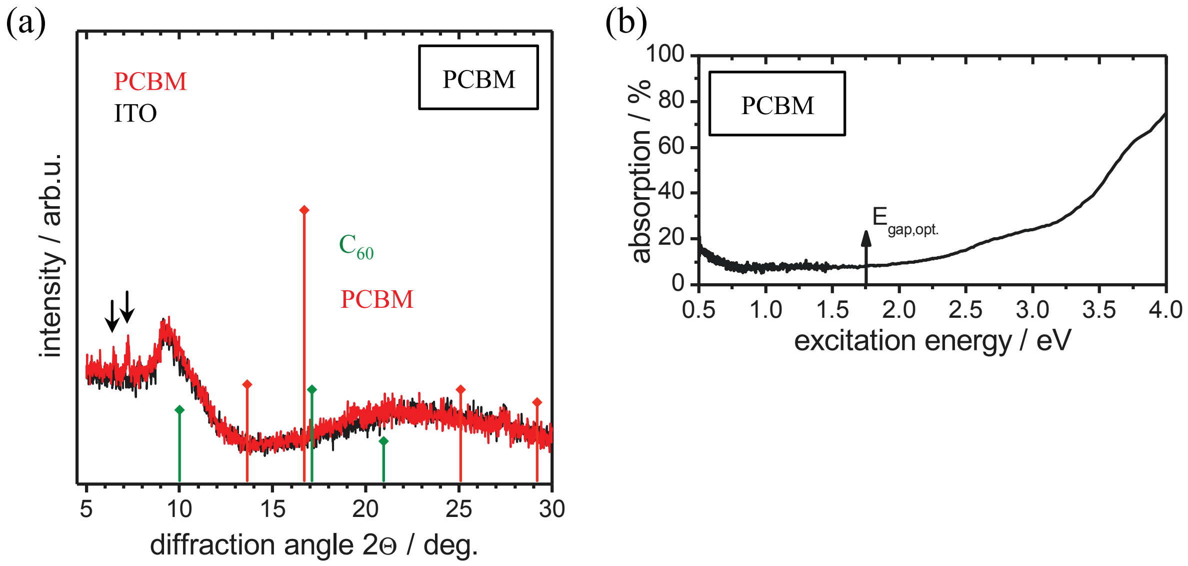

Figure 3.9: *X-ray Diffraction (Cu Kα) measurements*[†††] *of annealed PCBM and ITO (a). The 2Θ peak positions for C60 and PCBM were taken from [SUB02] and [KAR11], respectively. UV-Vis absorption spectra of PCBM*[‡‡‡] *(b).*

The XRD pattern of PCBM on ITO does not exhibit any of the reported characteristic peaks indicated by arrows in the graph (Figure 3.9a). Instead two small features are visible at 2Θ= 6.5° (1.36 nm) and 2Θ= 7.2° (1.23 nm) indicating that a small quantity of the PCBM layer is in a crystalline phase. These angles are around half of the reported values for PCBM (13.9° and 16.7°; 25.3° and 29.3°) [KAR11].

[†††] XRD measurements by Mathias Kappa (BTU Cottbus).

[‡‡‡] UV-Vis measurements of PCBM were performed by Shine Philip (BTU Cottbus) at HZB, Berlin-Wannsee.

From the UV-Vis absorption data of PCBM an absorption onset of 1.75 eV is obtained which is in agreement with the optical band gap of PCBM [PRE10], [ZOO09].

3.2.2 Core levels

In Figure 3.10 the O1s and C1s core level spectra of a pristine PCBM film are shown. A peak decomposition of the corresponding core level spectra was performed and is included in Figure 3.10. Voigt-profiles were used in this process.

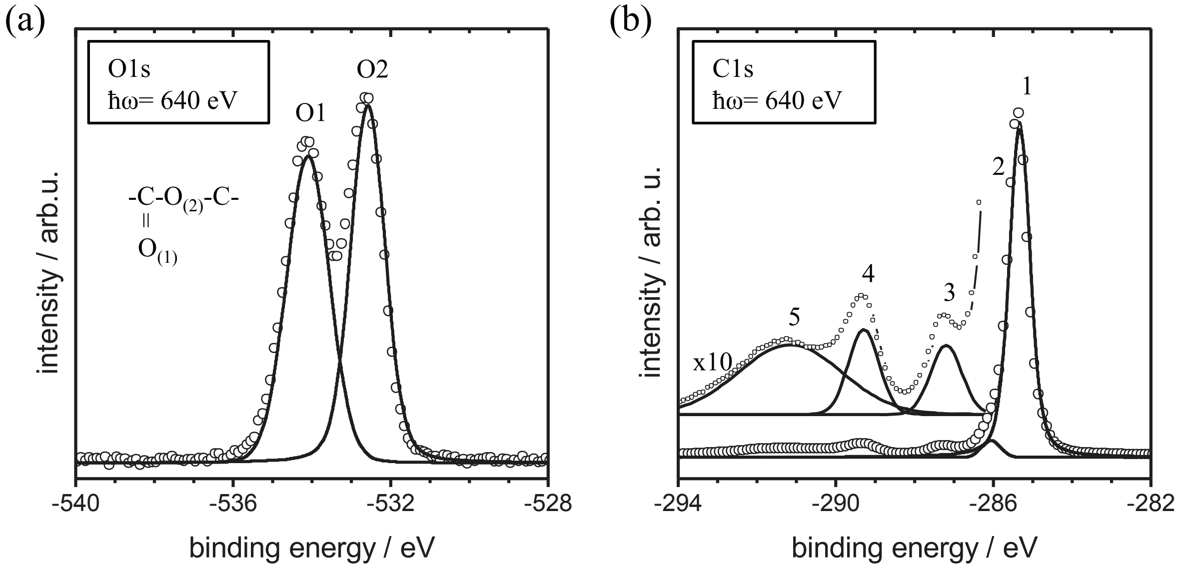

Figure 3.10: *O1s (a) and C1s (b) core level spectra of PCBM taken with an excitation energy of 640 eV. The circles represent the measurement data whereas the solid lines show the peak decomposition. The satellite structure (2-5) of the C1s core level is shown magnified.*

The peak positions and FWHM values of all contributions of the C1s and O1s core levels obtained from the peak decomposition are listed in Table 3.3.

The main C1s core level line is found at a binding energy of -285.3 eV (1). Satellites are visible on the higher binding energy side (2-5), which are characteristic for PCBM [FEL09]. The two oxygen contributions from the ester group indicated as O1 (-534.1 eV) and O2 (-532.6 eV) in the O1s spectrum in Figure 3.10 are well resolved with a splitting of 1.5 eV [LOP91].

Table 3.3: *Peak decomposition data of the C1s and O1s core levels shown in Figure 3.10.*

Peak	Assignment [FEL09], [LOP91]	Peak Position / eV	Area / % (FWHM / eV)
O1s (1)	C=O	-534.1	50 (1.20)
O1s (2)	C-O-C	-532.6	50 (0.79)
C1s (1)	C=C (C_{60})	-285.3	84 (0.61)
C1s (2)	C-C	-286.1	3 (0.54)
C1s (3)	C-O	-287.2	2 (0.93)
C1s (4)	C(O)O	-289.3	3 (0.91)
C1s (5)	Shake-up π-π*	-291.2	8 (3.0)

3.2.3 C1s resPES

For PCBM the resPES diagram is shown in Figure 3.11. In case of PCBM the C1s resPES diagram is rich on C1s-π* and C1s-σ* transitions. Thus the propagation of the resonant Auger decay is difficult to determine here.

In case of PCBM the different valence band (π and σ) and conduction band states (π* and σ*) are clearly visible. Their position is marked for further discussion in the next section by black arrows to the right and to the top of Figure 3.11.

Because of the high intensity of the molecular orbital transitions in the π*-band of PCBM (285 eV – 291 eV) the Auger transitions are hardly noticeable. The features propagating under 45° above 291 eV excitation energy are due to the carbon KLL Auger transition (2h final state, black arrow). Below 291 eV and above 285 eV, the KLL auger transition is shifted by 3 eV towards higher kinetic energy from E_{kin}= 264 eV to E_{kin}= 267 eV. A combined (S+P) Auger decay process (67.5°) in π*-band is hardly evident. Only the shifted KLL Auger decay indicates the presence of an (S+P) Auger decay process.

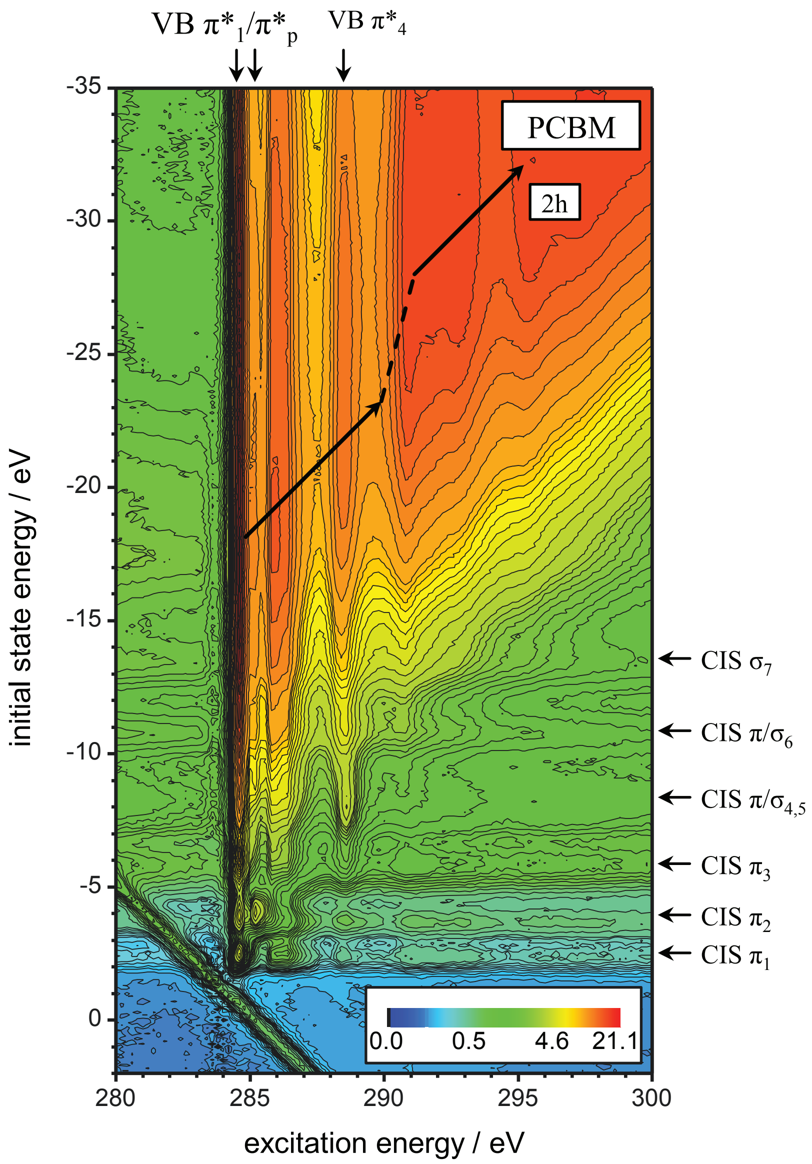

Figure 3.11: *resPES diagram of PCBM on ITO. The intensity of the signal is color-coded in a logarithmic scale. The CIS and VB spectra are taken from these data by horizontal and vertical cuts as indicated by the corresponding arrows. The black arrows indicate the 45° 2h (S) Auger process in the π*-and σ*-band. Indicated by the dashed line is the shift of the 2h (S) Auger decay between the π*- and σ*-band.*

3.2.4 Conduction and valence band

The valence band and conduction band spectra at the excitation and initial state energies marked in Figure 3.11 will be further used to evaluate the nature of the conduction and valence band states. Based on this discussion the position of the singlet Exciton level, its binding energy and the electronic band gap can be deduced.

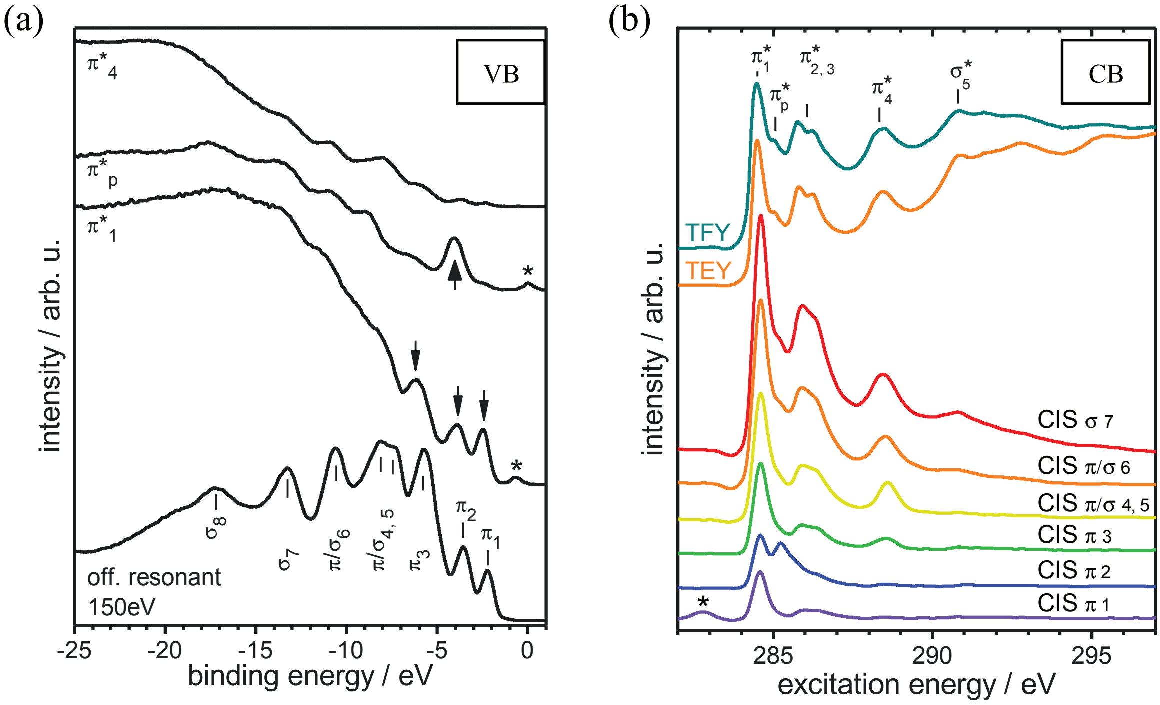

Figure 3.12: *Valence band (a) and Conduction band spectra (b) of PCBM. The VB data are taken from Figure 3.11 at various excitation energies as indicated in Figure 3.11. An additional off-resonance VB spectrum is included recorded at 150 eV. The CIS spectra are deduced from the resPES data as indicated by the arrows in Figure 3.11. In addition, the two upper curves correspond to the TEY and TFY XAS spectra (b). The peak assignment is shown in the off-resonant VB (a) and in the TFY data (b). The asterisk marks the second order of the C1s core level.*

In Figure 3.12a the valence band spectra of PCBM taken off-resonant at ħω= 150 eV and at resonance with ħω= 284.5 eV (π^*_1), 285.0 eV (π^*_p; phenyl side-group), and 288.4 eV (π^*_4) are shown. The valence band spectra at π^*_1 and π^*_p are significantly different to the other VBs at higher excitation energies. The π^*_1-VB exhibits three strong resonances corresponding to the π_1, π_2, and π_3-VB states, whereas the π^*_p-VB only exhibit an increase in photoemission for the second VB state (π_2). In contrast, no significant resonances are observed in the valence bands taken at excitation energies of higher unoccupied states than these two.

The conduction band of PCBM is represented by the XAS spectra in the total electron (TEY) and total fluorescence yield (TFY), which are shown in Figure 3.12b. The first six resonances are assigned to the π^*_1, π^*_p, $\pi^*_{2/3}$, π^*_4, and σ^*_5 band states [GER09], [KOL06], [PUT04]. The CIS spectra at VB states as indicated in the 150 eV spectra of Figure 3.12a are included in Figure 3.12b, too. These spectra are significantly different to the TEY and TFY spectra as they show the coupling of the respective VB state into the various CB states. The first π_1 VB state couples only into the first π^*_1 resonance, i.e. the π-π^* transition (π^* Exciton).

For the higher VB states with admixture of σ-character ($\pi/\sigma_{4,5}$, π/σ_6, σ_7) also the coupling into the higher π^* states is observed.

From the data it can be concluded that the π-system of the side group shows no overlap with the π-system of the fullerene as discussed later. The π_2 (primary phenyl) state couples only into the general excitonic state π^*_1 and into its own unoccupied band (π^*_p).

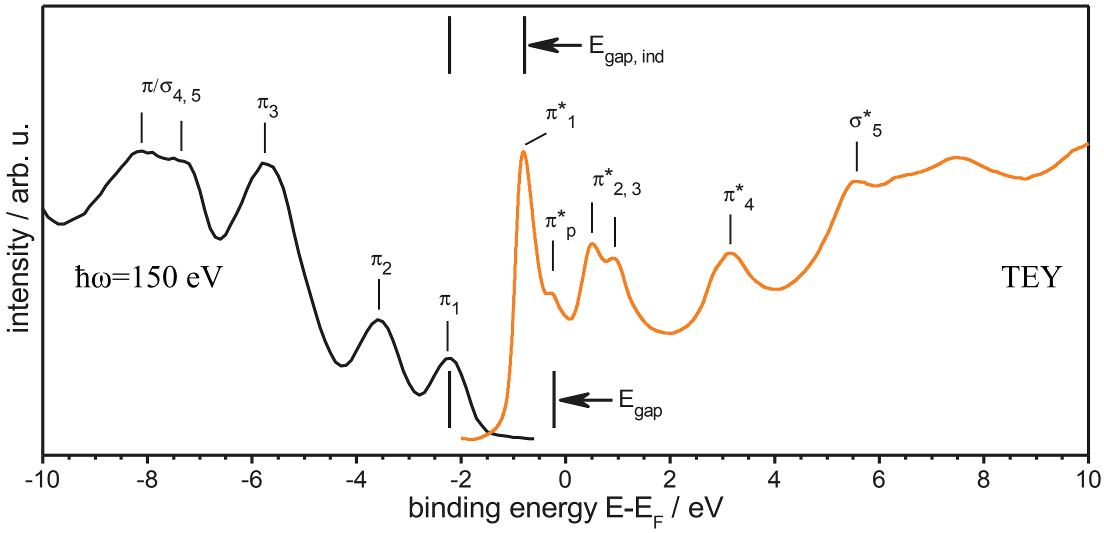

Figure 3.13: *Combined data of the occupied (valence band at 150 eV excitation) and unoccupied states (conduction band, TEY at C1s edge) of PCBM. Both spectra are referred to the Fermi energy. The CB and VB states are assigned as listed in Table 3.4. The indirect band gap* $E_{gap,ind}$= *1.4±0.1 eV and direct band gap* E_{gap}= *2.0±0.1 eV are indicated.*

The electronic structure of PCBM can be constructed by the combination of the valence band and XAS spectra (Figure 3.13). Both spectra can be referred to the Fermi energy. For the XAS spectra the Fermi energy is defined by $E_F = \hbar\omega - E_{C1s}$. In this case a value of $E_{C1s} = 285.3$ eV was determined from core level and resPES measurements (Figure 3.10b and Figure 3.11).

The assignment of the π- or σ-character to the individual peaks is done using the resonant valence band spectra and the CIS spectra of the corresponding peaks. The S and (S+P) Auger gives also an instrument for this classification. Based on these observations the peaks are assigned in Figure 3.13.

The occupied/unoccupied π- and σ-band system of PCBM resembles the one of C_{60}, showing the minor influence of the side group on the sp^2-hybridized system as shown in [Frie11]. This is also evident from the CIS spectra. Only the π_2 and π^*_p can be assigned to arise partly from states of the side group.

With both, occupied and unoccupied states referred to the same energy scale, the electronic band gap as the energy difference between the VBM and the CBM can be extracted. As shown in Figure 3.13 the band gap is almost completely filled with states. These states can be assigned to scattering, defects or to excitonic excitation as discussed later. The value of $E_{gap,ind} = 1.4 \pm 0.1$ eV, as the distance of the π_1 and π^*_1 peak maxima, corresponds to the theoretical value of the indirect band gap in a PCBM crystal [NAP08]. Considering the first CB state π^*_1 as an excitonic state inside the gap the band gap is the distance between π_1 and π^*_p carrying a value of $E_{gap} = 2.0 \pm 0.1$ eV, which is in agreement with other experimental values [KOS06]. Both E_{gap} and $E_{gap,ind}$ are indicated in Figure 3.13.

Table 3.4: *Peak assignment of the VB and CB spectra.*

Character	**VB peak position [eV]**	**CB peak position [eV]**
Pure π and π^*	-2.2: π_1 C_{60} -3.6: π_2 phenyl	284.5: π^*_1 Exciton 285.0: π^*_p phenyl 285.8: π^*_2 C_{60} 286.2: π^*_3 C_{60} 288.4: π^*_4 C_{60}
Overlap of π and σ	-5.7: π_3 (σ) C_{60} -7.4: π/σ_4 C_{60} -8.1: π/σ_5 C_{60} -10.6: π/σ_6 C_{60}	-
Pure σ and σ^*	-13.3: σ_7 C_{60} -17.2: σ_8 C_{60}	290.8: σ^*_5 C_{60}

Next, the result of the second class of materials will be presented starting with HOPG and Graphene flakes.

3.3 Graphene

For the different Graphene systems a comparison of their C1s core level and C1s XAS spectra is done before the resPES results for each system are discussed individually.

The resonant decay process at the C1s edge is discussed starting with Highly Ordered Pyrolytic Graphite as the basis and model system for further investigations of Graphene. It is further discussed for two grades of Graphene flakes and for monolayer Graphene on three different substrates (Ni, Cu, and SiO_2).

The single layers of the multi layer system of HOPG are bound among each other by van der Waals forces. Hence, in HOPG additional interlayer interactions are present that will influence the Auger decay processes in a similar way as the π-π stacking of rr-P3HT.

3.3.1 C1s core level and XAS

For HOPG and the different Graphene systems it is useful to have a comparative study of their C1s core level and properties because of their similarities in the structure. Likewise a comparison of the total electron yield X-ray absorption spectra of these systems is valuable.

In Figure 3.14a a direct comparison of the C1s core levels of Graphene flakes, HOPG, and monolayer (ML) Graphene on different substrates obtained by synchrotron PES with an excitation energy of $\hbar\omega$= 450 eV is shown. This comparison shows the high quality of the films obtained by the heat treatment of the Graphene flakes. The obtained FWHM values are: $FWHM_{HOPG}$= 0.23 eV; $FWHM_{ML/SiO2}$= 0.66 eV; $FWHM_{ML/Cu}$= 0.59 eV; $FWHM_{ML/Ni}$= 0.51 eV. For more details see Table 3.5.

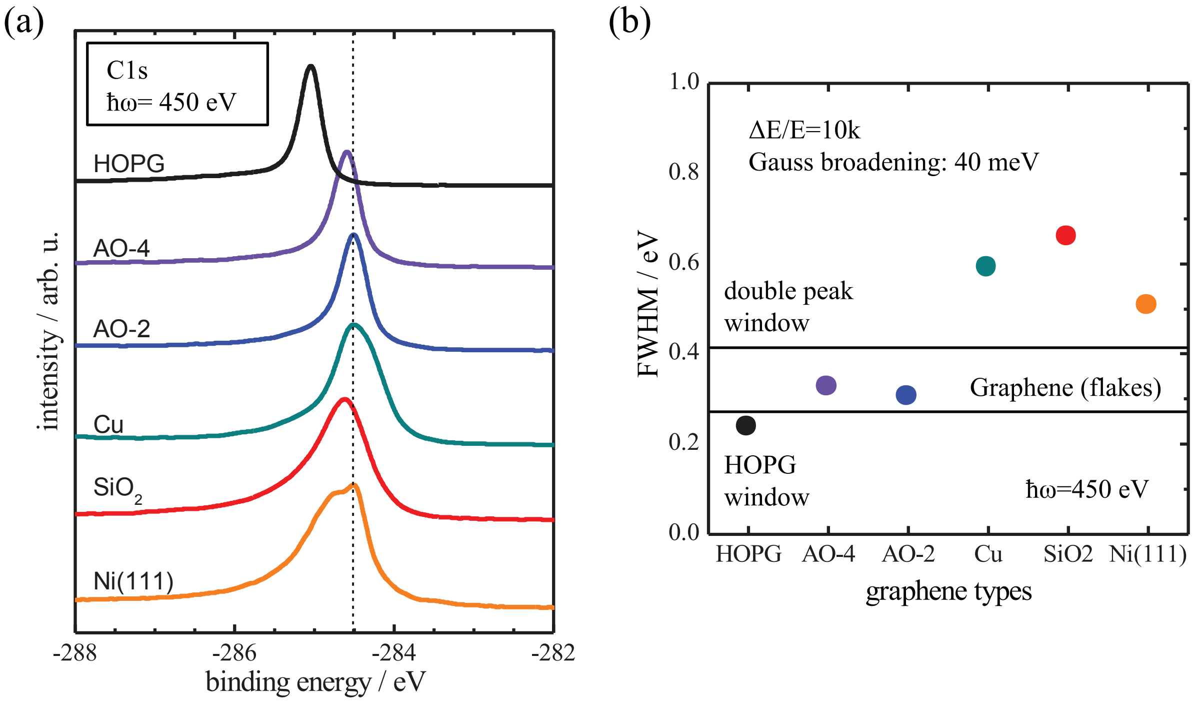

Figure 3.14: *A comparison of C1s core level spectra obtained from synchrotron measurements is given for HOPG, AO-2 (1000 °C), AO-4 (1000 °C), and ML Graphene on Ni(111), Cu, and SiO_2 (a). FWHM of the main C1s line for the different Graphene types (b).*

Table 3.5: *Binding Energy, FWHM, and asymmetry factor α of the C1s core level recorded with a excitation energy of 450 eV (see Figure 3.14) of different types of Graphene. Doniach Sunjic line profiles were used for the peak analysis.*

Sample	**Binding energy / eV**	**FWHM / meV**	**α**
HOPG	-285.0	235	0.058
Flakes AO-4	-284.6	303	0.060
Flakes AO-2	-284.5	325	0.090
ML/Cu	-284.5	590	0.069
ML/SiO_2	-284.6	657	0.057
ML/Ni(111)	-284.9 / -284.5	2x 505 (total 900)	0.046

For an easy comparison the FWHM values of the different systems are displayed in Figure 3.14b. In this comparative study the C1s core level for the HOPG sample has the smallest width. Here the FWHM is 0.23 eV with a Doniach Sunjic asymmetry factor α of 0.058.

Graphene flakes exhibit a FWHM of 300 meV after annealing. Their line shape is highly asymmetric ($\alpha_{AO\text{-}4}$= 0.06, $\alpha_{AO\text{-}2}$= 0.09).

The FWHM for the Graphene systems on Cu, SiO_2, Ni(111) is found to be much larger. In all systems the asymmetry factors α are similar (α_{Cu}= 0.069, α_{SiO2}= 0.057, $\alpha_{Ni(111)}$= 0.046).

In comparison, in the work of Christian Riedl [RIE10], he obtained a FWHM of 0.56 eV (α= 0.03) for mono- and 0.53 eV (α= 0.03) for bilayer epitaxial Graphene on SiC(0001) at an excitation energy of 600 eV. For hydrogen treated epitaxial Graphene on SiC(0001) Riedl deduced a FWHM of 0.28 eV (α= 0.04) for lifted bilayer and 0.34 - 0.42 eV (α= 0.04) for monolayer Graphene at an excitation energy of 450 eV.

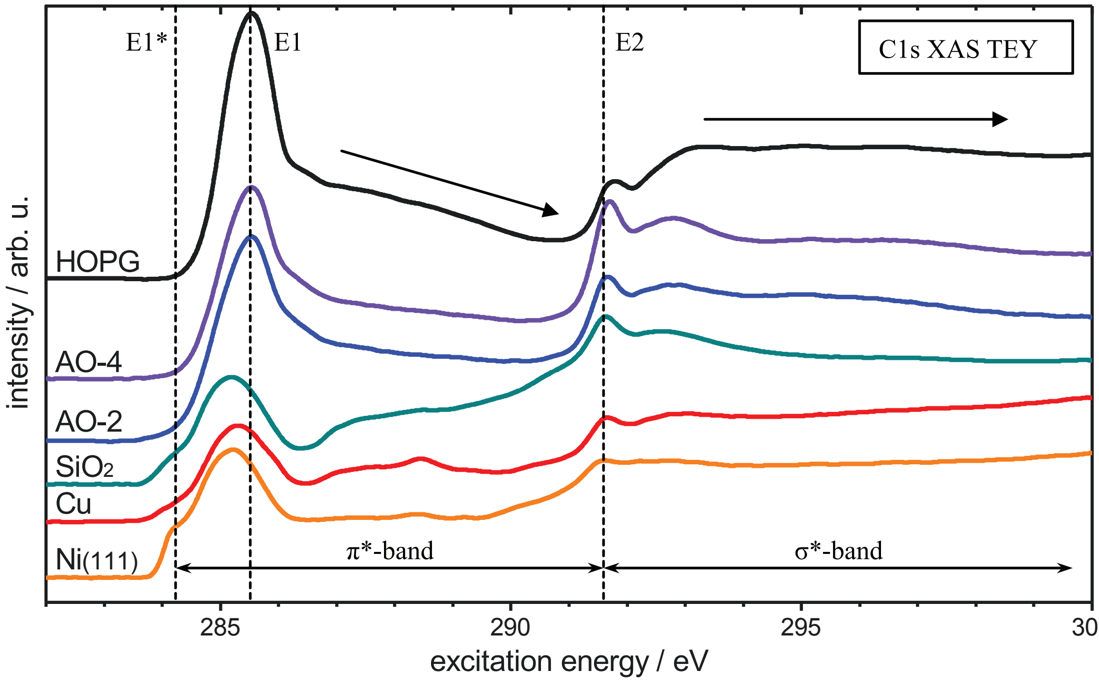

Figure 3.15: *X-ray absorption spectra at the carbon K-edge of different Graphene types in the total electron yield mode. The black arrows indicate the Auger decay plateaus.*

In Figure 3.15 the X-ray absorption spectra at the carbon K-edge in the total electron yield mode for different Graphene types is shown. To compensate the strong polarization dependence of π*- and σ*-resonances the magic angle of 54.7° was chosen. The XAS-TEY spectra can be referred to the Fermi energy by the binding energy of the C1s core level (Table 3.5).

The XAS of HOPG is showing two characteristic resonance features at 285.5 eV and 292 eV labelled with E1 and E2 in Figure 3.15. The plateau between these two features is showing a decrease in intensity with increased excitation energy. In contrast, this is not observed for the plateau above 292 eV (see arrows in Figure 3.15). The former is characteristic for the multiple Auger decay with a three-hole final state. The normal Auger decay with a two hole final state is characterized by a constant intensity.

When moving over to Graphene flakes the intensity of the Auger decay between the two resonance features E1 and E2 is increased.

The intensity ratio of E1 to the Auger (height of the Gaussian step function in the π*-region) is reduced from 6.6 for HOPG to 1.9 for Nickel (Table 3.6). The FWHM of the main E1 peak for all carbon thin films is increased from 1.0 eV for HOPG to 1.2 eV Ni(111) showing a lower lifetime for the ML Graphene ($\tau \propto 1/\Gamma$). A higher FWHM is an indication of reduced multiple Auger decay (S+P).

In contrast to HOPG a new feature E1* is evolving at 284.1 eV in the TEY XAS spectra, characteristic for Graphene, which has an intensity contribution of about 5 %.

Table 3.6: *Intensity ratio of the first XAS resonance at 285 eV (E1) and the Auger decay. In addition the FWHM of E1 is given. The shoulder (E1*) has an intensity contribution of about 5 % to the resonance E1.*

Sample	**Exciton intensity**	**E1 (E1*) FWHM / eV**
HOPG	6.6	1.00
Flakes AO-4	3.3	1.09
Flakes AO-2	2.1	1.18
ML/Cu	2.3	1.21 (0.46)
ML/SiO_2	2.8	1.21 (0.37)
ML/Ni(111)	1.9	1.22 (0.32)

Next a more detailed analysis of the resonant photoemission profiles of the individual Graphene Systems is presented.

3.3.2 HOPG

The surface of the used HOPG crystal was pre-characterized by AFM for control of the surface quality.

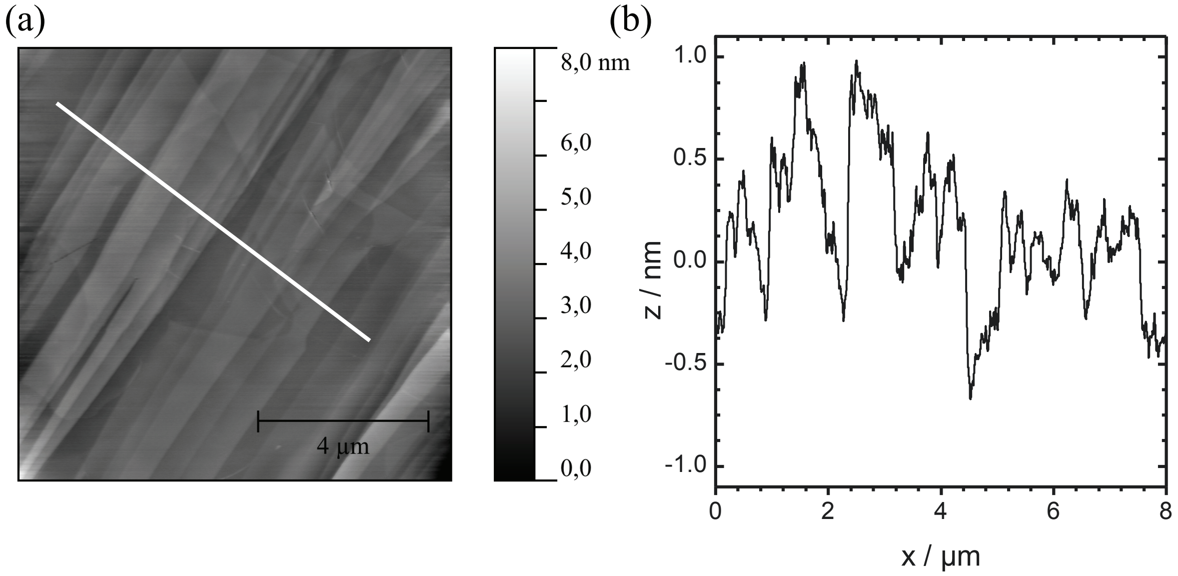

Figure 3.16: *Atomic force microscopy image (a) and extracted height profile (b) of the surface of the investigated HOPG sample.*

In Figure 3.16a an AFM image of the surface of the HOPG sample is depicted. A height profile extracted from the image (white line) is shown in Figure 3.16b. Terraces, steps, and kinks are visible due to the preparation by the scotch tape method [GEI11].

3.3.2.1 C1s resPES diagram

The resPES diagram of HOPG at the carbon K-edge is shown in Figure 3.17.

The (C1s-C2p-C2p)-KLL Auger decay line with a kinetic energy of 264 eV becomes evident in the resPES diagram as a line following an angle of 45° {2h (S) Auger decay}. These Auger decay lines are observed for excitation energies above 292 eV (σ*-region) only.

Below a excitation energy of 292 eV and above 285 eV (π*-region) the spectator Auger decay is shifted by 3 eV to a higher kinetic energy of 267eV. In addition, two different Auger decays are evident. They have a slope of 67.5° (3h) and 78.75° (4h) and are attributed to an (S+P) and an (S+S) combined Auger decay (Chapter 4.2.2.1 and 4.2.2.2), respectively. This behaviour indicates that there must be different mechanisms or different states involved in the resonant behaviour in the π*-region.

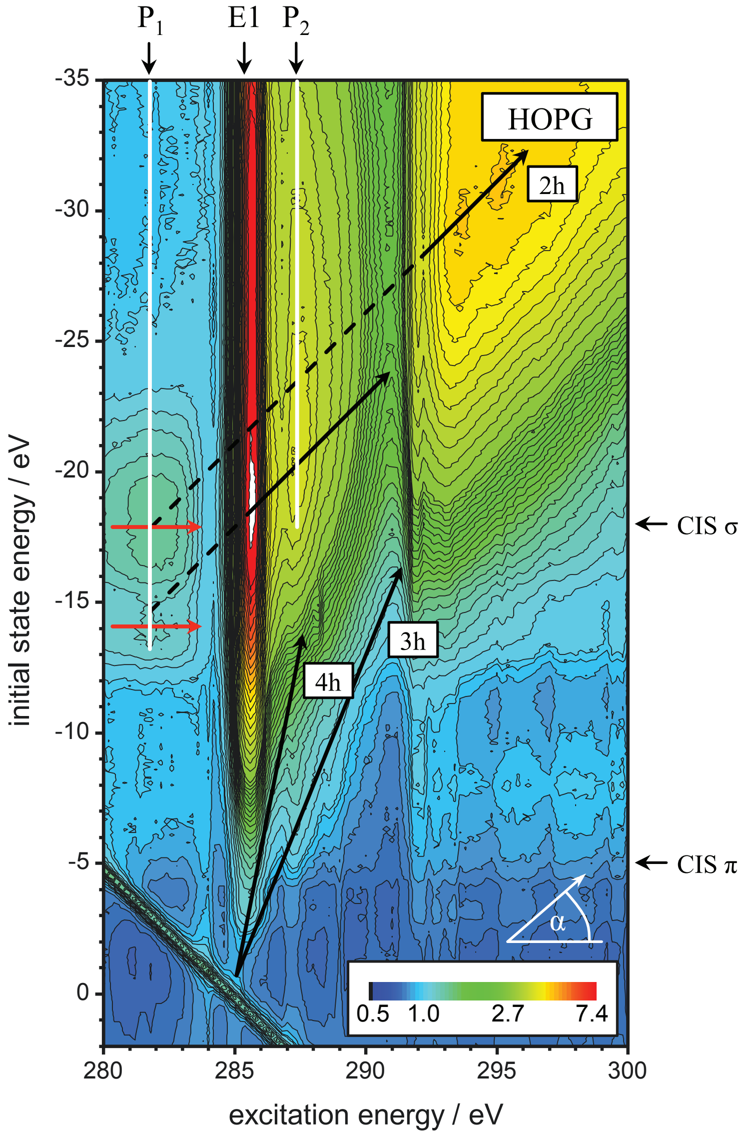

Figure 3.17: *resPES diagram of HOPG*[§§§]*. Black arrows indicate the individual multiple Auger decays. The vertical white lines show the position of polaronic resonances P*$_1$ *and P*$_2$ *at the Γ-point and the two red arrows indicate two valence states with a FANO profile. The 2h (S) Auger is shifted between the π*- and σ*-band. Indicated by the dashed lines are the principal VB states involved in the decay process and the shift of the 2h (S) Auger decay between π*- and σ*-band. To the right the position of the CIS spectra for π and σ states is indicated.*

[§§§] Raw Data of HOPG was recorded by Daniel Friedrich (BTU Cottbus).

The first resonance appears at 285.5 eV and marks the beginning of the π*-band. A second resonance is found at 292 eV which assigns the beginning of the σ*-bands. Both resonances give rise to an Auger decay and can be attributed to a π*- and σ*-resonance (E1 and E2), respectively. The latter is generally attributed to be of excitonic nature (E2) and the former to the 1s-π* 'white band' transition showing strong polarization dependence with excitonic contributions [BRU95], [BRU02], [CHO12], [MED09].

The term "Exciton" represents a quasi-particle stabilized by Coulomb interactions and is considered to exist in the band gap. In terms of resonant PES an Exciton is a state in which the excited electron is trapped and does not contribute to the decay channel. The lifetime of the trapped state is longer than the Auger decay lifetime (τ_{Auger}, Table 2.1).

In a semi-metal there should be no excitonic state. However, for graphite, for Graphene, and for HOPG there exists a band gap at the M point which is around E_{BG}= 4.7 eV [CAR95], [CHA11]. This gap would be sufficient for the creation of an Exciton but requires higher excitation energy for its excitation. Furthermore, for few-layer Graphene or due to substrate interaction with the carbon layers a band gap opens up at the K-point [ALZ09], [GIO07], [LUI11], [RUT11], [ZHO07].

Below the first resonance (285.5 eV) at an initial state energy region of -15 eV – -20 eV a strong FANO type resonance is found as indicated by the two red arrows in Figure 3.17. In the resPES diagram this is indicated by a dip in intensity prior to the absorption edge in the corresponding CIS spectrum (see Figure 4.4).

Both the shifted Auger transition and the FANO resonance are considered in the (S+P) Auger decay model.

Close to the position of the FANO resonance two resonances are found at -14 eV and -17 eV initial state energy prior to the first π*-resonance at 285.5 eV. These resonances are an indication of polaronic levels at the Γ-point (compare to Figure 1.7c). For Polarons two levels are expected in the band gap. The first polaronic level is the one observed at the FANO resonance at an excitation energy of 282 eV; the second level is found at a excitation energy of 288 eV as indicated in Figure 3.17 by P_1 and P_2. As evident the pre-edge Polaron resonances, in particular the corresponding valence band states at the Γ-point, give rise to a spectator Auger decay at the C1s core level threshold.

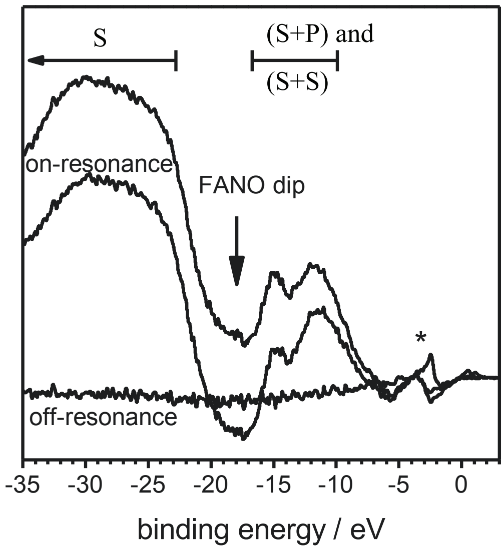

Figure 3.18: *Auger contribution spectra at the C1s edge of HOPG at 282 eV (off-resonance), 285 eV (on-resonance), and 285.6 eV (on-resonance). Four features are visible: 2nd order excitation of the C1s core level (0 – -5 eV), (S+P) and (S+S) Auger decay (-5 – -16 eV), FANO-Resonance at -18 eV, and KLL spectator Auger decay (S) starting at around -19 eV (E_{kin}= 267 eV). The normal Auger is at -22 eV (E_{kin}= 264 eV). The asterisk marks the 2nd order of the C1s core level.*

The Auger contributions of the first resonance at 285 eV are shown in Figure 3.18. The spectra can be divided into four regions. From 0 eV to -5 eV the 2nd order excitation of the C1s core level is evident, from -5 eV to -16 eV a spectator and participator decay channel of the (S+P) and (S+S) Auger decay followed by a FANO dip is found and from -20 eV onward the normal C1s KLL spectator Auger decay is observed. The latter three regions are all evident for the (S+P) Auger decay and the (S+S) Auger decay that are visible in Figure 3.17.

The second order excitation of the C1s core level is found in Figure 3.17 in the lower left corner. For initial state energy of zero the corresponding excitation energy on this line corresponds to the binding energy of the core level. Here a value of E_{bind}= -285 eV is obtained for the binding energy of the C1s core level in agreement with XPS C1s core level measurements. This indicates that no excitonic shift is present in the resPES diagram. With the knowledge of the binding energy of the core level the XAS spectra, the CIS spectra, the

CFS spectra, and the position of all molecular bands can be referred to the Fermi energy in the next section.

3.3.2.2 Conduction and valence band

Valence band spectra and conduction band spectra of HOPG are referred to the same energy scale by use of the excitation energy value of the second order excitation at zero initial state energy (285.0 eV, see Figure 3.17) (i.e. the binding energy of the C1s core level).

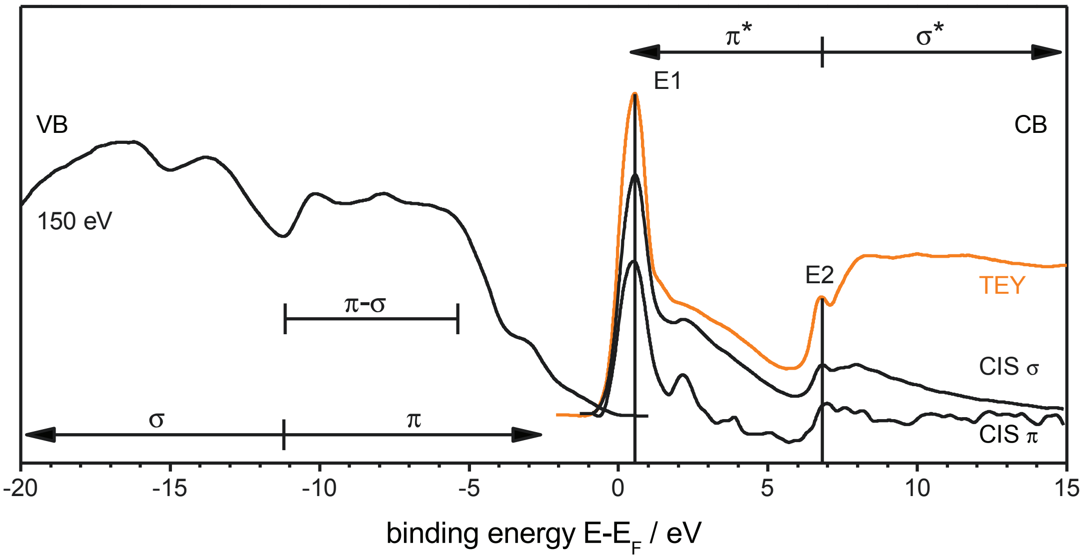

Figure 3.19: *A combined spectrum of the occupied (valence band at 150 eV excitation) and unoccupied states (conduction band, TEY at C1s edge, and constant initial state spectrum of the π-band and σ-band) of HOPG. All spectra are referred to the Fermi energy. The excitonic levels are marked with E1 (+0.5 eV) and E2 (+7 eV).*

In Figure 3.19 a combination of XPS (VB) and XAS (CB) data in reference to the Fermi energy is given showing the density of states around the Fermi energy. The π- and σ-CIS spectra are taken from the resPES diagram (Figure 3.17) whereas the TEY, the XAS, and the valence band with an excitation energy of ħω= 150 eV are recorded separately. The assignment of the occupied and unoccupied states can be partially derived from the resPES diagram. Further assignments are taken from references [CAR95], [MA99], [NEG06]. The occupied π-bands of HOPG appear between 0 eV and -11 eV whereas the pure σ-bands are assigned to the features above -11 eV. Intermixing of both bands is given between -5 eV and -11 eV, as shown by band structure calculation and angle resolved photoemission measurements [CAR95], [NEG06]. The excitonic features E1 (285.5 eV) and E2 (292 eV) separate the unoccupied π*- and σ*-bands from each other.

3.3.3 Graphene flakes

The size of both Graphene Flakes grade AO-2 and AO-4 can be deduced by AFM.

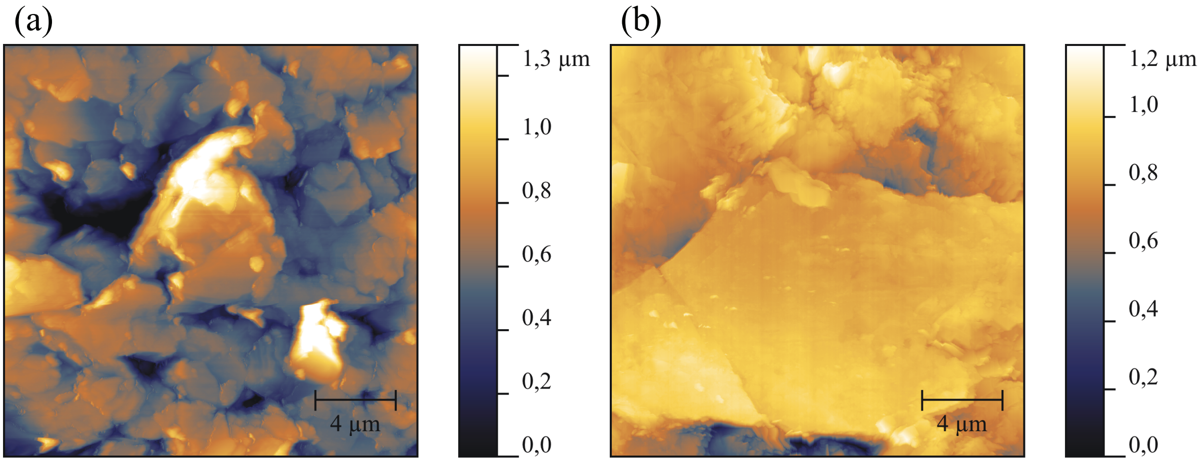

Figure 3.20: *AFM images of Graphene flakes grade AO-4 (a) and AO-2 (b).*

AFM images of the Graphene flakes grade AO-4 and AO-2 are given in Figure 3.20a and b, respectively. The lateral dimension for AO-4 is about 2–4 µm and for AO-2 about 20 µm.

3.3.3.1 C1s resPES diagram

Already the C1s core level and C1s TEY XAS spectra indicated a very similar spectroscopic characteristic for both flakes, even so the size of the Graphene flakes grade AO-4 is only a fifth to tenth of the size of Graphene flakes grade AO-2. The spectroscopic similarities are sustained also for the resonant photoemission profile at the C1s core level threshold.

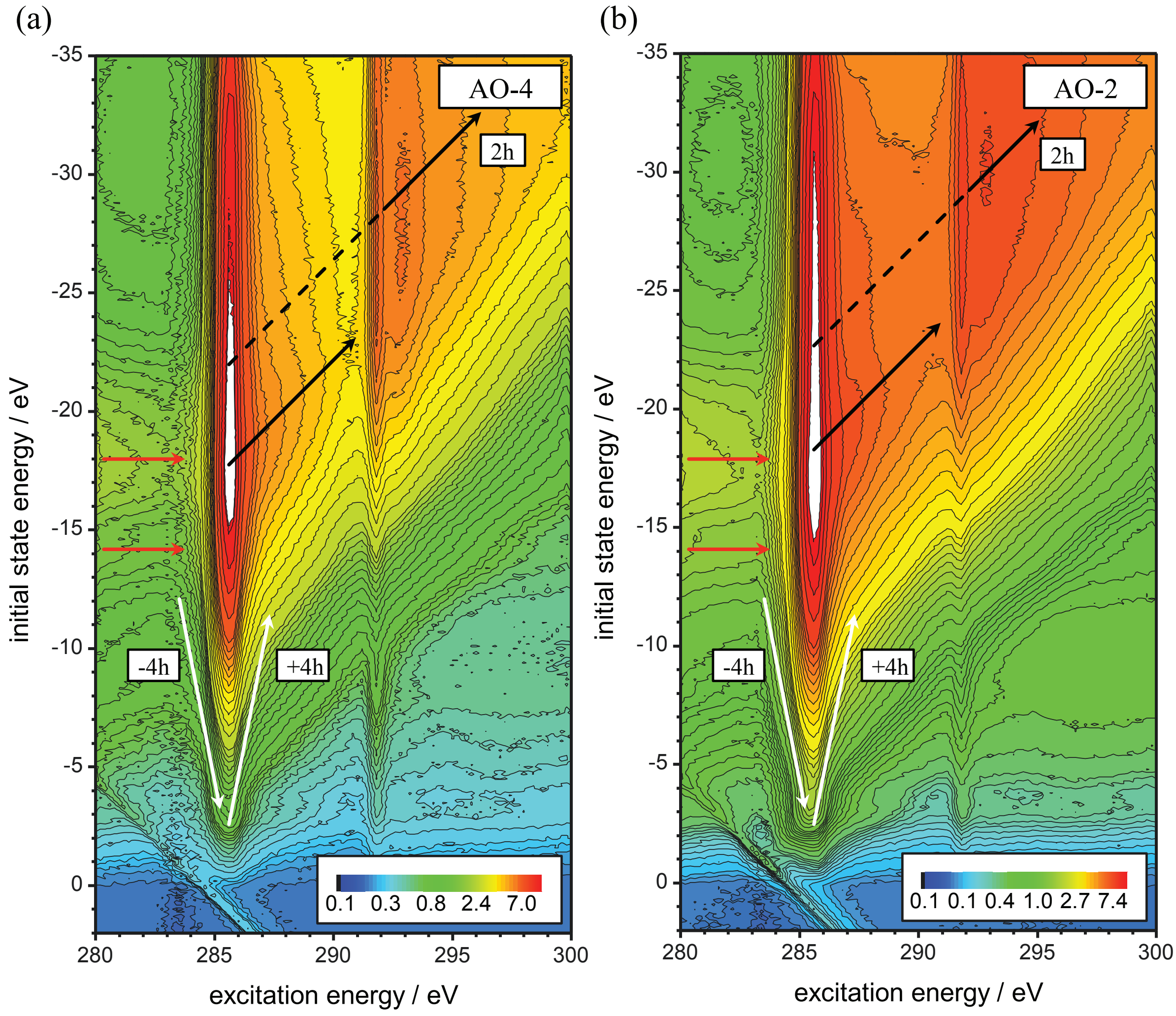

Figure 3.21: *ResPES diagram of Graphene flakes grade AO-4 (a) and grade AO-2 (b). The intensity of the signal is given in logarithmic scale and colour scale contours. Black arrows indicate the 2h (S) Auger decay, white arrows the ±4h decay, and the two red arrows indicate two valence states with a FANO profile. Indicated by the dashed line is the shift of the 2h (S) Auger decay between π* and σ*-band.*

The resPES diagram of Graphene flakes grade AO-4 and AO-2 are plotted in Figure 3.21.
In all data the first (π*-) resonance appears at around 285.5 eV. There is a second (σ*-) resonance at an excitation energy of 291.5 eV. The plots are dominated by the appearance of the broad C-KLL Auger emission {2h (S) final state} which is indicated by the black arrows in both the π*- and σ*-band. In the π*- band the C-KLL is shifted by 4 eV to a higher kinetic of $E_{kin,\pi*}$= 267 eV compared to the σ*-band with a kinetic energy of $E_{kin,\sigma*}$= 263 eV.

At the first resonance at 285.5 eV at the lower binding energy end close to the Fermi energy a V-shape decay is observed indicated by the white arrows which propagate under an angle $\alpha = \pm 78.75°$. The Graphene flakes show in addition in the pre-resonance region at -15 eV to -20 eV initial state energy a shallow FANO type resonance that is indicating a discrete state in the band gap at the M-point [FAN66], [CHA11].

For both Graphene flakes the second order excitation of the C1s core level crosses the Fermi energy of the initial state axis at an excitation energy of 284.5 eV. This value agrees well with the C1s core level binding energy. Hence, the binding energy of the C1s core level can be used for referencing the respective X-ray absorption spectra to the Fermi energy.

3.3.3.2 Conduction and valence band

The C1s core level binding energy deduced from the resPES profile measurements is used in the following to combine both valence and conduction band of both Graphene flakes on the same binding energy scale.

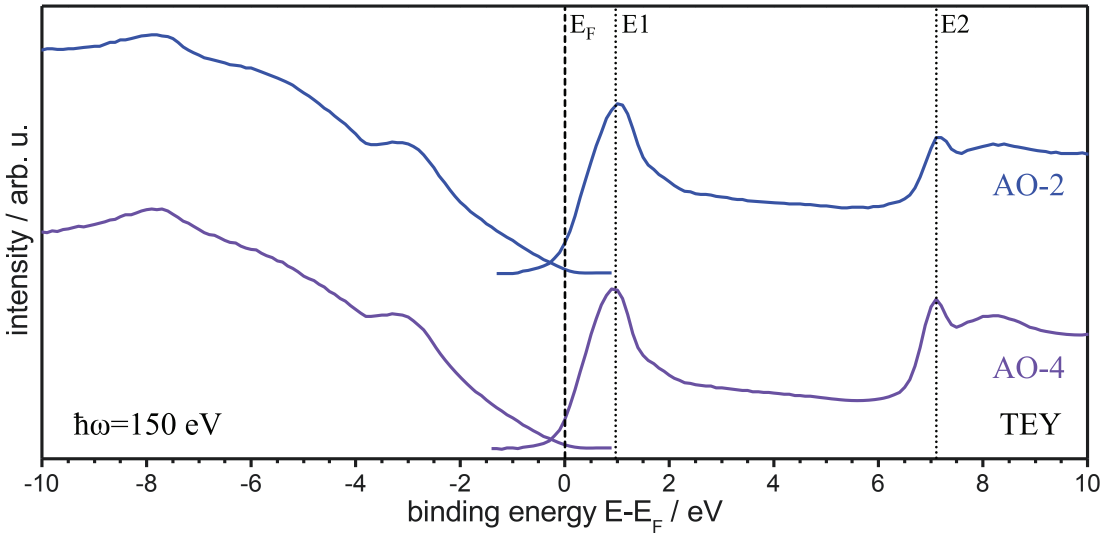

Figure 3.22: *A combined spectrum of the occupied (valence band at 150 eV excitation) and unoccupied states (conduction band, TEY at C1s edge) of Graphene flakes type AO-4 and AO-2. All spectra are referred to the Fermi energy with the help of the binding energy of the C1s core level (Table 3.5). The excitonic levels are marked with E1 (+1 eV) and E2 (+7 eV).*

In Figure 3.22 a combination of XPS (VB) and XAS (CB) data in reference to the Fermi energy is given for Graphene flakes grade AO-4 and AO-2 showing the density of states around the Fermi energy. The excitonic features E1 at +1 eV (285.5 eV) and E2 at +7 eV (291.5 eV) separate the unoccupied π*- and σ*-bands from each other.

The size of the Graphene flakes has no apparent influence of the valence and conduction band for both grades of Graphene flakes. For both Graphene flakes, AO-4 and AO-2 no conduction band states below the Fermi energy are evident.

3.3.4 Monolayer Graphene

In the case of monolayer Graphene on nickel, on copper, and on SiO_2 no AFM images were taken. Still, the high quality of these samples was ensured by pre-characterization of these samples by their respective manufacturer.

3.3.4.1 C1s resPES diagram

In contrast to Graphene flakes the C1s core level of monolayer Graphene were considerable broadened (Figure 3.14). Also in the C1s TEY XAS spectra of monolayer Graphene the first π*-resonance E1 is red shifted and shows a characteristic pre-edge feature E1* (Figure 3.15). Hence, the C1s resPES profile of monolayer Graphene is considered to exhibit significant differences compared to Graphene flakes (Figure 3.21).

For monolayer Graphene on Ni(111), on copper, and on SiO_2 the resPES diagrams are shown in Figure 3.23. It is remarkable that the general Auger pattern for the monolayer Graphene samples displays significant differences than for Graphene flakes.

The resPES data of ML Graphene do not show an Auger decay in the π*-band. Instead a strong excitonic feature above 285 eV is found. The 2h (S) KLL-Auger only appears above the σ*-resonance. Furthermore, the V-shape at the π*-resonance is not observed as the FANO resonance at the CIS(-17 eV) σ–states is suppressed.

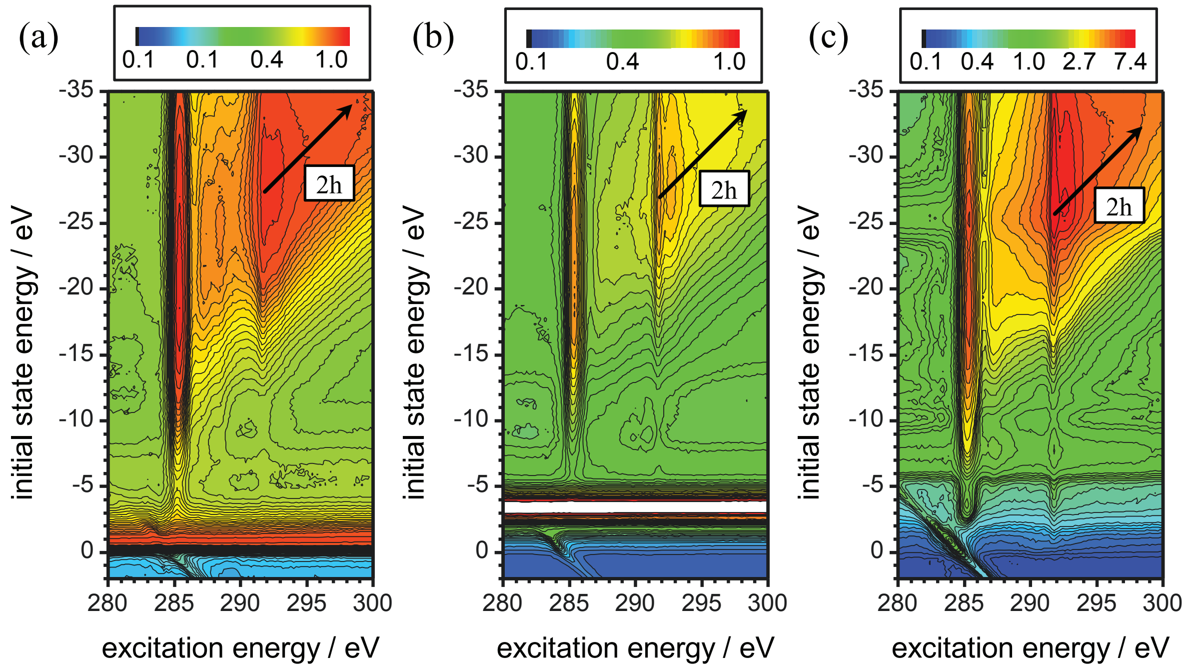

Figure 3.23: *ResPES diagram of ML Graphene on Ni(111) (a), on Cu (b), and on SiO_2 (c). The intensity of the signal is given in logarithmic scale and colour scale contours. The black arrow indicates the 2h (S) Auger decay.*

3.3.4.2 Conduction and valence band

In Figure 3.24 a combination of XPS (VB) and XAS (CB) data in reference to the Fermi energy is given for ML Graphene on Ni(111), Cu, and SiO_2 showing the density of states around the Fermi energy.

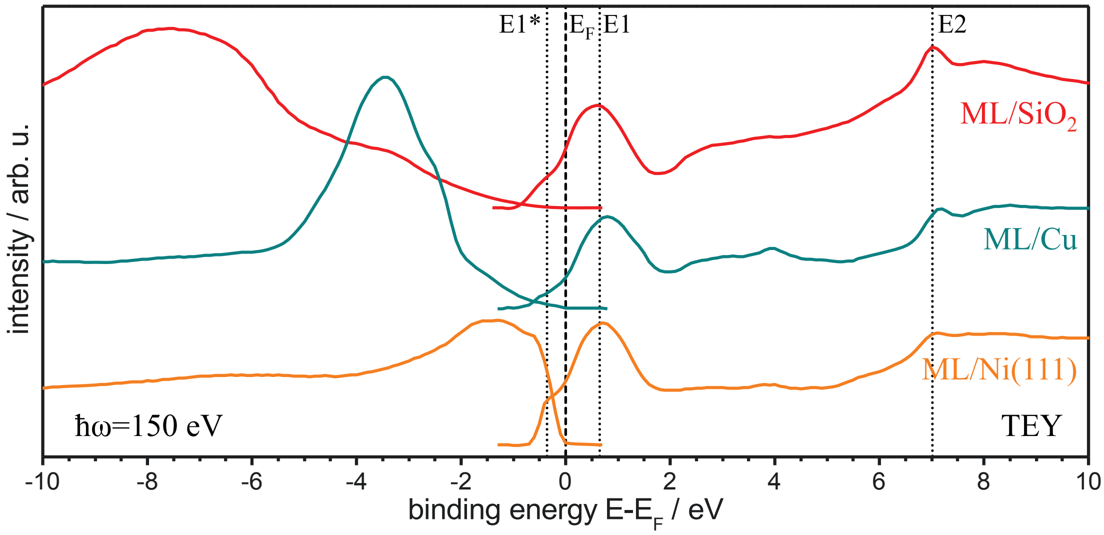

Figure 3.24: *A combined spectrum of the occupied (valence band at 150 eV excitation) and unoccupied states (conduction band, TEY at C1s edge and constant initial state spectrum of the π-band and σ-band) of monolayer Graphene. All spectra are referred to the Fermi energy with the help of the binding energy of the C1s core level (Table 3.5). The excitonic levels are marked with E1* (-0.4 eV), E1 (+0.7 eV) and E2 (+7 eV).*

The excitonic features E1 at +0.7 eV (285.2 eV) and E2 at +7 eV (291.5 eV) separate the unoccupied π*- and σ*-bands from each other.

For ML Graphene on Ni(111) the resonant transition E1* at -0.3 eV (284.2 eV excitation energy) coincides with in the combined VB and CB spectrum with the Ni3d band indicating a hybridization of Ni3d and C2p states. For ML Graphene on Cu and on SiO_2 the hybridization is apparently smaller as the corresponding Cu3d and Si3p states are further apart from the C2p states at the Fermi energy.

In the next section the results of the last material class (Co-PI) are presented which was investigated in this thesis under the aspect of Polarons and excitons at the resonant core level excitation.

3.4 Co-PI

In this chapter the results of the water oxidation TM-oxide catalyst Co-PI are discussed.
For the investigation of the OER catalyst Co-PI four samples where prepared with different deposited charges as listed in Table 3.7. The deposited charge density is used as a measure for layer thickness. In the following these four prepared samples will be referred to as Cat-A, Cat-B, Cat-C, and Cat-D.
Cat-C was only characterized by C2p and O1s core level PES.

Table 3.7: *List of the prepared and investigated Co-PI samples.*

Sample	**Deposited charge / (C/cm^2)**
Cat-A	0.26
Cat-B	0.8
Cat-C	1.05
Cat-D	4.47

3.4.1 CV and AFM

Co-PI is prepared from a Co ion containing electrolyte at pH= 7. The cyclic voltammetry curves of the Co-PI catalysts show a strong anodic wave at 1.1 V vs. Ag/AgCl and cathodic wave at 0.65 – 0.8 V vs. Ag/AgCl (Figure 3.25). These CV-curves are in good agreement with the results and description of Nocera [SUR09].

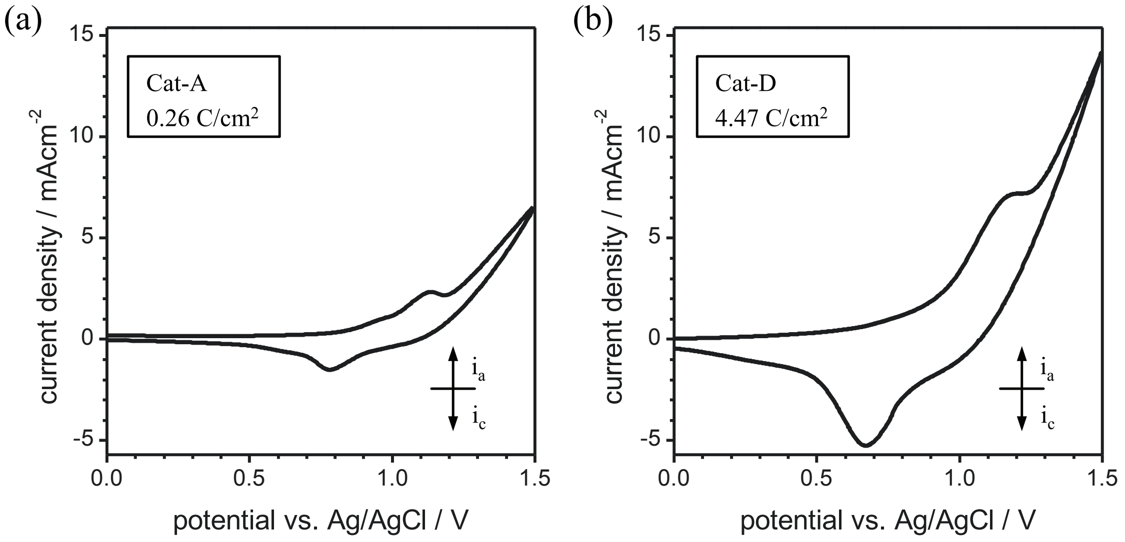

Figure 3.25: *Cyclic voltammogram of Co-PI catalysts in 0.5mM* $Co(NO_3)_2{\cdot}6H_20$ *and 0.1M potassium phosphate electrolyte at pH= 7.0. The CV-curve of Cat-A is shown on the left and the one of Cat-D on the right.*

The surface of the prepared samples was characterized after synchrotron measurements by Atomic force microscopy. An AFM image of the dried Cat-C sample shows a homogeneous film without pinholes (Figure 3.26). The cobalt oxide clusters have diameter of about 1 µm and a layer thickness of about 400 nm.

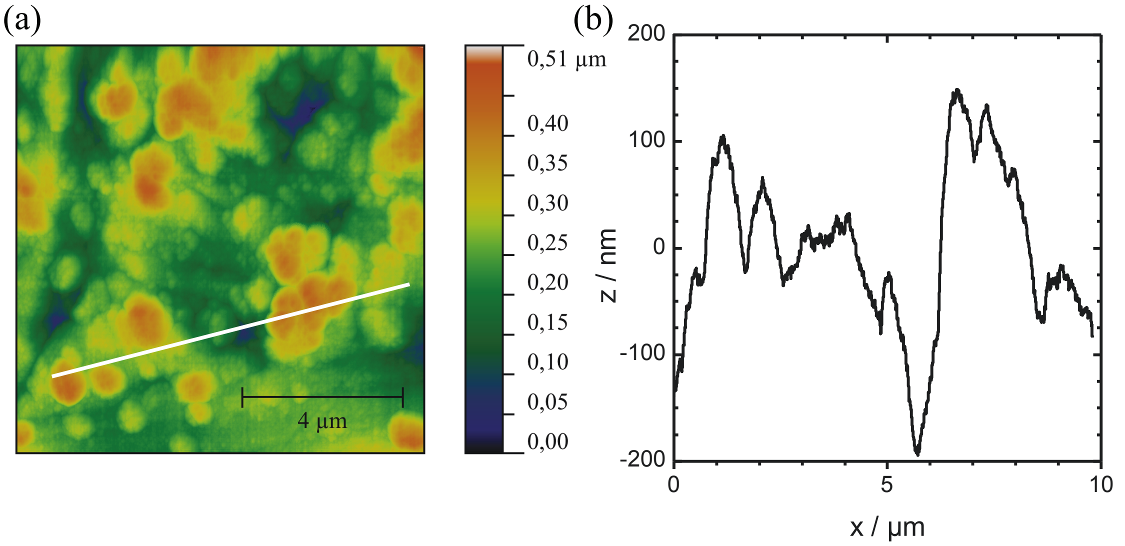

Figure 3.26: *AFM image of Co-PI Cat-C (a). Profile extracted from the AFM image as marked by the white line (b).*

3.4.2 Core levels

For further evaluation of the structural motif, the oxidation state, and as a Fermi energy reference in XAS spectra the core level spectra of Co-PI are depicted in the following.

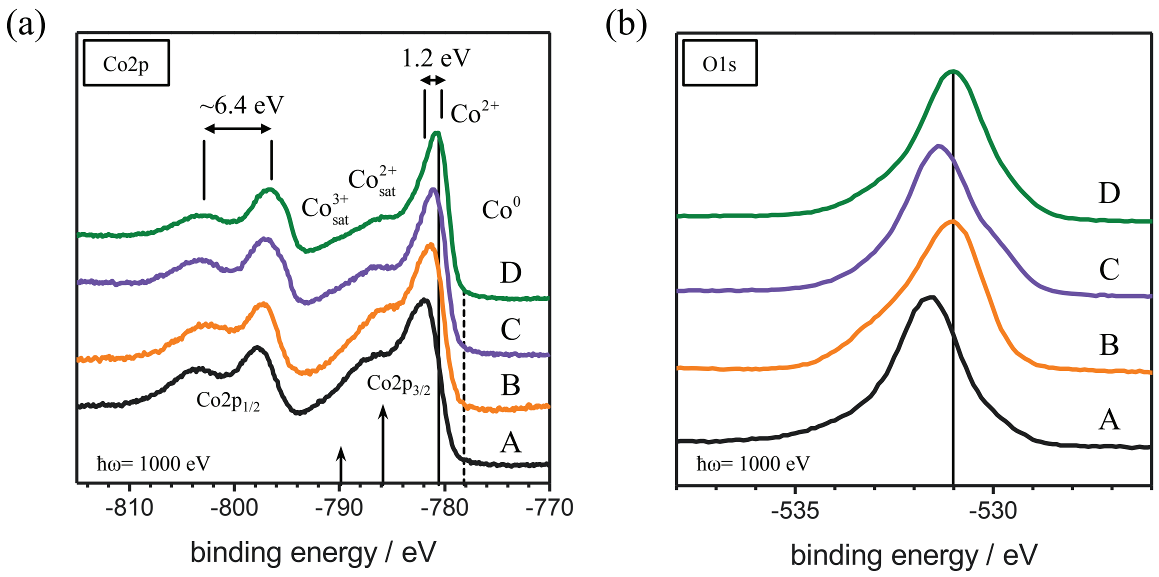

Figure 3.27: *Co2p (a) and O1s (b) core level of the Co-PI Cat-A to Cat-D. The vertical solid line in (a) gives the position of the Co2p$_{3/2}$ Co^{2+} main peak of Cat-D. Here the binding energy is modified by 1.2 eV with the film thickness (Cat-A to Cat-D). The dashed vertical line in (a) indicates the Co2p$_{3/2}$ Co^{0} peak of metallic Co. In addition arrows denote the Co^{2+} and Co^{3+} satellite peaks. The vertical solid line in (b) gives the position of the O1s main peak of Cat-D.*

The deposited Co-PI films were characterized by means of synchrotron radiation X-ray photoelectron spectroscopy with an excitation energy of ħω= 1000 eV (λ= 12.4 Å).

In Figure 3.27a the Co2p core level of the Cat-A to Cat-D are shown. The main emission of the Co2p$_{3/2}$ peak is found at -780.8 eV for Cat-D. It gives rise to two additional satellite structures (marked by arrows in Figure 3.27a) at -785.7 eV (Δ= -4.9 eV) and -790 eV (Δ= -9.2 eV). They are attributed to Co^{2+} and Co^{3+}, respectively [SCH10]. For thicker films the Co^{2+} satellite structure decreases in intensity. The emission of the Co2p$_{1/2}$ line is found at -796.5 eV for Cat-D. Only one satellite structure is found here with a splitting of 6.4 eV.

The main O1s peak, shown in Figure 3.27b, is centred on a binding energy of $E_{B,O1s}$= -531.0 eV for Cat-D and shifted by 0.6 eV compared to Cat-A. There is an increase of the high-energy shoulder at -533 eV for Cat-D (-533.6 eV for Cat-A) for increased Co-PI thickness (Figure 3.27b). Their origin is mainly due to water and hydroxyl adsorption [PET08].

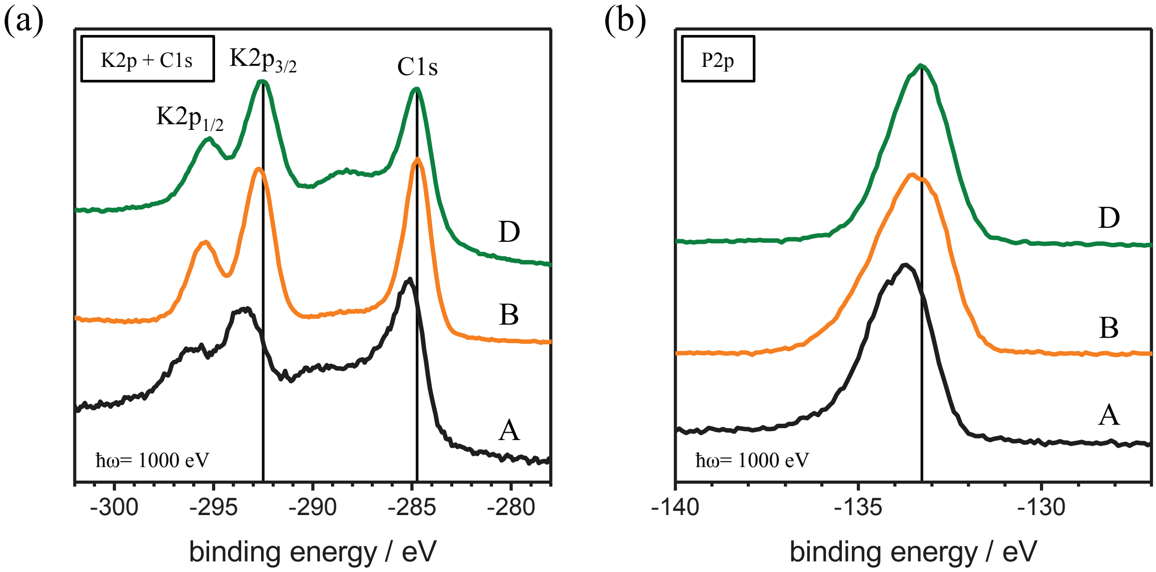

Figure 3.28: *K2p (a), C1s (a) and P2p (b) core level spectra of the Co-PI catalysts Cat-A, Cat-B, and Cat-D. The vertical line indicates the position of the main core level emission line of the thick Co-PI layer (Cat-D).*

In addition the P2p, K2p, and C1s core levels were recorded for catalyst Cat-A, Cat-B, and Cat-D (see Figure 3.28). The corresponding binding energies are $E_{B,P2p}$= -133.3 eV, $E_{B,K2p}$= -292.5 eV (Δ= 2.77 eV), and $E_{B,C1s}$= -284.8 eV for Cat-D. The data obtained for films prepared with a low charge density show higher binding energies, the values are given in Table 3.8.

Table 3.8: *Parameters deduced from PES data analysis of the Co-PI catalyst samples. The binding energy of the core levels and the VBM and CBM are given relative to the position of the Fermi energy E_F. For Cat-C only Co2p and O1s core level data were measured.*

Sample	**Charge density [C/cm^2]**	**Co2p$_{3/2}$ [eV]**	**O1s [eV]**	**P2p [eV]**	**K2p$_{3/2}$ [eV]**	**C1s [eV]**	**VBM [eV]**	**CBM [eV]**
Cat-A	0.26	-782.0	-531.6	-133.7	-293.5	-285.2	-1.8	+2.6
Cat-B	0.80	-781.3	-531.1	-133.4	-292.7	-284.8	-1.5	+2.6
Cat-C	1.05	-781.1	-531.3	-	-	-	-	-
Cat-D	4.47	-780.8	-531.0	-133.3	-292.5	-284.8	-0.8	+2.6

It is possible to deduce the atomic composition of the cobalt catalyst layers by XPS and give a quantitative atomic concentration for each element. That analysis was performed for the Cat-A and Cat-D. The results are given in Table 3.9. For both films the total amount of cobalt and oxygen is about 60 % (Table 3.9). Also, the individual concentration of phosphor, potassium, and carbon is comparable with a relative P:K ratio of 2:1. There is a significant difference, however, as for Cat-D the total cobalt to oxygen concentration is strongly reduced by almost a factor of 3 when compared to the thin catalyst layer of Cat-A.

The increase of the oxygen content and the decrease of the cobalt content are the result of increased water adsorption and incorporation into the thicker layer D. A change in the cluster size also affects the composition. Results from the calculation of the composition for Cat-A and Cat-D are given in Table 3.9 together with results from [YOU10] and results derived from the structural models of [KAN10]. The composition results are also in good agreement with other reported values [YOU10]. Based on the edge sharing cubane and molecular cobaltate cluster models (MCC) a Co concentration of around 20 % is expected with a minimum of 25 % oxygen content [KAN10]. The last 55 % are non-bridging oxygen, hydroxide, phosphate ligands, and water (Table 3.9). Out of Cat-A and Cat-D only the Cat-A with the lowest deposited Co-PI is in this range.

Table 3.9: *Atomic composition of the Co-PI films Cat-A and Cat-D (atomic concentration). For comparison results from Young et al. are included of electrodeposited films [YOU10]. Structural models from Kanan et al. were used for Cubane and MCC bulk/surface concentration calculation [KAN10].*

Sample	**O / %**		**Co / %**	**P / %**	**K / %**	**C / %**
	Lattice/ Bridging	**Ligands**				
Cat-A	34.3	10.3	19.7	8.2	4.3	23.2
Cat-D	22.3	30.7	7.5	9.4	5.7	24.4
Young 5k x	51.5		9.3	5.2	34.0	-
Young 15k x	53.2		14.0	5.8	27.0	-
Cubane surface	24.2	54.6	21.2	-	-	-
Cubane bulk	27.8	50	22.2	-	-	-
MCC surface	38.7	38.7	22.6	-	-	-
MCC bulk	47.6	27	25.4	-	-	-

3.4.3 Valence bands

In order to deduce the pDOS for cobalt and oxygen derived valence band states (Co3d and O2p) resonant excitation was selected at 780.6 eV and 531.0 eV, respectively. The valence band structure at 150 eV can be considered as a non-resonant excitation with the benefit of integrating over all contributions at a rather high cross section. Such data can be understood as giving the total density of states (DOS) in the VB regime and, in addition, is ideal for deriving the position of the VBM with respect to the Fermi energy E_F.

In Figure 3.29 the VB spectra of Cat-A and Cat-D taken at 150 eV and at resonant excitation are shown. The VB spectra consist of Co3d and O2p states.

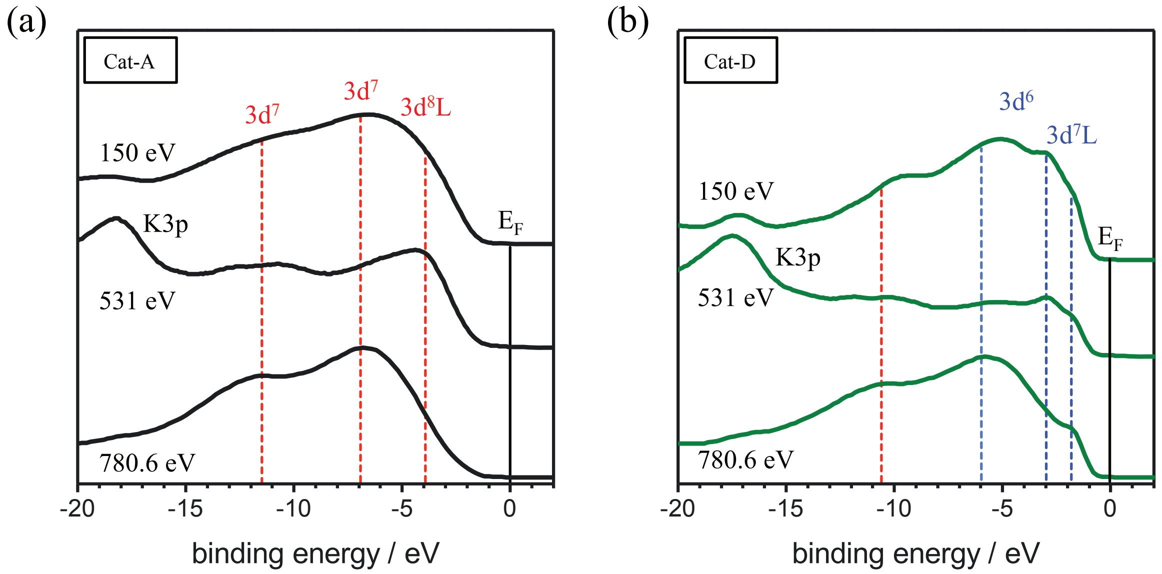

Figure 3.29: *Valence band spectra of Cat-A (a) and Cat-D (b) taken at an excitation energy of 150 eV and at the O1s (531 eV) and Co2p (780.6 eV) resonance of the Co-PI catalysts. The position of the individual Co3d and Co3d charge transfer states (L) are indicated.*

In the Cat-A, Figure 3.29a, a broad band that shows up between 0 eV and -15 eV dominates the VB regime in the 150 eV data. There is a general agreement that this band is predominantly from O2p states (pDOS) [HUE03]. This is in particular true for the thin layers. In the resonant excited spectra of the O1s resonance a pronounced peak is found which must be O2p derived at -4.3 eV. Further oxygen contributions are found at higher binding energies with distinct peaks at -18 eV (overlap with K3p).

The pDOS contributions from Co states (Co3d and Co4s) show up in the VB spectra excited with 780.6 eV. Here rather deep lying contributions peaking at -7 eV and at -11.5 eV are observed.

The data of considerable higher amount of deposited Co-PI Cat-D appear similar, however, there are weak features, which appear at -3 eV and at -1.8 eV. These features are attributed to charge transfer states, which are indicated in the Figure 3.29b. Their appearance is discussed later in Chapter 4.3.3.

The VBM can be deduced from the data taken at 150 eV excitation and is determined to be at -1.8 eV for Cat-A. In the corresponding VB spectra for thicker Co-PI films (Cat-D) the valence band shifts by 1 eV to lower energies. Such a shift of the VBM with respect to E_F is found for all films (Cat-A, Cat-B, and Cat-D). The values are listed in Table 3.8 of the previous section.

3.4.4 Co2p and O1s XAS

The XAS data for the Co-PI Cat-A, Cat-B, and Cat-D at the Co2p and O1s absorption edge are shown in Figure 3.30. In the XAS spectra the position of the Fermi energy is indicated as derived from the binding energy of the O1s and Co2p$_{3/2}$ (L$_3$) core levels, respectively.

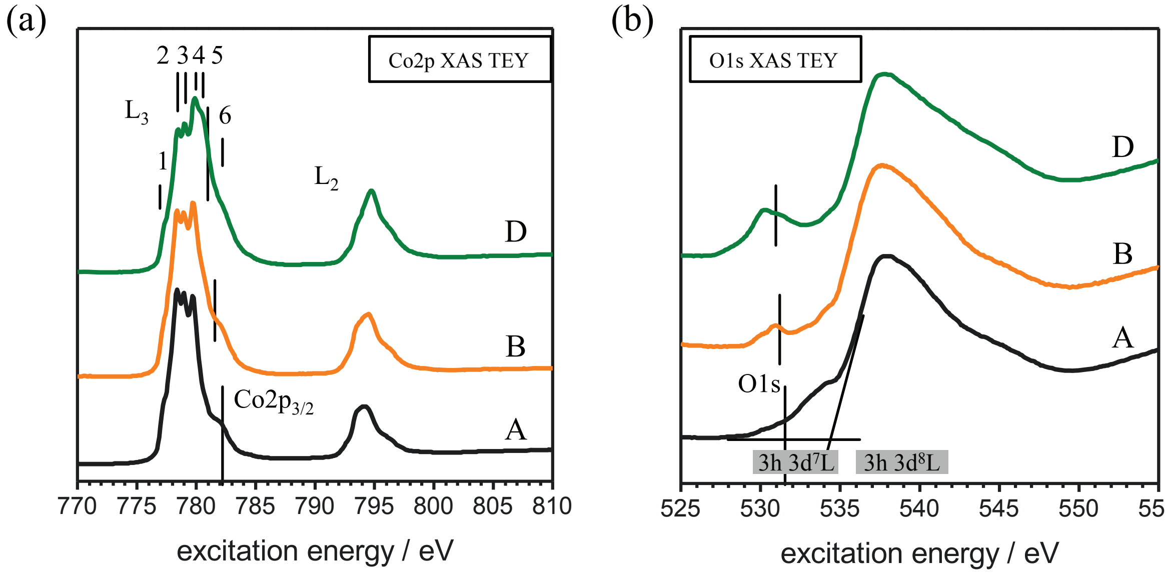

Figure 3.30: *Co2p (a) and O1s (b) XAS spectra of Co-PI catalysts. In the XAS spectra the position of the Fermi energy is given by the binding energy of the O1s, Co2p$_{1/2}$ (L$_2$), and Co2p$_{3/2}$ (L$_3$) core levels.*

In the Co2p XAS spectra the L$_3$ and L$_2$ edges consist of several peaks centred at 779 eV and 795 eV, respectively. At the L$_3$ edge six transitions are found indicated by 1 – 6. They appear at excitation energies of (1) 777.0 eV, (2) 778.4 eV, (3) 779.0 eV, (4) 779.8 eV, (5) 780.6 eV, and (6) 782 eV.

For the O1s XAS spectra the main absorption line is found at 538 eV which extents up to a small pre-edge peak at 531 eV. The pre-edge peak is increased, with larger thickness, but not yet existent in the thinnest Cat-A.

In both XAS spectra the position of the Fermi energy is indicated as derived from the binding energy of the O1s and Co2p$_{3/2}$ (L$_3$) core levels (Table 3.8), respectively.

3.4.5 ResPES diagram at the Co2p and O1s edge

In Figure 3.31 the resPES diagram of the Co-PI catalyst Cat-A and Cat-D are displayed. In both resPES diagrams the Co L_3 edge consists of six main resonances.

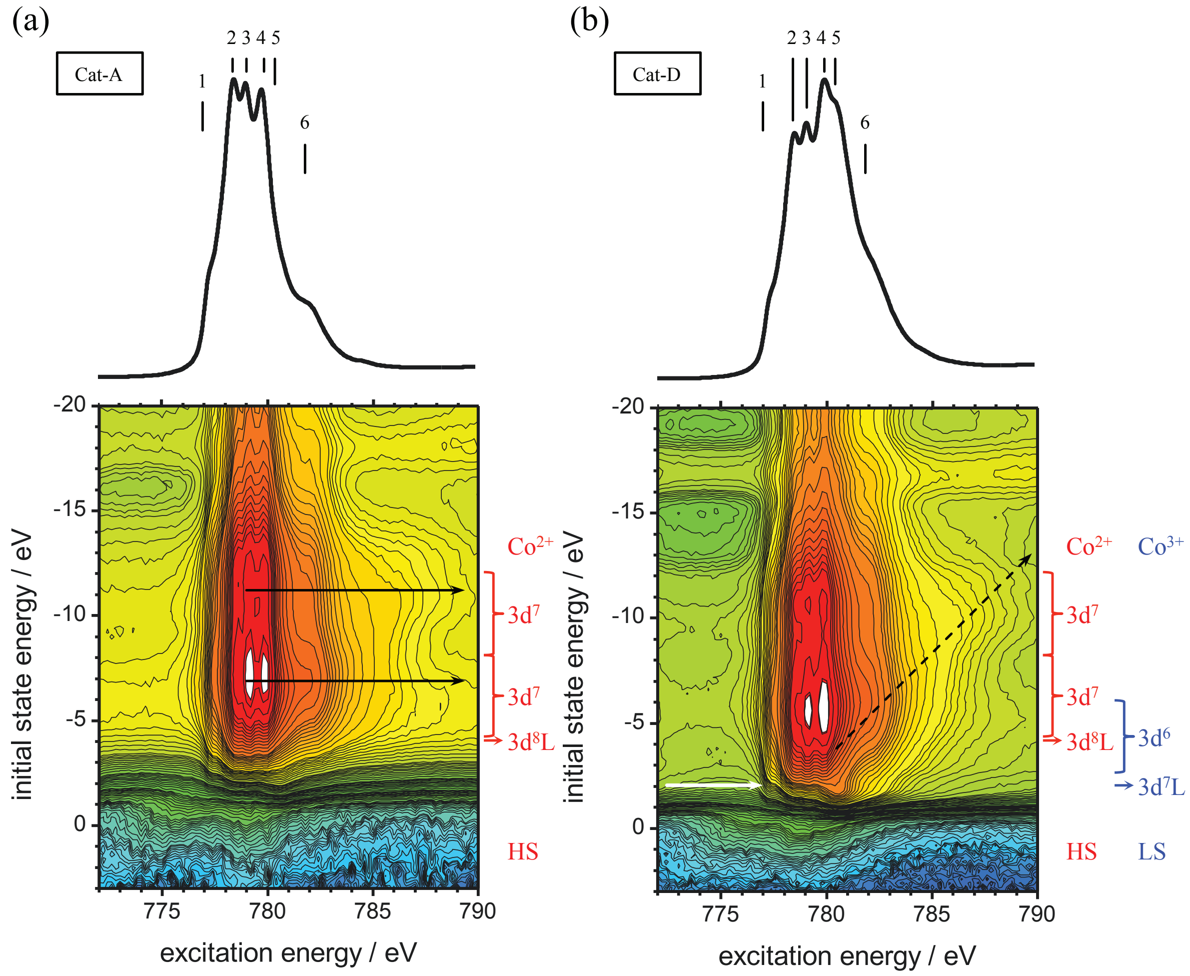

Figure 3.31: *Cobalt 2p L_3 edge resPES diagrams of the Co-PI catalyst for Cat-A (a) and Cat-D (b). The black arrows indicate the participator Auger decay; the dashed line guides the eye towards the spectator Auger decay. The white arrow at -2 eV in panel (b) indicates a valence state with a FANO profile. The top panels of the Figures show the TEY-XAS spectrum of the corresponding catalyst (compare to Figure 3.30a).*

The valence band region can be divided into three regimes. For Cat-A two main bands at -11.5 eV and -7.0 eV initial state energy and a shoulder at lower binding energies at -4.3 eV are found giving rise to participator Auger decays (black arrow; Figure 3.31a). In the corresponding data of Cat-D two new features can be observed (Figure 3.31b). The former band at -7.0 eV is broadened and shifted by 1 eV to lower binding energies. At -1.8 eV a sharp feature arises not present in the thinner layer.

The spectator Co-LMM Auger (2h final state) is propagating under 45° corresponding to its constant kinetic energy (dashed line) of E_{kin}= 775 eV.

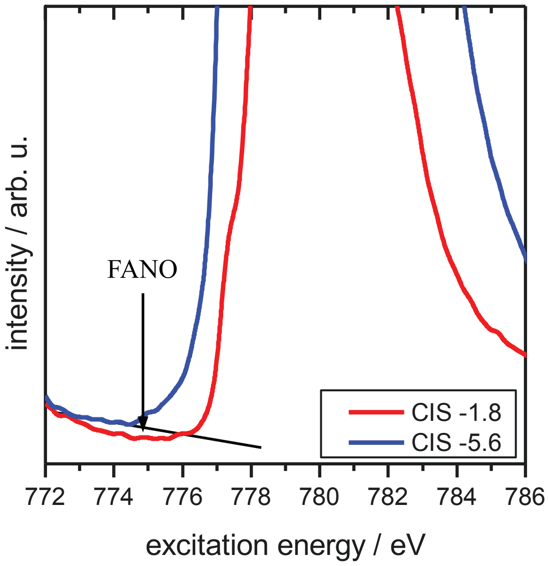

Figure 3.32: *FANO resonance of Co-PI Cat-D at a constant initial state energy of -1.8 eV. For visualisation a CIS spectrum far away from the FANO resonance is included.*

A constant initial state (CIS) cut at the initial state energy of the resonance at -1.8 eV (Co^{3+}) reveals a FANO resonance (Figure 3.32), as it is also observed for the corresponding resonance for previous studies on Cobalt-Oxide at our group [MUE146], [SCH10], [SCHM12].

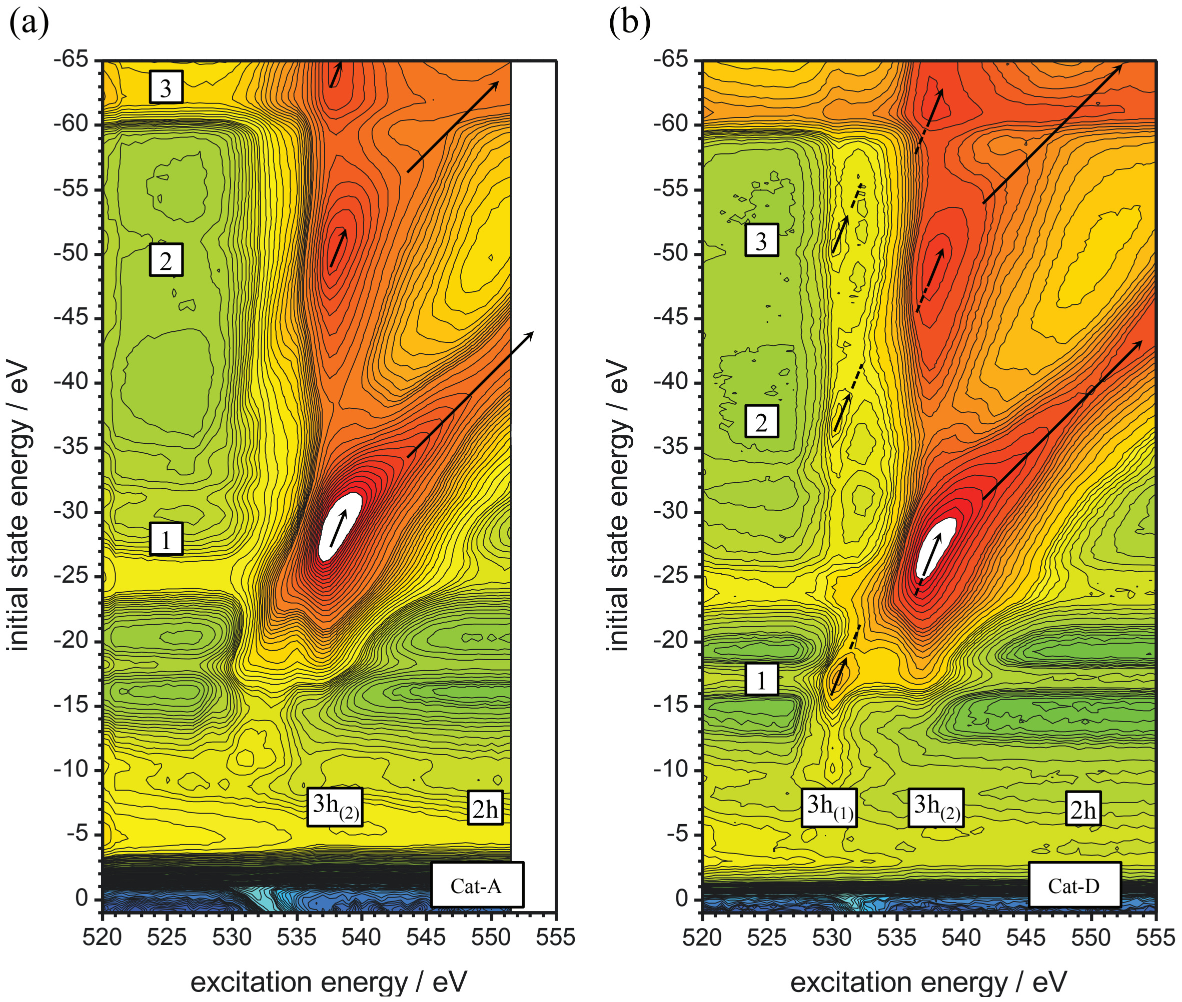

Figure 3.33: *Oxygen 1s edge resPES diagram of the Co-PI catalyst Cat-A (a) and Cat-D (b) at the onset of the KLL-(O1s-O2p-O2p) [1], KLL-(O1s-O2s-O2p) [2], and KLL-(O1s-O2s-O2s) [3] Auger decay.*

The corresponding resPES diagram at the O1s edge of the Cat-A and Cat-D is given in Figure 3.33. In this range of excitation energies the initial states of the VB are found at around -3 eV and of the O2s at around an initial state energy of -24 eV. The weak feature at -17 eV is due to emission from K3p states. Dominating in that resonant profile is the O-KLL Auger (kinetic energy of 510 eV), which has a maximum intensity at around 538 eV.

Three main lines of Auger decays are found (labelled by [1] – [3] in Figure 3.33). They correspond to a O1s-O2p-O2p [1], O1s-O2s-O2p [2], and O1s-O2s-O2s [3] KLL-Auger decay. For the spectator Auger decay (region 2h) a kinetic energy of $E_{kin,1}$= 510 eV, $E_{kin,2}$= 487 eV, and $E_{kin,3}$= <475 eV is obtained.

There are two particular observations in these O1s resPES diagrams. First, there are weaker resonances already at lower excitation energies (region $3h_{(1)}$). In particular, there is a pronounced feature, which appears between 528 eV and 533 eV peaking at around 530 eV ($3h_{(1)}$).

The second observation concerns the slope of the Auger contributions. Only above the resonance energies starting around 540 eV the Auger decay has the expected slope of 45°. Both features around 530 eV ($3h_{(1)}$) and around 537 eV ($3h_{(2)}$) have a different slope with an angle of 67.5°.

The decays of the first two regions ($3h_{(1)}$ and $3h_{(2)}$) differ in their way of propagation from the one above an excitation energy of 540 eV as they have a slope of 67.5° in terms of a $E_{bind}(\hbar\omega)$ diagram instead of 45° for the KLL-Auger decay.

Here, the two 67.5°Auger decays initially appear at a higher kinetic energy (E_{kin}= 514 eV for [1]) at $\hbar\omega$= 530 eV ($3h_{(1)}$); the second one ($3h_{(2)}$) shows up around E_{kin}= 537 eV which is shifted by 3 eV from the first 67.5° Auger band. They approach the value of the normal O-KLL Auger transitions of E_{kin}= 510 eV [1] within a small range of excitation energies.

In the next Chapter the three material classes (organic semiconductors, Graphene, and Co-PI) are discussed on the basis of localized states (Polarons, Excitons, and CT states) and the concept of the multiple hole Auger decay is illustrated.

Chapter 4 Discussion

In this chapter localized states (i.e. Excitons and Polarons) and the novel combined Auger decay processes which are observed first in organic semiconductors, in Graphene systems, and in OER catalyst Co-PI will be discussed in detail.

In the first section the focus is on the organic semiconductors rr-P3HT and PCBM, their characteristic charge carriers (Excitons and Polarons), and the influence of these charge carriers on the resonant Auger decay processes. For both materials a combined spectator-participator Auger (S+P) is found in the π*-band at the threshold of the singlet Exciton. As the rich amount of possible π*- and σ*-transition make detailed discussion on the characteristics of the combined Auger decay difficult HOPG (without van der Waals force) as a more suitable model system is chosen for further investigation about the (S+P) Auger decay and development of a model for the combined Auger decay.

Together with additional new Auger decay combinations observed for Graphene flakes and monolayer Graphene (without van der Waals force) – i.e. a combined double spectator (S+S) Auger and a double spectator (S+S)* Auger-Gain decay – the concept of the combined (S+P) Auger decay will be discussed in the next section. The lifetime of the mandatory excitonic state is covered and a model for each Auger decay combination is proposed.

The last section deals with another class of material (TM-oxide), which also shows indication of combinations of Auger decays at resonance. Here Polarons and Excitons – already known for the organic systems – can also be attributed to this process in oxides as well.

Based on the resPES Auger profile the spin state of the catalyst can be deduced.

4.1 Organic Semiconductors

rr-P3HT as a p-type organic semiconductor is used for organic solar cells as the light absorber and for OFETs as the active layer.

It shows several transition features in the C1s XAS indicating the presence of Excitons (first charge carrier product after light absorption in organic solar cells) and Polarons (dissociation products of Excitons in organic solar cells). Two types of Excitons (singlet and triplet Exciton) and two types of Polarons (interchain 2D-Polarons and intrachain 1D-Polarons) are identified. In rr-P3HT a Fermi level pinning is identified due to a substrate charge transfer. The charge transfer is responsible for doping of rr-P3HT. CT doping of rr-P3HT proceeds solely via 2D-Polarons as identified by a 2D-Polaron doping gradient.

In contrast, PCBM as the electron acceptor material in organic solar cells only shows indication of one singlet Exciton.

For both materials, rr-P3HT and PCBM, the singlet Exciton give rise to a combined spectator-participator (S+P) Auger process at the C1s resonance. The concept of the (S+P) Auger decay will be discussed later on in Chapter 4.2.2.1.

4.1.1 Charge Carriers in P3HT

In the rr-P3HT XAS spectra three localized features could be identified in Figure 3.5b which are the E_S, the E_T and the σ* Exciton. E_S is the singlet Exciton below the CBM with a binding energy of E_{bind}= 0.4 eV. At E_S the (S+P) Auger decay process starts (Figure 3.4).

In contrast, the absorption resonance E_T does not decay via an S or (S+P) Auger decay, as it is the case for the other two resonances (E_S, σ*). For an Auger decay the participating electrons need an overlap in their wave function in order to transfer the energy after refilling the core level. This is not fulfilled for E_T. It can be concluded that this level is strongly localized (has a long lifetime, see Chapter 4.2.1) with no overlap to the other VB states.

The energy difference of E_T relative to the VBM and CBM is 1.4 eV and 2.2 eV respectively (Figure 3.7). These values are in good agreement with values reported for triplet Excitons, also confirmed by the strong localization of this level in the resPES measurements in Figure 3.5b [KOE09], [OHK08], [OST03].

A formation of triplet Excitons is possible by intersystem crossing (spin-flip) or singlet Exciton fission. The efficiencies for spin-flip or fission is strongly correlated to the energetic difference between the optical singlet Exciton and the lowest triplet Exciton, with low rates for higher differences [ARY12]. A calculation of the energetic values for singlet E_S and triplet E_T states give E_S= 2.69 eV and E_T= 1.46 eV for poly(paraphenylenevinylene) (PPV) [ARY12]. The value of E_T of 1.4 eV of this work is in good agreement. Also, Gou et. al estimated an energy level of 1.55 eV for the lowest triplet state and 2.0 eV for the singlet Exciton in rr-P3HT [GUO09]. Triplet Excitons show longer lifetimes and stronger spin interaction than their singlet counterparts [SHA05] (see also Chapter 4.2.1).

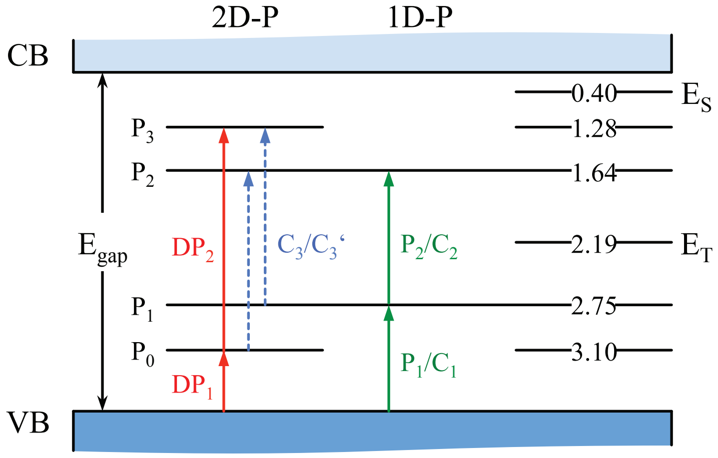

Figure 4.1: *The diagram combines the energy values (eV) referred to the CBM (binding energies) evaluated from the XAS data of the polaronic levels P_0 - P_3 (this work) and excitonic levels E_S and E_T (this work) with the optical transitions for 2D-Polarons (DP_1, DP_2, C_3) and 1D-Polarons (P_1, P_2, C_1, C_2) for rr-P3HT from [BEL01], [OST00], [OST01].*

In addition to the two excitonic levels E_S and E_T four polaronic levels P_0 - P_3 are identified. The energy values of the polaronic (P_0 - P_3) and excitonic levels (E_S and E_T) relative to the CBM at 287.6 eV are included in Figure 4.1 {energy positions taken from Table 3.2 (this work)}. The corresponding optical transitions for Polarons are indicated in addition and are in excellent agreement with the literature [BEL01], [OST00], [OST01]. They are also given in Table 4.1. Both, the energy values and the number of transitions confirm the assignment in terms of 2D-Polarons.

The assignment of the transitions E_S and E_T to Excitons and P_0 - P_3 to Polarons is in addition emphasized by measurements of the elastic photon scattering channel on rr-P3HT by

RIXS (Figure 3.8). All six transitions are evident in the elastic channel indicating their localized nature as scattering centres in RIXS (see Figure 3.8b).

From the combined VB and XAS spectrum the binding energy of the Excitons and the band gap of rr-P3HT was obtained (see Figure 3.7). The binding energy of the π*-CB Exciton (E_S) is in the order of 0.4±0.1 eV in agreement with the literature [ARY12], [HOR02]. For E_T a value of 2.19 eV for the binding energy is obtained. Taking the FWHM of the E_S peak into account (1.9 eV) the resulting electronic band gap $\{\Delta(E_S\text{-VBM})\}$ of 2.4±0.2 eV is close to the optical band gap (2.0±0.1 eV) obtained from the UV-Vis measurements (Figure 3.1).
These band gap values are also in agreement with the literature (E_{gap}= 2.6 eV deduced from combined inverse photoemission spectroscopy and UPS spectra; E_{gap}= 1.86 eV deduced from UV-Vis measurements) [DEI10].

Table 4.1: *Comparison of the Polaron transition energies from photo-induced absorption spectroscopy [OST00], [OST01] and charge modulated spectroscopy [BEL01] measurements to the XAS findings (this work). All values are referred to the VBM.*

Transition	**Österbacka et al. [OST00], [OST01]**	**Beljone et al. [BEL01]**	**This work**
DP_1	0.06/0.07	-	>0.1
DP_2	1.7/1.8	-	1.82
P_1/C_1	0.37	0.35-0.45	>0.45
P_2/C_2	1.3	1.25	1.11
C_3/C_3'	-	1.65/1.35	1.46
2Δ/CT	0.3-0.4	0.1-0.4	0.35

4.1.1.1 2D-Polaron in P3HT

In the previous section the existence of Excitons and 2D-Polarons in the XAS spectrum of rr-P3HT was verified.

Especially, the appearance of the split absorption band in the C1s XAS of rr-P3HT gives evidence for the existence of 2D-Polarons (see Figure 3.6). By the decomposition of the rr-P3HT XAS spectra into Gaussians a quantitative analysis of the polaronic and excitonic states is enabled. The doping concentration of rr-P3HT can be calculated from the intensity fraction of (P_0+P_1) relative to the intensity of the main line at 287.6 eV. The area of the Gaussians gives the intensity of the states. From the analysis the following intensities are extracted for the TFY (TEY) spectrum:

- A_{P0}= 0.14 (0.09); FWHM$_{P0}$= 0.4 (0.4) eV;
- A_{P1}= 0.17 (0.14); FWHM$_{P1}$= 0.4 (0.4) eV;
- A_{CBM}= 1.92 (2.00); FWHM$_{CBM}$= 1.7 (1.3) eV.

Further the relative amount of the 2D-Polarons is determined by the relative intensities of P_0 and P_1 to the CBM. The relative doping concentration can now be calculated from these three values and is given as:

- $doping_{total} = \frac{A_{PO} + A_{P1}}{A_{CBM}}$;
- $doping_{2D} = doping_{total} \cdot \frac{A_{P0}}{A_{P1}}$;
- $doping_{1D} = doping_{total} \cdot \left(1 - \frac{A_{P0}}{A_{P1}}\right)$.

For the 100 nm sample at the interface (TFY) the doping concentration amounts to [total= 16 %; 2D= 13 %; 1D= 3 %]. In contrast, the concentration of 2D-Polarons is reduced when surface sensitive data (TEY, 100 nm) are analysed [11 %; 7 %; 4 %] (see Figure 3.6b). The error within the determination for 1D- and 2D-Polaron doping concentration is about 2 %. In Table 4.2 the relative doping concentration is given for both samples of Figure 3.6b.

Table 4.2: *Polaron (Doping) concentration of rr-P3HT of samples with two different thicknesses.*

Sample	**Total Polaron concentration**	**2D-Polaron concentration**	**1D-Polaron concentration**
100nm TFY	16 %	13 %	3 %
170nm TFY	12 %	9 %	3 %
100nm TEY	11 %	7 %	4 %
170nm TEY	9 %	5 %	4 %

S2p core level spectra of rr-P3HT likewise indicate an oxidized species (doping of rr-P3HT). From the S2p spectrum a doping concentration of 2 % per thiophene unit is obtained (Table 3.1). This is in the order of the 1D-Polaron doping concentration (see Table 4.2) and could be due to small quantities of oxygen which are under the detection limit of SR-PES as neither O1s core level nor O-Auger decays are observed (see Figure 3.2). However, this does not explain the high doping concentration of 2D-Polarons.

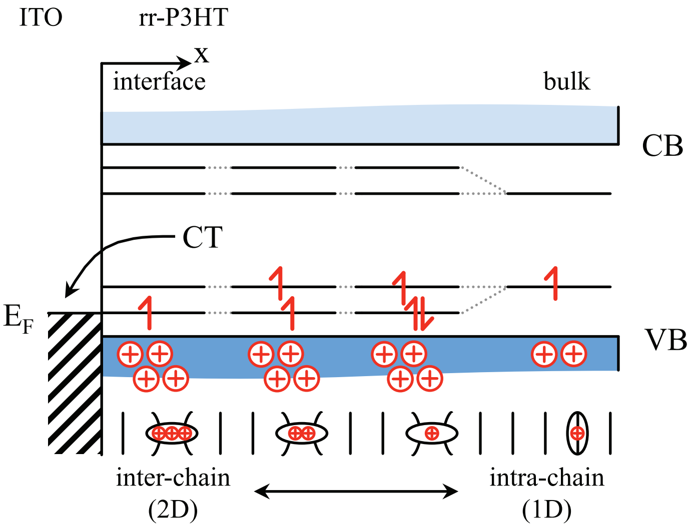

Figure 4.2: *2D-Polaron Fermi level pinning at the organic–inorganic interface of rr-P3HT on ITO by charge transfer with the corresponding charge distribution and the transition from 1D-Polarons to 2D-Polarons.*

The intensity of the 2D-Polaron features is increasing with the information depth (distance to the substrate interface i.e. the rr-P3HT layer thickness). This is shown for two different samples (100nm and 170nm thickness) in Figure 3.6b. The intensity of the 2D-Polarons increases from 5 % (TEY, 170 nm sample) to 13 % (TFY, 100 nm sample) (see Figure 3.6, Figure 4.2, and Table 4.2).

The highest 2D-Polaron concentration is thus found in the TFY spectrum of the 100 nm sample (Table 4.2) where rr-P3HT closest to the substrate interface is sampled. Hence, the doping of rr-P3HT should be substrate induced and arise from an interface charge transfer.

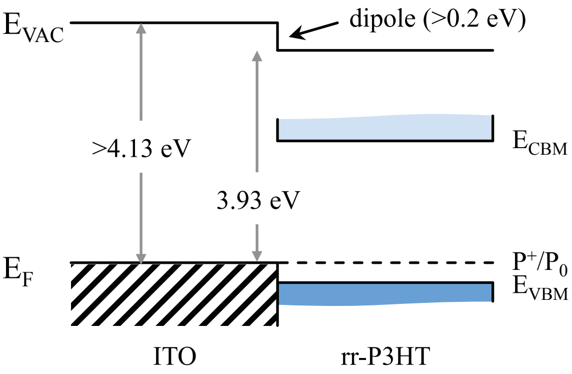

Figure 4.3: *Schematic band line-up at the interface of rr-P3HT on ITO. The Fermi level is pinned to the positive Polaron charge transfer state (P_0). The values are taken from Figure 3.7.*

The driving force for an interface charge transfer and doping of rr-P3HT is the energy difference between the work function of the ITO substrate (Φ_{ITO}= >4.13 eV, Figure 3.7) and the P_0 level, which is the positive charge transfer (P^+) state in rr-P3HT (3.9 eV) [XU09]. The work function of rr-P3HT on ITO was determined to be $\Phi_{rr\text{-}P3HT}$= 3.93 eV (Figure 3.7). Electrons flow from P3HT to the substrate until the positive charge transfer state and the Fermi level of the substrate is equalized, i.e. the Fermi level is pinned to P_0/P^+. A dipole of >0.2 eV at the interface is a consequence of the pinning (see Figure 4.2 and Figure 4.3). The CT of electrons from rr-P3HT to the substrate therefore can be treated as a substrate oxidation of the polymer and is responsible for the high concentration of 2D-Polarons.

The constant doping concentration of 1D-Polarons (see Table 4.2) on the other hand is probable due to residual oxygen.

From the data it can be clearly stated that the number (3 % – 4 %) of 1D-Polarons remains unaffected by the charge transfer and is independent on the distance to the interface (see Table 4.2). Consequently, it can be deduced that the charge transfer proceeds exclusively via 2D-Polarons causing a pinning at the polaronic energy levels. However, the interface charge transfer could either create new 2D-Polarons or change the occupation number of the existing 2D-Polarons (see Figure 4.2).

2D-Polarons can carry a single charge (+) up to three charges (+++) (see Figure 4.2). Here it cannot be differentiated between the charge states of (+), (++), and (+++) of 2D-Polarons.

In summary, in the carbon K-edge XAS spectra of rr-P3HT four additional features are identified alongside the excitonic transition E_S and E_T.

These four transitions can be attributed to arise from Polarons. Especially, their characteristic energy level splitting identifies these features to arise from 2D-Polarons in excellent agreement to optical measurements and theoretical studies [BEL01], [OST00], [OST01]. In addition, a doping gradient of these 2D-Polarons was identified. Their number increases through charge transfer from the interface inducing a Fermi level pinning in rr-P3HT at the positive charge transfer state P^+ of rr-P3HT. The CT at the interface proceeds solely via 2D-Polarons. Next to the interface the intensities indicate 13 % of 2D-Polarons at a total Polaron density of approximately 16 %.

Out of the two excitonic states only the singlet exciton E_S 0.4 eV below the CBM shows an influence on the Auger decay in π*-band of rr-P3HT. Here the Auger decay proceeds via a combined (S+P) Auger decay. The concept of this new resonant Auger decay will be discussed in Chapter 4.2.2.1.

4.1.2 Valence and conduction band states in PCBM

PCBM as an electron acceptor material is added in organic solar cells to increase the dissociation rate of singlet Excitons by increased Exciton dissociation rate at the interface of PCBM to the light absorbing material, for instance rr-P3HT [SAR92], [ZHU11]. Its light absorbing properties are rather weak in the visible light range compared to rr-P3HT (compare Figure 3.9b and Figure 3.1b). Thus only Excitons are expected to exist in a high concentration (e.g. charge transfer Excitons at the interface to rr-P3HT – the electron is transferred to PCBM whereas the hole stays in rr-P3HT).

The resPES diagram of PCBM is rich on transitions to different π*- and σ*-bands. Their nature is investigated in the following by resonant photoemission (Figure 3.12a). Only the intensity of the first three valence orbitals π_1, π_2, and π_3 (almost pure π-character) is resonantly increased for direct excitation into the π*-band systems. Higher valence band states – with σ-character – can also be excited into higher π*-band states and even into the σ*-band system for pure σ character of the VB state. This is evident from the profile of the corresponding VB spectra ($\pi^*_{2,3}$, π^*_4, σ^*_5), which excepting the Auger contribution do not differ in shape and intensity and are different to the VB spectra of π^*_1 and π^*_{phenyl}. Their shape is exemplary shown for the VB at the π*4 resonance in Figure 3.12a.

Under resonant excitation from the first π-band states (π_1) electrons can only be excited into the first π*-band (π^*_1). This is evident from only one sharp peak in the corresponding CIS spectra (CIS π_1, Figure 3.12b). It has a low FWHM of 450 meV, which can be correlated to a long lifetime.

Excitons have typically lifetimes in the range of 10^{-9} to 10^{-6} s [SHA05]. It is also known that the C1s→π* and C1s→σ* transitions at their threshold energies have high excitonic contributions [BRU95], [PET98]. The first resonant excitation can therefore be attributed to arise from the direct C1s (π)-π* excitation, which leads to the formation of the π* Exciton (singlet Exciton).

For the direct excitation from higher valence band states (π_3, $\pi/\sigma_{4,5}$, π/σ_6), the formation of an Exciton (π^*_1) is also apparent but direct excitation into the higher π*-band states is as well possible ($\pi^*_{2,3}$, π^*_4). This is due to the fact that higher states posses also admixture with σ-character.

For VB states of pure σ-character (σ_7) the excitation proceeds into an additional level (σ^*_5). Above this energy also excitations into the σ*-system are possible.

States originating from the phenyl side group are exceptions of this rule. They can only be excited into the excitonic state or into their own π*-orbitals (285.0 eV, π^*_{phenyl}), but not into the π*-system of the fullerene.

It has to be noted that the CIS of π_3 shows excitation not only into π^*_1. This is an indication that π_3 has also σ-character to some extend, not apparent only by VB-spectra.

The shoulder in higher CIS spectra at 285.3 eV is not due to excitation from the C_{60} π-system into the π*-system of the side group, as the intensity is expected to be much higher. Rather C_{60} also has some states in this energy region.

Therefore the peaks in the range of 285 eV – 291 eV excitation energy can be assigned to arise from C1s/VB-π* transitions. Above 291 eV the bands consist solely of σ*-character.

Both π* and σ* states can also be distinguished in the resPES measurements by the difference in the Auger decay (Figure 3.11). The kinetic energy of the initial spectator Auger decay of E_{kin}= 267 eV for the core electron excitation into π* states (starting with π^*_1 at 284.5 eV) is decreased by 3 eV to E_{kin}= 263 eV for the core electron excitation into σ* states (starting with σ^*_5 at 290.8 eV). This shifted spectator Auger decay gives evidence that also in PCBM as well as in rr-P3HT the singlet Exciton give rise to a combined spectator-participator Auger decay (see Chapter 4.2.2.1). The C1s core hole is refilled by an (S+P) Auger decay only as long as the initial excitation happens into π* states (until π^*_4).

Hence, in order to obtain the electronic band gap not the difference of π_1-π^*_1 has to be calculated, as this value is equivalent to the Exciton energy with a value of 1.4 eV, but the difference to the next XAS feature π^*_p has to be given which is 2.0 eV. The binding energy of the Exciton in PCBM is about 0.6 eV similar to the value obtained for rr-P3HT of about 0.4 eV.

In summary, PCBM shows a strong first excitonic resonance. No Polarons are evident for PCBM. The singlet Exciton with a binding energy of 0.6 eV and a low FWHM of 450 meV (equivalent to a lifetime of 1.5 fs) give rise to a combined (S+P) Auger decay. The core hole only decays via the (S+P) Auger process until excitations from C1s directly into σ* states are possible.

4.1.3 Conclusion - organic semiconductors

In summary, both organic semiconductors rr-P3HT and PCBM exhibit strong excitonic resonances below the CBM. The singlet excitonic binding energy is about 0.4 eV for rr-P3HT and 0.6 eV for PCBM, respectively. It is found to give rise to a combined spectator-participator Auger decay (S+P) only for transitions into the π*-band, for both rr-P3HT and PCBM.

Excitation into triplet Exciton or Polaron in-gap states, found only for rr-P3HT, do not induce an Auger decay. They act as strongly localized scattering centres as evident from elastic scattering channel of RIXS. In rr-P3HT the Fermi level is pinned to the lowest polaronic level (P_0) by a substrate induced charge transfer. The Polarons in rr-P3HT are identified to be 2D-Polarons because of their characteristic level splitting in agreement with optical measurements [BEL01], [OST00], [OST01].

Singlet Excitons do not only give rise to a combined (S+P) Auger decay as observed for rr-P3HT and PCBM. For Graphene systems also additional combinations are possible as evident by the ±78.75° slope for Graphene flakes (see Figure 3.21).

For rr-P3HT and especially PCBM the rich amount of transitions to different π*- and σ*-bands make a detailed discussion of the basics of the (S+P) Auger decay rather problematic.

Therefore, in order to study the concepts of the (S+P) Auger decay in more detail HOPG as an ideal candidate is chosen as it's XAS is not superimposed by several strong π*- and σ*-resonances. HOPG only shows a strong first π* and a second σ* resonance.

Its van der Waals force bound layers (Figure 1.7a) show similar influence on the Auger decay as the crystalline lamellae structure (π-π stacking) of rr-P3HT (Figure 1.3). The Auger decay starts right at the C1s threshold. Therefore HOPG (with van der Waals force) and Graphene systems (without van der Waals force) are ideal candidates to study the fundamentals of the combined Auger decay processes.

Thus, in the next chapter, the fundamentals of the combined (S+P) Auger decay will be discussed on the basis of HOPG and the additional combinations {(S+S) and (S+S)*} on the basis of Graphene flakes and monolayer Graphene.

4.2 Multiple hole Auger decay

Singlet Excitons are found to give rise to a novel combined spectator-participator Auger decay (S+P) in the π*-band of sp^2 hybridized systems. This chapter will not only cover the concepts of (S+P) Auger decay found in rr-P3HT and PCBM at the threshold of the singlet Exciton in the π*-band but also the concepts of additional combinations of Auger processes that are found at the Exciton threshold in Graphene flakes (double spectator (S+S) Auger and double spectator (S+S)* Auger-Gain decay).

Instead of rr-P3HT and PCBM as a basis for further discussion of the (S+P) Auger decay HOPG was chosen due to the clear separation between π* and σ* resonance (E1 and E2) in HOPG which are undisturbed by additional transitions.

At the resonant excitation at the carbon C1s edge of these sp^2 hybridized systems (rr-P3HT, PCBM, HOPG, and Graphene) multiple hole Auger decay processes are observed. They are attributed to the existence of localized states above E_F (singlet Excitons for rr-P3HT and

PCBM). The multiple Auger decay processes are found to be very sensitive for the lifetime of the photo-excited state, which is influenced by polarization of VB and CB states or by the existence of localized (in-gap) states above E_F. In the Kramers-Heisenberg scenario, the FWHM of the resonance can be attributed to the lifetime of the respective photo-excited intermediate state.

Interlayer interaction (van der Waals force for HOPG and π-π stacking for rr-P3HT), substrate interaction, substrate screening, charge redistribution, and in-gap states are reflected in this lifetime. Also, a different lifetime is observed for the individual trapping levels (Exciton, Polaron).

As the photo-excited electron has a chance to probe the various intermediate states the observation of these individual Auger processes allows to conclude for instance on the quality of Graphene in terms of the magnitude of perturbation of the π-cloud by localization effects and trapped localized states.

Different Auger decay channels {1h (P), 2h (S), 3h (S+P), +4h (S+S), and -4h(S+S)*, see Figure 3.17, Figure 3.21, and Figure 3.23} can be identified by their individual slope in the E_{bind}(hω) diagram as a consequence of the different individual lifetime of the photo-excited intermediate state (Table 4.3). In particular, at resonant excitation at the C1s edge there is a high probability to find a combination of new Auger decays due to the high density of excited states.

The Auger angle α in the resPES data is defined by the slope in a E_{bind}(ħω) diagram. Here the following relation can describe the characteristic feature of this resonant mechanism.

$$\pm\Delta = \pm\frac{\Delta_{initial}}{\Delta_{exc.}} = \tan(\pm\alpha) = \cot\left(\pm\frac{\pi}{2^n}\right) \tag{24}$$

The number n of holes in the final state in this relation also describes the slope of the participator (1h) and spectator (2h) Auger decay. n= 2 gives the regular spectator process with α= 45°. n= 1 in the participator decay with α= 0°.

The case for n= 3 (α= 67.5°) is explained in the following (Chapter 4.2.2.1) by the concept of the combined spectator-participator (S+P) Auger decay process, which can be found in sp^2 hybridized systems only in the π*-region at the Exciton threshold. The interlayer coupling (van der Waals force) for instance on HOPG give rise to an (S+P) Auger decay with a 3h final state at the π*-resonance (see Figure 3.17).

The case of n= ±4 (α= ±78.75°) is found for Graphene flakes and will be covered in Chapter 4.2.2.2 and 4.2.2.3.

For the Graphene flakes (Figure 3.21) two decay processes next to the π*-resonance at 285 eV are found. The slope of the decay below the resonance energy is inversed to that above (α_{+4h}= +78.75° and α_{-4h}= -78.75°) which results in a V-like shape profile. For the first process the kinetic energy of the Auger decay is increased with increased excitation energy. This Auger-Gain process gives the slope of -78.75°. On the other hand the +78.75° slope corresponds to a conventional Auger decay mechanism. Both processes are indicative for a four hole final state and can be attributed to combinational (S+S) and (S+S)* processes, respectively.

Table 4.3: *Multiple Auger decay combinations; their final state and angle in resonant photoemission. S denotes to the spectator and P to the participator Auger decay with the asterisk indicating additional kinetic energy of the Auger decay gained by the decay of an Exciton.*

Combination	**Holes in Final state**	**Angle of inclination α**
P	+1h	0°
S	+2h	+45°
(S+P)	+3h	+67.5°
(S+S)	+4h	+78.75°
(S+S)*	-4h	-78.75°

Each individual multiple hole Auger decay is affected by the lifetime of Excitons. The presence of an excitonic state in HOPG and Graphene flakes is indicated by a FANO resonance (see Chapter 4.2.2). In addition, the strong excitonic nature of the first resonance feature E1 at 285.5 eV in HOPG is indicated by the low FWHM in the XAS data with $E1_{FWHM}$= 1.0 eV and its high intensity (up to 2x) compared to Graphene flakes, few-layer Graphene, and monolayer Graphene Figure 3.15). Most of the intensity is found in the π*-resonance (E1) which indicates a very long lifetime of the excited state (0.7 fs). A long lifetime of the excited state also promotes the decay into many elemental low energy channels (e.g. plasmons) and scattering at defects. The normal photoemission is strongly suppressed. Only very weak valence band features are apparent above the C1s threshold and only strong spectator Auger decay contributions are visible (see Figure 3.17 and Figure 3.18). Based on the lifetime of E1 (0.7 fs), its high intensity, its strong spectator Auger decay contributions, its suppression of normal photoemission channels, and the appearance of a FANO resonance (see Figure 3.17) the main feature at 285.5 eV is assigned to arise from a localized excitonic state due to carbon layer interaction in addition to its C1s-π* character for HOPG. Also for Graphene flakes the first C1s-π* transitions can be attributed to have a strong excitonic component due to the appearance of a FANO resonance (see Figure 3.21) and long lifetime (0.6 fs, see next section).

In the next section the lifetime of the excitonic and polaronic in-gaps states for rr-P3HT, PCBM, HOPG, Graphene flakes, and monolayer Graphene is discussed.
After this the concept of each individual combination of the Auger decay processes will be discussed separately {(S+P), (S+S), and (S+S)*} and a model for each of the combinations will be proposed. A summary is given in the end.

4.2.1 Lifetimes

The lifetime of the core level excitation into an intermediate state in XAS is indirect proportional to the FWHM of the transition and can be calculated by the following equation (uncertainty principle):

$$\tau = \frac{\hbar}{\Gamma} = \frac{6.58211928 \cdot 10^{-16}\,\mathrm{eV \cdot s}}{\mathrm{FWHM}} \tag{25}$$

Intermediate states are not only transitions to π*- and σ*-bands but also transitions to excitonic and polaronic in-gap states.
In Table 4.4 the Exciton and Polaron lifetimes are given which are extracted from the individual XAS spectra (Figure 3.5b, Figure 3.12b, and Figure 3.15). For comparison the values for P3HT and PCBM are included in this table. In general the lifetime of Polarons and Excitons of the organic semiconductors in this work (P3HT and PCBM) are higher than for the Excitons found in HOPG and Graphene (excepts for the singlet Exciton in P3HT). The highest lifetime is obtained for the Exciton in PCBM, but the lowest for the singlet Exciton E_S in P3HT. The latter is probably due to the fact that most of the singlet Excitons get converted to triplet Excitons in their decay process.

Remarkable is the relative high lifetime of the pre-edge resonance in ML Graphene. This is an effect of the substrate interaction and hybridization (Chapter 4.2.2.4).

A combined Auger decay is only found for the singlet Exciton in rr-P3HT (E_S), PCBM (π^*_1), and Graphene flakes (E1). For rr-P3HT and PCBM their binding energy is 0.4 eV and 0.6 eV, respectively. For HOPG and Graphene it is expected to be in the same order. Optical absorption measurements indicate a binding energy of about 0.42 eV for monolayer Graphene [CHA11]. The FWHM of the singlet Exciton is in the same order as the one of their binding energy. Hence, the singlet Excitons have a significant overlap with the CB.

Triplet Excitons and 2D-Polarons found in rr-P3HT and the Polaron found in HOPG have negligible overlap with the CB, as their binding energy is too high compared to their FWHM. For instance for rr-P3HT the binding energy of the triplet Exciton is 2.2 eV and the FWHM is 0.4 eV (compare Figure 4.1).

Hence, only singlet Excitons can contribute as localized in-gap states to a combined Auger decay. The lifetime of the singlet Exciton is reduced by about 10 % for Graphene compared to Graphene flakes. For HOPG interlayer Excitons can be formed compared to only intralayer Excitons for Graphene. An (S+P) Auger decay is only found in HOPG (in addition to P3HT and PCBM) whereas (S+S) and (S+S)* Auger decays are only found for Graphene.

On the other hand for monolayer Graphene on Ni, Cu, and SiO_2 no combined Auger decay is observed despite overlap of the singlet Exciton E1 with the CB. This is a consequence of substrate hybridization and is covered in Chapter 4.2.2.4. An indication is already found here in the high lifetime of the pre-edge shoulder E1* for monolayer Graphene of about 1.4 - 2.1 fs. In addition E1* is separated by about 1 eV from E1 and is 0.3 eV below Fermi energy (Figure 3.24). Hence this feature is cannot be attributed to an Exciton but rather to a hybridized carbon metal-substrate state as discussed in Chapter 4.2.2.4.

Thus, the combined Auger decay is very sensitive to structural details (substrate screening, substrate interaction, and interlayer interaction) and modifications of the lifetime of the singlet Exciton i.e. overlap with the CB.

Table 4.4: *Lifetime of Polaron and Exciton, extracted from XAS measurements.*

Charge state	**FWHM / eV**	**Lifetime / fs**
PCBM E_S (π^*_1)	0.45	1.5
P3HT E_S	1.9	0.35
P3HT E_T	0.6	1.1
P3HT $P_{(0-3)}$	0.4 – 0.5	1.3 – 1.6
HOPG	1.0	0.7
HOPG Polaron	0.5	1.3
AO-2/AO-4 E1	1.09 – 1.18	0.6
ML/Ni(111) E1 (E1*)	1.22 (0.32)	0.5 (2.1)
ML/Cu E1 (E1*)	1.21 (0.46)	0.5 (1.4)
ML/SiO_2 E1 (E1*)	1.21 (0.37)	0.5 (1.8)

The localized singlet excitonic state with its long lifetime and low Exciton binding energy – enabling a significant overlap with the CB – gives rise to the combined Auger decays. On the basis of HOPG and Graphene flakes the combined (S+P), (S+S), and (S+S)* Auger decay will be discussed in the following.

4.2.2 Auger decay channels

Only singlet Excitons give rise to the combined Auger decay as they have a significant overlap with the CB and can thus also be identified by a FANO resonance.

For an existing singlet excitonic in-gap state in Graphene systems a FANO transition is observed for the excitation of σ states with an initial state energy of -18 eV and -15 eV below the π*-resonance (see Figure 4.4, Figure 3.17, and Figure 3.21).

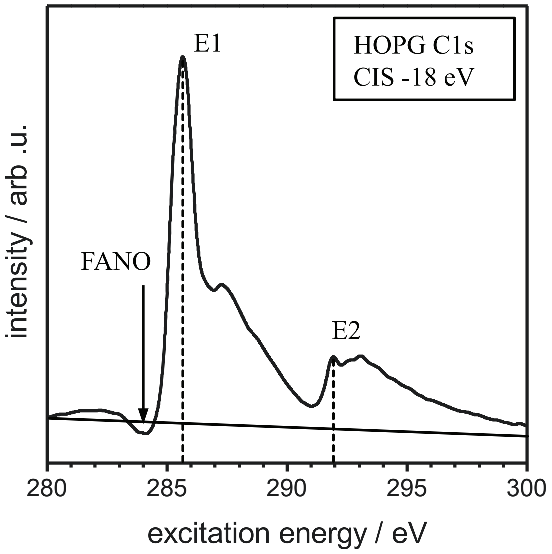

Figure 4.4: *FANO resonance of HOPG at a constant initial state energy of -18 eV.*

The lifetime and screening of the excitonic in-gap state determines the magnitude and presence of the FANO transition.

The intensity of the FANO- and of the first π*-transition at 285 eV are reduced for pure Graphene flakes compared to HOPG. This is an indication of a lower concentration of the excitonic in-gap states in Graphene.

The higher FWHM of the π*-transition of pure Graphene flakes compared to HOPG also indicates a lower lifetime of the Exciton by more than 10 % (Table 4.4). These changes may already be enough for the (S+P) decay to disappear in Graphene flakes. Especially the change in lifetime and localization of the excitonic state due to non-existence of interlayer coupling can be made responsible for the absence of the (S+P) Auger decay channel in Graphene and appearance of the (S+S) and (S+S)* decay.

Substrate screening and hybridization of metal 3d - carbon 2p states will further reduce the lifetime of the excitonic state. The consequence is a dramatic reduction in the intensity of the FANO transition. For strong substrate coupling no FANO transition is observed. A new pre-edge feature E1* is found 0.3 eV below Fermi energy with a long lifetime (1.4 - 2.1 fs). The implication is that the singlet excitonic states are completely attenuated. This scenario is found in the resPES diagram of ML/Ni(111), ML/Cu, and even ML/SiO_2 (Figure 3.23). Here no FANO transition is observed indicating that transitions to the excitonic in-gap states are completely hindered.

In the next four sections the (S+P) decay (interlayer interaction in HOPG), the (S+S) decay (intralayer Exciton in Graphene), the (S+S)* decay (intralayer Exciton in Graphene), and the pre-edge decay (substrate interaction in monolayer Graphene) is discussed and a model for each Auger decay combination is given.

4.2.2.1 The (S+P) Auger decay

HOPG is the prototype for the (S+P) Auger decay, because of its well-ordered layer structure, interlayer interaction and clear separation between 67.5° and 45° propagation of the two separate Auger decays. In the resPES data of HOPG the π*-resonance show a different Auger decay profile when compared to the Auger decay in the σ*-region. As shown in Figure 3.17, in the π*-region the Auger decay appears under α= 67.5° (S+P) while in the σ*-region the Auger process proceeds with α= 45° (S).

The ordered multilayer structure of HOPG facilitates carbon layer interaction and opening of small band gaps at the K-point. This enables the formation of singlet excitonic states [ALZ09]. The photo-excited electron will be trapped by these localized states. Interlayer interaction singlet Excitons will be formed due to the trapping, which contribute to the strong resonance at 285.5 eV. CIS spectra of the π-band region show that the excitation of π-band states primary forms singlet Excitons, as the corresponding CIS spectrum mainly consists of the first π*-resonance feature (Figure 3.19).

These localized singlet excitonic states have a long lifetime, as evident by the low FWHM and high intensity of E1, account for the FANO resonance below the first resonance in the σ-region, and induce the (S+P) Auger decay. The low intensity of the normal Auger decay (not noticeable in the resonance profile) and the absence of valence band photoemission underline this conclusion (Figure 3.17).

Therefore, this novel Auger decay can be found in any carbon thin film containing a well-ordered structure of multiple carbon layers with a strong singlet excitonic resonance. This as well includes crystalline polymer-structures of rr-P3HT (Figure 3.4) and PCBM (Figure 3.11).

The singlet excitonic state mainly decays into two channels: the larger part (>60 %) is deactivated by scattering into low-energy excitations (e.g. plasmons) or scatters at defects while the rest decays via the (S+P) Auger mechanism.

For HOPG as the model system of the (S+P) Auger decay these different contributions can be quantitatively extracted by the analysis of the intensity of the π*-region (intensity of E1, Auger decay intensity and intensity of additional superimposed resonances). The analysis shows that 10 % of the excitations lead to the (S+P) Auger decay and 63 % are scattered at singlet interlayer Excitons.

Structural defects or a distortion of the sp^2 band structure lead to localized (analogue to molecular orbitals) features superimposed in the XAS data between 285 eV and 290 eV. Contributions of carbon adsorbates are also visible in this excitation energy region. The contribution of adsorbates and structural defects amounts to 27 % of the XAS spectrum in the π^*-band.

However the resonances at 287.5 eV (+2.5 eV) and 289 eV (+4 eV) (Figure 3.17 and Figure 3.19) are not solely due to adsorbates. The resonance at 287.5 eV can rather be attributed to a polaronic level at the Γ-point with the Γ-point resonance being at 289 eV. This assumption is also confirmed by a pre-edge resonance at an excitation energy of 282 eV as the second polaronic level at the Γ-point.

Four main requirements for the (S+P) Auger decay can be derived from the measurements (Figure 3.17 and Figure 3.18) and are included in the (S+P) model.

First it is necessary to have a localized state inside the band gap of the material. For well-ordered carbon thin films singlet interlayer Excitons act as the localized state. The localized state is evident in the data by a strong FANO resonance at a binding energy of E_{bind}= -18 eV indicating a localized state slightly above the Fermi energy.

Secondly, the lifetime of the intermediate state (electron is bound to the localized state after its excitation and relaxation) has to be higher than the one of the spectator decay (Table 2.1). The FWHM of the singlet excitonic resonance E1 is indirect proportional to the lifetime of the intermediate state ($\tau \propto 1/\Gamma$). By comparing the FWHM of E1 of HOPG to the one of Graphene the higher lifetime of the singlet excitonic feature is evident ($FWHM_{HOPG} < FWHM_{Graphene}$; Table 3.6).

Thirdly, a high mobility and delocalization (Bloch wave function) of the valence band states are required for the recombination of the second core hole, which is given only in covalent bands. This is a natural property of sp^2-hybridized systems like rr-P3HT, PCBM, and HOPG [HEE01], [KAR03]. Both decay channels, spectator (step 4 in Figure 4.5) with E_{kin}= 267 eV and participator (step 6 in Figure 4.5), are evident in the Auger difference spectrum (Figure 3.18) and in the resPES diagram (Figure 3.17) as proposed in the (S+P) Auger decay model.

Finally, this mechanism becomes possible only at resonances where a high density of core holes is available. Because of the high photon flux of the synchrotron X-ray source this requirement is fulfilled in this case.

The (S+P) Auger decay model based on these requirements and the spectroscopic observations in this work is presented in the following.

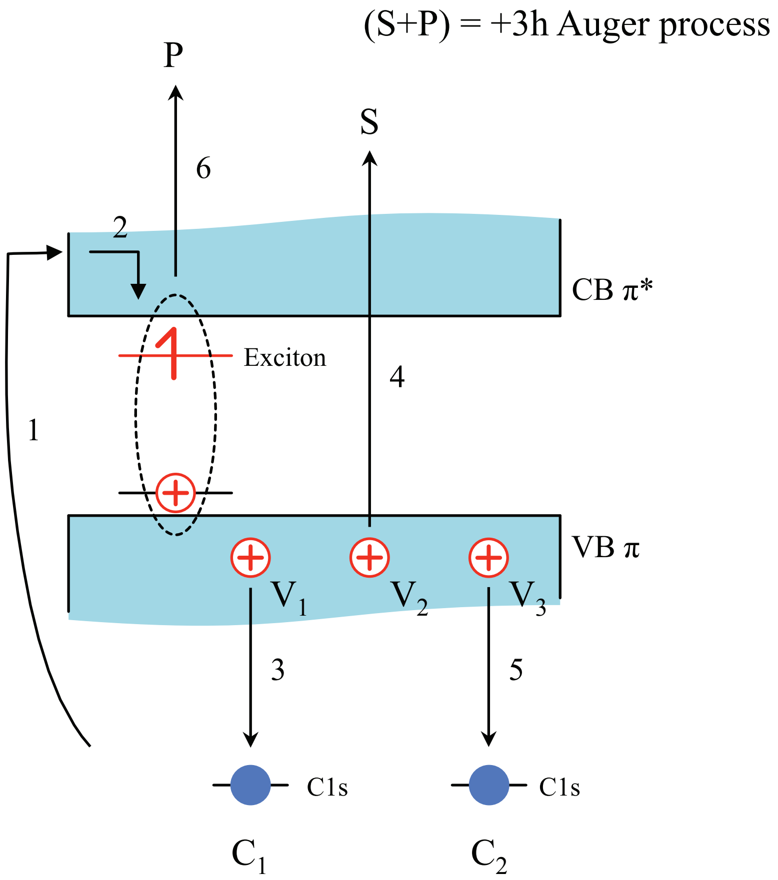

Figure 4.5: *Schematic picture of the singlet interlayer Exciton – (S+P) Auger process.* C_1 *and* C_2 *are core holes of two carbon atoms. The* V_1*,* V_2*, and* V_3 *are three final valence hole states. The trap state can be assigned to the singlet interlayer Exciton state. The initial excitation and relaxation of the excited core electron (step 1+2) is followed by a KLL spectator decay (step 3+4) and a participator decay {(S+P) decay} of the initial excited electron (step 5+6).*

The (S+P) Auger decay process is a final state process in which the primary core hole at the C1s level is filled to cause three valence holes V_1, V_2, and V_3. The resulting kinetic energy is transferred to the resonantly excited electron to leave as a participator electron. Figure 4.5 is illustrating this process of the (S+P) Auger decay.

The first step (1 in Figure 4.5) involves the creation of the primary core hole at the C1s level and the excitation of the electron over the band gap into an empty state in the π*-band system. This electron relaxes in step 2 (2 in Figure 4.5) into an empty localized state (singlet excitonic level). Here the electron is stabilized by the Exciton binding energy. This means it has a longer lifetime compared to a conduction band electron and consequently also higher lifetime than the spectator decay, which follows the previous step.

The normal C-KLL Auger decay involves now step 3 and 4 (see Figure 4.5). The primary core hole is filled from one valence electron and a second valence electron escapes the material as an Auger electron yielding valence holes V_1 and V_2. Up to this point the process is just a typical spectator decay.

The (S+P) Auger decay process now involves the trapped electron, which becomes emitted as a participator Auger electron, before it would decay by low energy decay processes with longer lifetimes than a fast Auger decay (e.g. plasmons, phonons or scattering at defects). The decay of the trapped electron must be distinguished from a common participator Auger decay, as the trapped electron has to find another suitable core hole because the original core hole was already filled.

The trapped electron will take any bypassing hole state and considers it as a virtual initial state. It can be released when one of these core holes will be filled by a third valence electron by creating the third valence hole V_3 (5 in Figure 4.5). Thereby the energy is transferred to the electron in the localized trapped intermediate state and it becomes emitted as a participator Auger electron (6 in Figure 4.5).

The result of the complete decay of the trapped electron is a combined spectator-participator Auger decay mechanism (C1s-V_1-V_2-S-V_3-P). It requires that the valence holes are delocalized covalent bonded π states and the Auger decay process is no longer atomic-like. The coupling of the valence electrons to the core holes is by the covalent interaction within the π-band, not by Coulomb interaction. Insofar, it must not necessarily be the next neighbour core hole, which enables the V_3-P decay; it could be any other core hole as the energy is transferred to a delocalized valence electron (represented by Bloch wave functions).

In the literature, resonant Raman Auger and post-collision interaction are other models to explain similar effects in terms of deviation from the normal spectator Auger decay propagation in the vicinity of resonant excitation.

Auger resonant Raman scattering leads also to deviations from the constant kinetic energy of the normal Auger decay shifting the energy of the Auger electrons to higher and lower kinetic energies [FOE02]. Below the core level threshold resonant Raman Auger decay shows linear dispersion with the excitation energy and changes at the threshold to constant kinetic energy. In the close environment of van Hove singularities the kinetic energy decreases and the initial value is regained after leaving the vicinity of the singularity [FOE02]. However, in the (S+P) Auger decay model, the magnitude of the Auger electron energy shift is constant and only depends on the number of holes in the final state and therefore should be independent on the method of ionization at the resonance. The energy shift starts above the core level threshold, not below, and is maintained until approximately the ionization threshold is reached. In terms of the $E_{bind}(\hbar\omega)$ diagram a linear dispersion with a slope of 67.5° is observed for the (S+P) Auger decay and a slope of 45° for the spectator Auger decay (see relation 24).

PCI describes the interaction of a high-energy Auger electron with a low energy electron [COW00]. However, as this model is based on slow free electrons, this effect would not be visible until the ionization threshold is reached. In the resPES diagram data this should take place above 290 eV excitation energy (Figure 3.17), therefore it is not corresponding to the (S+P) Auger decay.

PCI at the resonance below the ionization threshold is described as the inherent post-collision interaction [OHN01]. Here the electron is captured in a band (metallic or localized virtual charge transfer band) or in an empty bound level splitting from the former band by an attractive Coulomb core-hole potential. Two scenarios are discussed in this model. In the unscreened case the effective holes-excited electron interaction energy U_f is lower than the effective core-hole-excited electron interaction energy U_c. The delocalized excited electron gains energy and the Auger electron loses energy. On the other hand, in the case $U_f>U_c$ (screened case) the excited electron loses energy and the Auger electron gains energy. In the former case the excited electron in its final state is located in a band whereas in the latter case the electron stays in a bound state. In the inherent PCI only a spectator Auger electron is emitted with two holes in the valence band in the final state.

The inherent PCI model can also be applied onto a wide domain of the (S+P) Auger decay model. Up to step 4 in Figure 4.5 the (S+P) decay is similar to the inherent PCI with $U_f>U_c$.

In the resPES diagram this is seen as a shift of the kinetic energy of the spectator Auger decay. The spectator Auger decay is shifted by about 3 eV in the π*-region to higher kinetic energies (E_{kin}= 267 eV) compared to the spectator Auger decay in the σ*-region with E_{kin}= 264 eV.

But for the full description of the resPES wallpaper (the 67.5° Auger transition) the decay of the excited electron has also to be taken into account; here the inherent PCI is not sufficient to explain the data. The signature of the decay of the excited electron is found in the Auger contribution spectra in the π*-region at high kinetic energies (low binding energies in Figure 3.18).

In the resPES spectra of rr-P3HT Polarons and triplet Excitons predominate with only a small singlet Exciton induced (S+P) Auger decay feature in the π*-band (Figure 3.4). The spectra of PCBM is governed by molecular orbital resonances that are superimposed by the (S+P) and spectator Auger decay and their presence is thus difficult to identify (Figure 3.11).

Perfect free-standing monolayer Graphene (a single layer of HOPG) does not exhibit any interlayer or substrate interaction. Two different multiple Auger decays that will be explained in the following characterize it. In Graphene the initial excited core electron does not take part in the decay process. Hence, the (S+P) Auger decay is replaced by an (S+S) Auger decay cascade.

4.2.2.2 The (S+S) Auger decay

Without interlayer interaction in Graphene the (S+P) decay is replaced by a combination of an (S+S) and (S+S)* decay at resonance. The initial excited core electron does not take part in the decay process. First the (S+S) decay is discussed being very similar in its decay behaviour as the previously discussed (S+P) Auger decay.

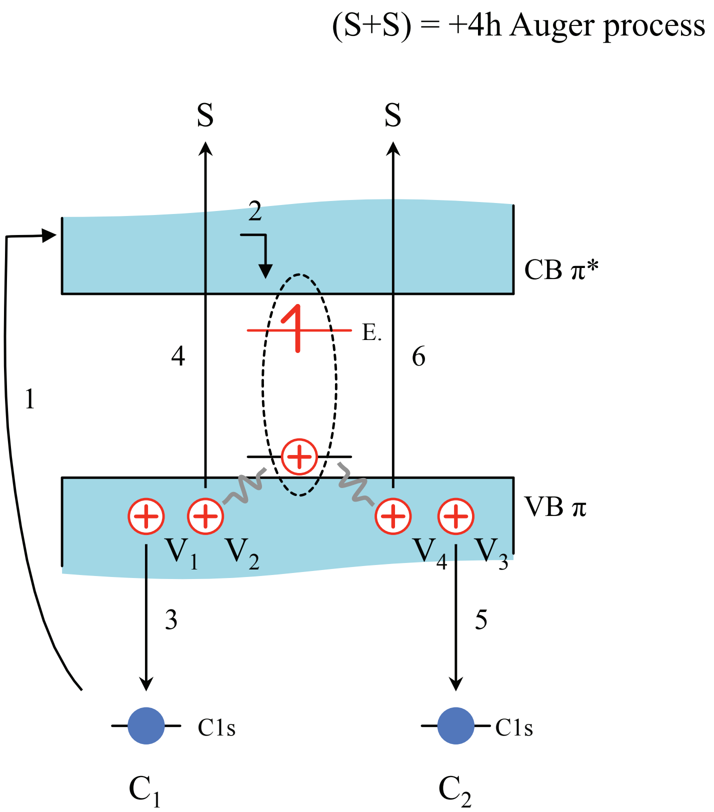

Figure 4.6: *Schematic picture of the (S+S) Auger process.* C_1 *and* C_2 *are core holes of two carbon atoms. The* V_1, V_2, V_3, *and* V_4 *are four final valence hole states. The initial excitation and relaxation of the excited core electron (step 1+2) is followed by an initial KLL spectator decay (step 3+4) and a second KLL spectator decay (step 5+6). The initial excited electron remains trapped in the excitonic intermediate state.*

The α= +78.75° Auger decay (S+S) is described in the following by means of Figure 4.6. With the creation of the initial core hole (step 1) the core electron is excited under resonance into the unoccupied CB. This initial step does not result in the generation of a core Exciton, as this would involve a transition from the core level into a level below the 'principal' minimum of the CB. After the excitation into the CB the electron will relax into a lower state stabilized and screened by a polarization which causes a 'virtual' hole pulled up from the VB (step 2). As a consequence this e-h pair becomes localized. It will no longer behave as a charge carrier described by Bloch wave functions.

The binding energy of this e-h pair is lower than the one of a core Exciton as it is less localized. It is formed at the π-π* band gap at the M-point [CHA11], [MAK11]. Parallel to the relaxation of the initial excited electron into the e-h state the initial core hole is filled in the third step by one π-band electron and the energy is transferred to a π-band (VB) electron that scatters at the weakly localized e-h (step 4). Because of the scattering with the e-h pair the energy of the spectator Auger decay is shifted by 3 eV to higher kinetic energies compared to the normal KLL spectator Auger above the ionization threshold (Figure 3.21a and Figure 3.21b) [OHN01]. The lowering of the energy of the core electron after the excitation into the CB by relaxation into the excitonic state by $U=U_f-U_c$ (change in effective core-hole-excited electron interaction energy) is increasing the kinetic energy of the KLL Auger electron (E_{kin}= 267 eV) as visible in the spectra (downshift of the Auger line) [OHN01]. This effect is also known as inherent post collision interaction (inherent PCI) as it appears below ionization threshold but above core-level threshold [OHN01].

The (S+S) Auger decay involves now a second core hole that becomes filled by a third valence electron. For the (S+S) decay the energy from the decay of the second core hole has to be transferred to another valence electron that becomes emitted as a second spectator electron (step 5 and 6). The communication between the two KLL Auger decay processes is handled by the scattering of the delocalized VB electrons at the localized e-h pair, as the e-h pair is present over the complete time scale of both decays. Obviously the lifetime of the e-h pair has to be long enough to allow a coupling of the two spectator decays under the spectating initial photo-excited core electron.

In total the (S+S) Auger decay is a combination of two spectator decays – scattered at an Exciton – and a net four hole final state with one additional virtual hole in the e-h pair.

The scattering process is the key mechanism to understand the building of combined Auger processes at all. It is based on the fact that localized hole states – by polarization effects – coexist with delocalized Bloch like valence holes.

For Graphene flakes also a second combined Auger process is observed (S+S)*. The asterisk denotes to the fact that the initial excited core electron is not trapped in a singlet Exciton. It rather perturbs an already existing singlet Exciton and the excess energy is transferred to two spectator Auger decay indicated by the asterisk.

4.2.2.3 The (S+S)* Auger decay

For the Graphene flakes (Figure 3.21) an additional feature on the lower excitation energy side is found which mirrors the (S+S) Auger decay. Both decays together, the (S+S) and (S+S)* Auger decay, are giving the lower binding energy region of the π*-resonance at 285 eV a V-like shape. The slope of this decay is inversed to the one of the (S+S) Auger decay (α_{+4h}= +78.75° and α_{-4h}= -78.75°). Because of the negative slope this decay has to be handled as an Auger-Gain decay process. With increased excitation energy the kinetic energy of this Auger decay is gradually increased in contrast to other Auger decay mechanisms with constant or decreasing kinetic energy. However, to enable such an Auger-Gain decay excess energy has to be transferred to the Auger electron.

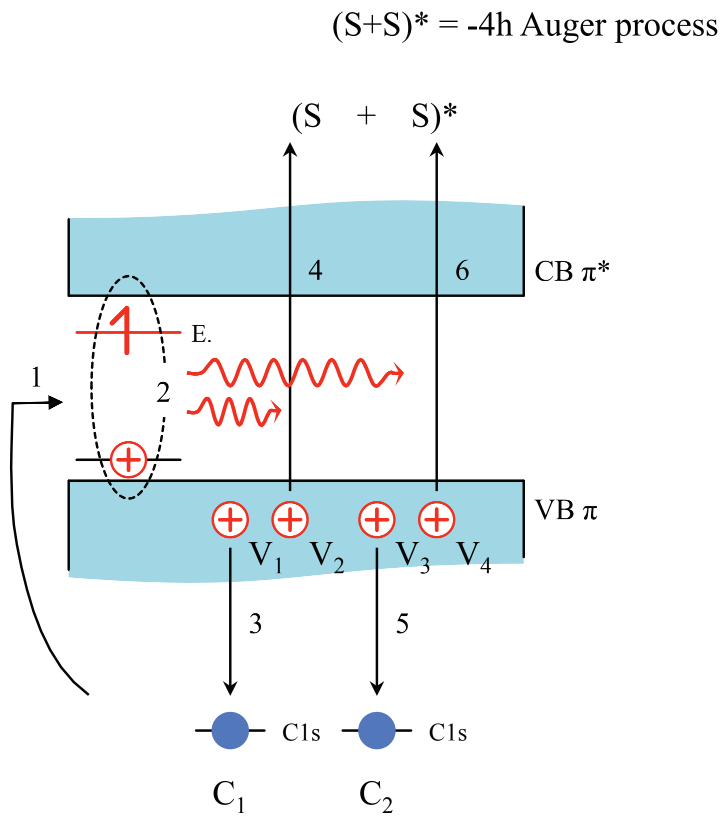

Figure 4.7: *Schematic picture of the (S+S)* Auger process. C_1 and C_2 are core holes on two carbon atoms. The V_1, V_2, V_3, and V_4 are four final valence hole states. The initial excitation below the CB (1) into the gap perturbs and destroys the Exciton (2). The excess energy is transferred to a subsequent double spectator decay (3+4) and (5+6).*

In close vicinity of the first π*-resonance a high amount of e-h pairs is expected to exist. Low energy decay processes can create these e-h pairs after direct photoemission of VB electrons. Below the core level threshold a core electron that is excited to a level below the minimum of the CB (for the (S+S) it has to be excited above the CB) will perturb the existing e-h pairs (step 1 in Figure 4.7). The perturbed e-h pair will decay under the release of its energy (step 2).

This excess energy, about 0.5 eV to 1 eV, is transferred to the combined double spectator Auger decay (S+S)* (step 3+4 and 5+6). The asterisk denotes the fact that this process has gained excess energy. Close to resonance a high amount of core holes is found to be already present.

Analogue to the (S+S) Auger model the two simultaneously spectator decays, however here with a minus sign (-78.75°), give rise to a -78.75° slope in the resPES diagram. A high lifetime of the Excitons is again needed.

4.2.2.4 The low E_{kin} Auger decay

In contrast to the Graphene flakes monolayer Graphene on a metallic substrate (nickel, copper, and even SiO_2) does not exhibit the (S+P), the (S+S), or the (S+S)* Auger decay at the carbon K-edge. This is due to substrate interaction as indicated by the corresponding C1s core level spectra of monolayer Graphene. They are considerably broadened compared to Graphene flakes and even show a double peak in the case of ML/Ni(111) (Figure 3.14a).

The C1s double peak for ML/Ni(111) is discussed to arise from two different carbons to nickel distances. The α Graphene sub lattice is on top of a Ni atom and the β–sub lattice on top of a Ni hollow site (see Figure 1.8a) [SCHU12], [VAR12]. It is also attributed to corrugation of the Graphene layer [PRE09], [SCHU11].

The metal interaction also leads to hybridization of Ni3d states with the π-band states of Graphene [MIT11], [VAN10], [VAR08]. Even the lifetime of the intermediate state in the resPES data is influenced. In fact, in the resPES profile a strong localization above the π*-resonance is found, only above the σ*-resonance the common C-KLL Auger emission is observed.

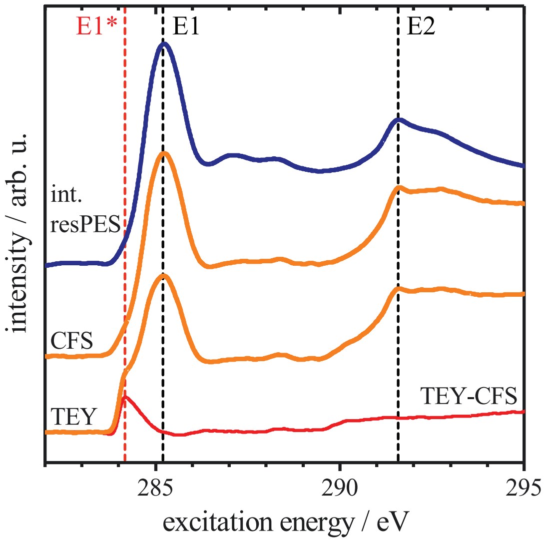

Figure 4.8: *TEY XAS spectra of monolayer Graphene on Ni(111). A CFS 264 eV, an integrated resPES diagram spectrum, and a difference spectrum of TEY and CFS are included for ML/Ni(111).*

In the XAS data of monolayer Graphene an additional shoulder (E1*) at the first π*-resonance in the total electron yield spectra is found (Figure 3.15).

The resonance E1* is not present in the corresponding resPES diagrams. In Figure 4.8 the resPES diagram of ML/Ni(111) is represented by its integral over the initial state energy. In addition a CFS 264 eV and a TEY spectrum for ML/Ni(111) are included. In order to emphasize this finding a difference spectrum (Figure 4.8 red spectrum) of the TEY and CFS spectra of ML/Ni(111) is added indicating an asymmetric pre-edge peak at an excitation energy of 284.2 eV.

The pre-edge peak in the ML Graphene XAS spectra is discussed in the literature to arise from doping exposing new unoccupied states below the Fermi energy [SCHU11], [SCHU12]. New unoccupied states or states due to doping should be visible at the resonant valence band spectra. No such states are visible in Figure 3.23. Valence band states up to a binding energy of -35 eV and Auger decay contributions above a kinetic energy of 250 eV that should be present for doping or new unoccupied states can be ruled out.

The pre-edge feature E1* is only present in the TEY spectra whose main intensity comes from low energy contributions. Pacile et al. used the TEY mode and Schultz et al. the transmission mode for their studies giving similar results [PAC08], [SCHU11].

The peak E1* is 0.3 eV below the Fermi energy that is almost exactly the separation of the two carbon core levels. Still the double C1s core level peak cannot be responsible for the XAS pre-edge peak as both C1s core levels have almost equal intensity but E1* is only about 5 % of E1. The pre-edge peak E1* is only found in TEY, not in the CFS or resPES diagram. It is at a lower excitation energy whereas the second C1s core level is at a higher binding energy. Hence, an overlap of two XAS spectra from the two C1s core levels can be excluded. Also the work function energy of Graphene is about 4.2 eV to 4.5 eV [KWO12], [XU13]. Plasmons and Excitons don't provide this amount of energy necessary for ionization of VB states.

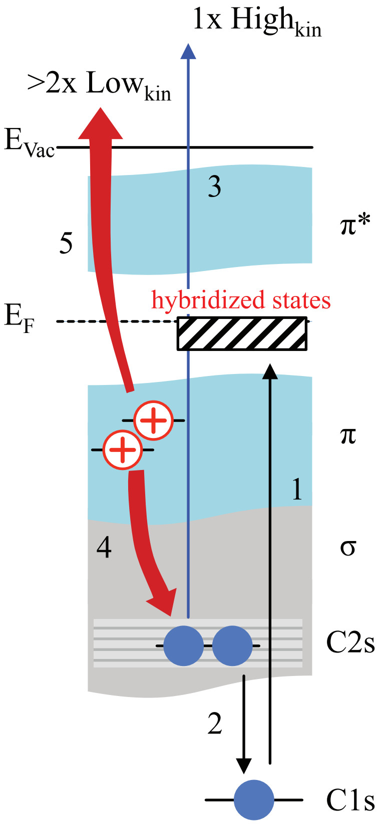

Figure 4.9: *The pre-edge peak in Graphene TEY XAS is due to a low kinetic energy Auger decay cascade.*

Based on the findings in this work a new model for the pre-edge peak is proposed (Figure 4.9). The hybridization of metal 3d and Graphene π-orbitals is a consequence of strong metal substrate coupling [MIT11], [VAN10], [VAR08].

New in-gap states are induced at and below E_F, in case of ML/Ni(111), by the Ni3d-C2p hybridization (in the other cases: Cu3d-C2p and Si3p-C2p). The hybridization also influences the lifetime of the intermediate excitonic excitation changing it to unfavourable conditions for an (S+P), (S+S), or (S+S)* Auger processes.

E_F is defined in the resPES diagram by the binding energy of the C1s core level. The core level is found at a binding energy of -284.5 eV (Figure 3.14a). Indeed the pre-edge resonance in the TEY data is found at an excitation energy of 284.2 eV and -0.3 eV relative to E_F. This coincides with the initial state energy of the Ni3d states.

After resonant excitation of the C1s core electron into the pinned in-gap state at 284.2 eV (step 1) it cannot take part anymore in a participator Auger cascade as the excited electron is transferred directly to the metal due to hybridization and therefore it is not available to an Auger decay process. In consequence a KL_1L_1 spectator Auger decay (E_{kin}= <250 eV) fills the core hole (step 2+3) where the spectator electron has been transferred to the metal substrate. The KL_1L_2 with E_{kin}= 264 eV is attenuated as the L_2 states (π-band) are hybridized with the metal states. The two C2s holes can be further decay via two low kinetic Auger decays or a cascade with more then two emitted electrons {Figure 4.9, step 4+5)}.

The spectator decay will only yield a single electron of <250 eV kinetic energy (<-36 eV initial state energy). In comparison to the ≥2 low kinetic energy electrons the intensity of the high kinetic energy decay channel is rather small. Indeed a strong pre-edge resonance in the low kinetic energy TEY spectrum is found (Figure 4.8). A shallow increase in intensity at -35 eV initial state energy in the resPES diagram of ML/Ni(111) (Figure 3.23a) indicates the presence of the high kinetic energy decay channel of the pre-edge resonance.

The metal induced pinning of the π-system is attenuating the resonant excitation into the excitonic state. In consequence also the spectator Auger decay with a 2h final state lose in intensity (E_{kin}= 264 eV). Therefore decay processes involving excitonic bound electrons like (S+P), (S+S), (S+S)*, and the FANO transition are quenched.

Indeed, for ML/Ni(111), for ML/Cu, and for ML/SiO_2 none of these decay processes are observed.

4.2.3 Conclusion - Graphene

By resonant photoemission and X-ray absorption spectroscopy new resonant Auger decay processes could be identified. They could be assigned to a combined spectator-participator (S+P), to a combined double spectator (S+S) Auger, and to a double spectator (S+S)* Auger-Gain decay. For each of the three new resonant Auger decay combinations a model was introduced.

The (S+P) process deviates from the normal continuum Auger decay. It is characterized by a net 3h final state with the number of holes determining its slope in a $E_{bind}(\hbar\omega)$ diagram of 67.5°. Interlayer coupling (van der Waals force for HOPG or π-π stacking for rr-P3HT) is found to give rise to the (S+P) Auger decay process in carbon films. The physical origin is the interaction of the photo-excited electron with singlet interlayer Excitons close to the CBM. The localized states involved in the combined (S+P) Auger process are also accompanied by a FANO profile transition in the pre C1s edge resonance region. The FANO resonance is used as a fingerprint to identify the presence of singlet Excitons in HOPG and in Graphene.

In Graphene flakes no interlayer interaction is present. For pure Graphene the (S+P) Auger decay is replaced by a combination of an (S+S) and an (S+S)* Auger decay. The scattering of the spectator Auger electrons at one single Exciton facilitates the double spectator decay. This process is determined by the scattering time rather than the lifetime of the singlet Exciton. The (S+S) and (S+S)* Auger decay is assigned to be characteristic for free-standing Graphene.

For monolayer Graphene metal substrate induced screening of the π electrons suppresses the Auger decays completely in the π*-band. Only when the upper σ*-bands are involved the C-KLL Auger process appears. Instead a low E_{kin} Auger decay cascade appears as an alternative decay channel that gives rise to the pre-edge π*-resonance at 284.5 eV. This process indicates that by the metal interaction for instance for Nickel as a substrate Ni3d-C2p hybridized states at the Fermi energy are existent and become involved. Hybridization influences the Exciton lifetime and the electron-Exciton scattering time in a negative way. Instead of the excited core electrons getting localized in a singlet Exciton, they are getting trapped in the metal-carbon hybridized states. The hybridized states have a significant higher lifetime and reduced overlap with the CB of Graphene as indicated by the low FWHM of the corresponding transition E1* and the absence of a FANO transition.

Thereby resonant photoemission is very sensitive to the existence of defects, interlayer interactions, and screening and polarization effects. The observation of the resonant behaviour at the C-K edge can provide a novel and powerful tool to learn about the influence on the Graphene properties by the underlying metal or oxide substrates.

As the multiple Auger decay requires localized in-gap states that have a significant overlap with the CB states (e.g. singlet Excitons) it should be also observed for other systems. TM-Oxides are known to exhibit polaronic and Excitonic effects [MCK12], [VARL12]. Excitation into these levels therefore should also induce multiple Auger decays. The next chapter will focus on one particular TM-oxide: Co-PI (cobalt oxide) which is used as a catalyst for the oxygen evolution reaction in photo-electrochemical cells.

4.3 Co-PI - Water oxidation catalyst

Multiple combinations of Auger decays are not only limited to sp^2 hybridized carbon systems. One requirement for multiple Auger decays is that an intermediate state with a long lifetime exists which can act as a trap level to enable further combinations of Auger decays. For sp^2 hybridized carbon systems it is a singlet excitonic state whose FWHM (lifetime $\tau \propto 1/\Gamma$) is in the same order as the one of its binding energy in order to ensure sufficient overlap between singlet Exciton and VB states.

In all concepts of the new multiple Auger decays (S+P), (S+S), and (S+S)* two core holes are necessary which have to have an overlap with the VB states of neighbouring atoms to enable the decay of a core hole from one atom by a VB electron from another atom. The delocalized π-band of sp^2 hybridized carbon systems naturally give this. But it is not limited to homogeneous systems. The (S+P) Auger decay can also be observed for instance at the N1s edge of CoPc[****] which indicates hybridization of C and N atoms. Here one C1s and one N1s core hole are involved.

As already stated in the paper by Ohno [OHN01] the inherent PCI is not limited to metallic systems (like HOPG and Graphene) but can also appear in CT systems.

Hence, also in CT systems combinations of Auger decays should be observed, for instance the (S+P) decay.

Transition metal oxides are an example for CT systems, which are also widely used as catalysts [GAR11], [MUE10], [SUB12]. For TM-oxides Polarons and Excitons are also existent. These small Polarons are highly localized on one or several anion sites [MCK12], [VARL12]. Core level excitation into these small Polarons – also called self-trapped holes – can create a self-trapped Exciton.

By a ligand (O2p) to metal (TM3d) charge transfer holes are created on the oxygen side. These can form STHs by lattice displacements, which act as traps for excited electrons – for instance at the O1s resonance – out of which form self-trapped Excitons can be formed. Further, STXs can give rise to the multiple hole Auger decay.

[****] Unpublished data: N1s resPES of CoPc indicating (S+P) and (S+S) Auger processes.

In the following section the results on the TM-oxide catalyst Co-PI (cobalt oxide) will be discussed. The influence of the multiple Auger decay on this catalyst and its properties is a central point in this discussion as well as the identification of the cobalt spin state by making use of the characteristics of the different Auger decay mechanism at resonance.

First the structure and oxidation state of Co-PI is discussed on the basis of core level measurements. Second by a combined resPES study at the Co2p and O1s edge the cobalt spin state of Co-PI is identified. The presence of (S+P) Auger decays at the O1s edge is further used to identify two charge transfer states. Especially the Co^{3+} CT state is found to be important for catalysis as it energetically located at the $E^0(O_2/H_2O)$ redox potential of water splitting.

By knowledge of the presence of CT states identified by the (S+P) Auger decay an improved band scheme is proposed for Co-PI.

4.3.1 Structural and elemental analysis

The TM-oxide catalyst Co-PI is prepared by electrochemical deposition. Two possible structural motifs for the cobalt catalyst are under discussion, namely corner-sharing cubane structures or edge-sharing MCC (Figure 1.9) [KAN10], [RIS09b]. The coexistence of both structures is not expected.

Both, Dau et al. and Nocera et al. agree on the resulting relative Co-Co and Co-O distances derived from EXAFS analyses of the Co-PI catalyst. However, they favour the cubane and the MCC structure, respectively.

The group of Dau conclude for their "thick” samples that they have the cubane motif with a mean Co valence of 3+ [RIS09b]. In contrast, Noceras group deduces a valency of greater than three for bulk Co-PI and slight lower valency for surface Co-PI [KAN10]. They highlight the sensitivity of valency to cluster size. Based on their X-ray absorption near edge structure results the cobaltate motif is favoured. Both groups used the Co1s edge as the basis of their argumentation.

The possible MCC and cubane motifs of Co-PI share the same amount of cobalt content (Table 3.9). They only differ in the relative Co/O ratio (lattice and bridging oxygen) for small and medium clusters. Oxygen is also used for the surface termination in these clusters (non-bridging oxygen) in form of hydroxide and phosphate.

In general the cubane clusters comprises of less bridging oxygen than the MCC clusters – only around two third. With increased cluster size both motifs show a general trend in incorporating more oxygen into the lattice because of higher volume to border and surface ratio.

The model structures from Kanan et al. [KAN10] give a Co/O ratio of 0.88 (0.80) for cubane surface (bulk) and 0.58 (0.53) for MCC surface (bulk) (see Table 3.9). The size of the clusters plays an important role in the Co/O ratio as with increased cluster size (surface and bulk) the Co/O ratio decreases. This ratio defines the upper Co/O limit. The lower limit is for both around 0.3 when also the terminating/non-bridging oxygen is included.

The XPS analysis provides an additional parameter in that discussion, as the determination of the relative amount of the Co atoms, lattice O atoms, and neighbours (O, K, P) is possible.

From the deconvolution of the O1s core level spectra into water/phosphate and lattice/termination oxygen contributions the Co/O ratio of the lattice can be calculated. For the Co-PI Cat-A a ratio of Co/O of 0.57 is obtained. It has 77 % lattice oxygen. Cat-D is showing a high content of hydroxide and especially water (high binding energy shoulder at -532 eV) resulting in only <42 % lattice oxygen and a Co/O ratio of 0.34.

By using a linear chain and a sphere model as the shape of the cluster, the lower and upper Co/O ratio limit was calculated. The results for all Co-PI layers (Cat-A – Cat-D) are in the Co/O ratio window of the theoretical MCC motif (0.67 > Co/O > 0.28), which itself is also in the lower end of the much bigger cubane window (1 > Co/O > 0.25).

The low Co/O ratio of the Co-PI layer of Cat-D with Co/O= 0.34 has several reasons: the cluster surface to volume ratio is higher compared to Cat-A, an overestimation of the amount of lattice oxygen based on the O1s core level data is probable, a higher amount of phosphate termination can be the case, and structural defects can exist. None of these can be excluded. Still a higher surface ratio would be beneficial for catalysis. A slight overestimation of the lattice oxygen is indeed the case because not all conceivable contributions were included in the peak analysis (water, phosphate, bridging and non-bridging lattice oxygen, hydroxyl groups). Also, a low Co/O ratio is more probable for small clusters.

Based on the elemental analysis the possibility of the cubane structure cannot be ruled out. But, as the Co/O ratios of all samples are within the MCC-window and none have higher ratios than 0.6 – solely attributed to cubane – the interpretation of the Nocera group in term of the molecular cobaltate cluster model as proposed in [KAN10] is favoured in this work.

One more important aspect of the Cobalt catalyst, the oxidation state of cobalt, can also be determined by Co2p core level and XAS analysis. It is discussed in the next section.

4.3.2 Cobalt oxidation state of Co-PI

The Co oxidation state (Co^{2+}; Co^{3+}) can be derived by an analysis of the Co2p core level data. Each oxidation state of cobalt has characteristic Co2p core level spectra. In general, there are satellite features, which are characteristic for the Co^{2+} and the Co^{3+} states. Their position and intensity is characteristic for the cobalt oxidation state.

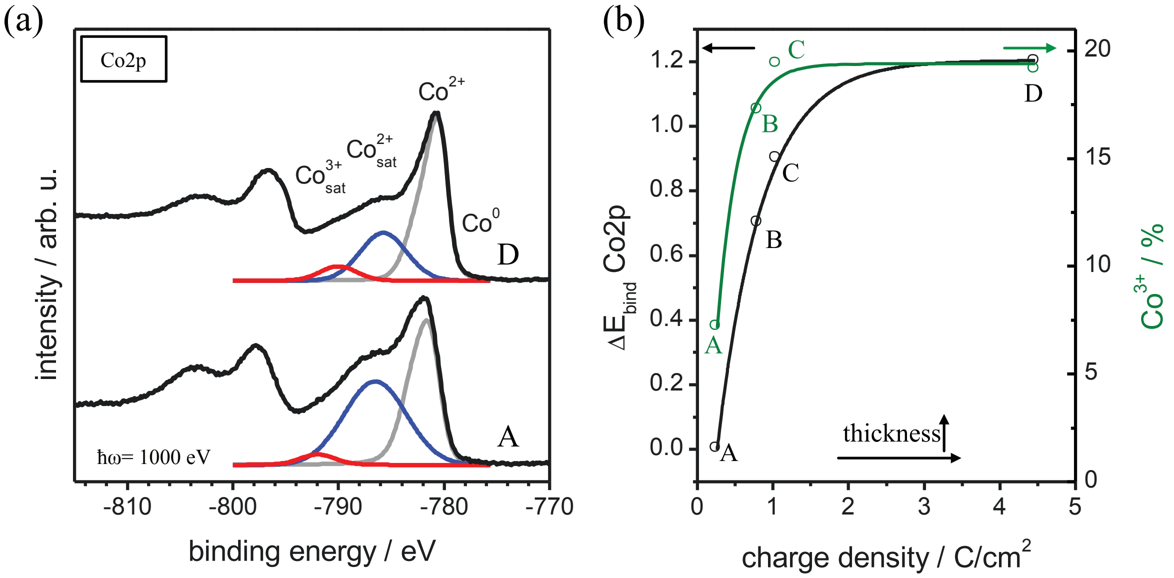

Figure 4.10: *Cobalt 2p core level of the catalyst Cat-A and Cat-D (a). Spectral decomposition: Co^{2+} satellite (blue) and Co^{3+} satellite (red). The area of the satellite peaks is used to estimate the amount of Co^{3+} (7 % Cat-A and 20 % Cat-D) (b). The progression of the Co^{3+} content is in agreement with binding energy shift of the Co2p core level.*

The Co2p core level spectra of Co-PI Cat-A shows a strong Co^{2+} satellite structure at 786 eV under absence of the corresponding satellite at 790 eV for Co^{3+} (Figure 4.10a).

By comparing the Co2p core level of the thin Co-PI layer to the one of the much thicker film of Cat-D the characteristic satellite peak for Co^{2+} is found to be attenuated. With a coexisting increase in the Co^{3+} satellite peak at 790 eV it can be concluded that with increasing layer thickness a rising admixture of three-valent cobalt is given (see Figure 4.10b). The existence of Co metal can be excluded by comparing the Co2p core level spectra to the one of a Co metal film as indicated by Co^0 in Figure 4.10a (compare to Figure 3.27a). By peak deconvolution the relative Co^{2+} and Co^{3+} can be obtained as indicated in Figure 4.10a. The results are given in Figure 4.10b. The Co^{3+} content is increased from 7 % for Cat-A to 20 % for Cat-D.

This saturation of the Co^{3+} content from Cat-C to Cat-D is also observed in the continuous shift of the Co2p core level and VBM (shift of E_F) towards lower binding energies as displayed for both the content of Co^{3+} and the shift of the Co2p core level in dependence of the deposited charge density in Figure 4.10b.

The position of the Fermi energy is shifted from mid-gap position (intrinsic or slight n-type) for a thin layer of Co-PI catalyst Cat-A towards p-type Co-PI for thick bulk Co-PI by 1 eV. Instead of a normal band bending, surface enrichment, or phase segregation the shift is therefore probable due to an increase in the cobalt oxidation state from CoO to Co_3O_4.

This conclusion is also assisted by the Co2p XAS and resPES spectrum of the Co-PI catalyst. The Co2p XAS of Cat-A (Figure 3.30a) looks similar to that of CoO, Co:ZnO, Co:CeO_2, and Co:TiO_2 [MUE08], [OPE08]. It is however rather different from $LiCoO_2$ [SCH10]. The former materials are based on Co^{2+} and the latter on Co^{3+} states.

In the Co L_3 TEY spectra (Figure 3.30a) six transitions are indicated by 1-6. According to multiplet calculations the transitions 1 and 5 are characteristic for Co^{2+} and Co^{3+}, respectively [CSI05], [HU04].

In addition the spin state of Co-PI can be derived from the TEY-XAS spectra. For a Co^{2+} high spin (HS) state the transitions 2 and 3 are higher in intensity than transition 4, as it is the case for Co-PI Cat-A (Figure 3.30a top and Figure 3.31a). For a low spin (LS) state instead of transition 2 and 3 only a single transition line lower in intensity than transition 4 is observed [CSI05], [KIM03].

A similar comparison in the XAS data can be done for Co^{3+}. For a Co^{3+} HS state a shoulder on the lower excitation energy side of the main XAS profile is expected and for a LS state a broad band on the higher excitation energy side [BUR06], [HAV06], [HU04].

As evident from the TEY XAS data of Cat-D (Figure 3.30a top and Figure 3.31b) the band on the high excitation energy side (transition 6) indicates the presence of the Co^{3+} LS state.

Despite this general agreement in determining the Co oxidation and spin state by using TEY XAS spectra and multiplet calculations, the advantage of recording the initial state resolved profile over the absorption edge (i.e. measuring a complete resPES profile) is that the resonant behaviour of individual initial states can be followed. It enables the assignment of coexisting spin and oxidation states and also the determination of their relative abundance. This new method is more reliable than the complex decomposition of the integral TEY-XAS data following the atomic multiplet splitting obtained from calculations. Based on resPES measurements at the Co2p and O1s edge a more detailed discussion of the oxidation state, the spin state, and the band scheme of Co-PI is possible. Here the multiple Auger decay is used to identify localized in-gap states and bands. It is covered in the next two sections.

4.3.3 Spin State of Co-PI by resPES

ResPES on the Co2p and O1s edge is used in the following to identify the spin, the oxidation state, the relative Co^{3+} content, and the energetic position of the Co ion as well as the existence of metal-to-ligand charge transfer states by use of the (S+P) Auger decay which are involved in the electronic structures of Co-PI.

In general, X-ray magnetic circular dichroism or magnetization measurements [OPE08] can be used to deduce the spin configuration (LS or HS) of Co-PI however the parallel identification of CT states with their particular spin is unique to resPES profile measurements. CT states when localized can be treated as STHs, which form STXs upon resonant excitation, which in turn give rise to a multiple Auger decay only detectable by a complete resPES profile measurement.

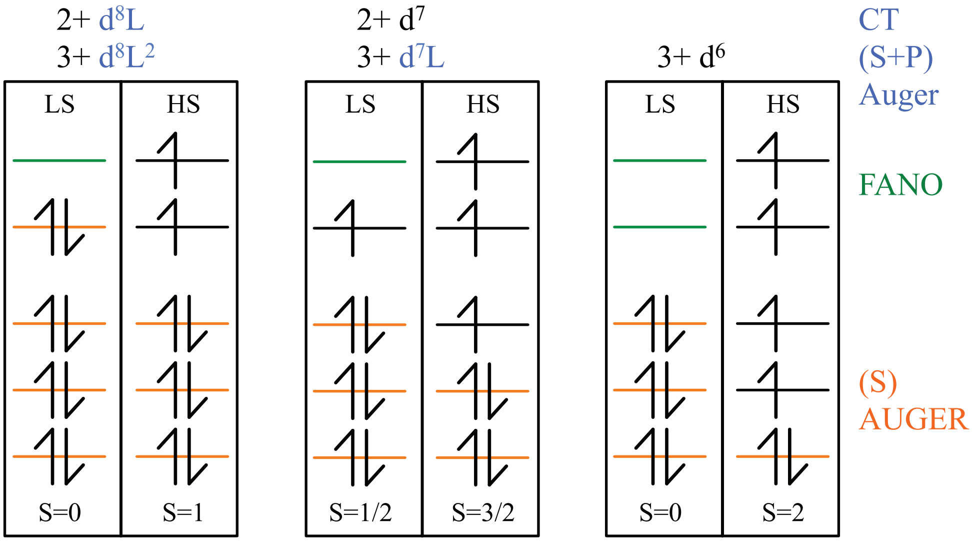

Figure 4.11: *Cobalt 3d configuration for 3d^8, 3d^7, and 3d^6 occupation. Completely filled 3d orbitals in a LS configuration cause a spectator (S) Auger decay (orange lines). A HS configuration favours the participator Auger decay. Empty 3d orbitals can give rise to a FANO resonance at the Co2p edge for CT configurations (blue). A CT is identified in the O1s resPES diagram by a combined (S+P) Auger decay.*

For the interpretation of the contributing spin states some systematic findings are used which are helpful for the interpretation of the resonance profiles. A LS state with its filled 3d orbitals can readily cause a spectator Auger decay (compare to Figure 4.11). For a HS configuration the coulomb operator selection rules (Equation 20) limits the formation of spectator Auger processes and favours participator decays, hence. With these considerations a LS and a HS system can be distinguished by resPES whether a spectator Auger decay (2h final state) or a participator Auger decay (1h final state) is observed, respectively. In addition, ligand-to-metal CT states can be identified which give evidence for particular localized states within the electronic structure of the catalyst. These show up as FANO resonances at the Co L_3 edge, are able to trap the photo-excited electron and cause the resonant decay into combined (S+P) channels at the O1s edge.

A FANO resonance at the Co L_3 edge accompanied by an (S+P) Auger decay at the O1s edge indicates a LS CT state whereas only an (S+P) decay at the O1s edge indicates a HS CT state (compare to Figure 4.11).

For Cat-A the resPES profile can be divided into three contributions (Figure 3.31a, lower panel). The two contributions with the highest intensity are found at an initial state energy of -11.5 eV and -7.0 eV, respectively. The resonance profile of these two bands is characteristic for participator (1h) Auger decays. From the core level studies it is known that Cat-A has a high amount (>90 %) of Co^{2+}. A pure participator scenario is only consistent with the Co^{2+} HS $Co3d^7$ (s= 3/2) state, as the LS configuration would favour a spectator Auger contribution. The absolute position of the Co valence band states reflects the spin state, and in particular the emission at around -7 eV is indicative of the Co^{2+} (s= 3/2) HS state, in agreement with Co:ZnO [OPE08]. This confirms the assignment of the two contribution at -11.5 eV and -7.0 eV which give rise to a participator Auger decay at the Co^{2+} (s= 3/2) HS states.

The third contribution is found at lower initial state energy of -4.3 eV. There is only a weak shoulder within a rather small excitation energy range between 777 eV and 780 eV. It is attributed to a metal-to-ligand charge transfer state, in which an electron originating from an O2p valence state (ligand) is transferred to an empty metal state. The CT states are characterized by the weak resonances at 780 eV and also by their corresponding features in the O1s resPES profile as discussed below.

The resPES data indicate that the shoulder at -4 eV is also a HS state (s= 1) because it again appears as a participator decay. For the Co-PI Co^{2+} system this will be a HS (s= 1) $3d^8L$ state which is assigned to the initial state of -4 eV.

In the corresponding data of Cat-D (Figure 3.31b, lower panel) the two main bands with their dominating participator contributions are still present, now they are shifted to -6.0 eV and -10.5 eV, indicating the presence of HS configurations. These must be attributed to the content of Co^{2+} ($3d^7$ HS) in that film.

Beside this shift of the two initial states of about 1 eV two new features are observed, in addition. First, there is an increased amount of a spectator Auger decay (LS) clearly visible with a kinetic energy of E_{kin}= 775 eV as indicated by the black dashed arrow (Figure 3.31b). It is only pronounced for Cat-D and is due to a spectator Auger decay that can be attributed to the Co^{3+} content. This indicates that the Co^{3+} relative content belongs to the LS $3d^6$ (s= 0) state to facilitate the spectator Auger decay out of the filled 3d levels. The intensity of this Auger process gives an estimate on the relative content of the Co^{3+} states, which amounts to about 10 % for Cat-A and 30 % for Cat-D. The Auger intensity was calculated by subtracting an off-resonant VB spectrum (772 eV) from the Co^{2+} (transition 3) and Co^{3+} (transition 6) resonances and normalizing all spectra to the Co^{2+} resonance (transition 3). These values are in agreement with the amount of Co^{3+} content which were also independently deduced from the intensity of the satellite structure of the Co2p core level (Figure 4.10b).

The second new feature arises at the initial state energy of -1.8 eV very close to the Fermi energy. This feature is very sharp, as it appears only around a excitation energy of 780.6 eV. It is characteristic only in the Co-PI samples prepared under high amperometric load. In fact, the CIS profile at this initial state of -1.8 eV has a FANO line shape (Figure 3.32). The FANO profile results from an interference of two photoemission channels. One is the direct emission channel; the second one is indirect as the emitted electron rests for a fraction of attoseconds within a completely empty level in the 3d orbitals until the emission process is continued. For enabling a FANO profile empty 3d states must be available. Such possible configurations could be either a LS $3d^6$ (s= 0) and/or LS $3d^7L$ (s= 1/2). The accompanying CT transitions are observed at the corresponding O1s resonance (Figure 3.33b). As at the Co L_3 edge both, the spectator Auger decay (E_{kin}= 775 eV) and the FANO profile are evident, it can be concluded that the Co^{3+} ($3d^7L$) LS configuration contributes.

Charge transfer states (from O2p to Co3d) can be distinguished from the other states in the resPES spectrum by their fingerprint in the Auger decay (S+P) at the O1s edge.

Under resonant excitation the Auger decay at the O1s edge close to the Fermi energy ($E_F \triangleq 531$ eV) $3h_{(1)}$ and close to the CBM $3h_{(2)}$ deviates from the normal two-hole spectator decay at higher excitation energies (Figure 3.33).

For the Co-PI catalyst the two (S+P) decays are assigned to arise from CT states. The one at 530 eV ($3h_{(1)}$) is solely associated to the ($3d^7L$) CT state for the Co^{3+} species as its intensity increases with the amount of incorporated Co^{3+} (Figure 3.30b). The other one at 537 eV ($3h_{(2)}$) is associated to the ($3d^8L$) CT state of the Co^{2+} species.

Cat-A with >90 % Co^{2+} (Figure 3.33a) shows only evidence for a single (S+P) decay (charge transfer state) at the CBM ($3h_{(2)}$) whereas Cat-D (Figure 3.33b) with >20 % Co^{3+} shows an additional separate (S+P) Auger decay at the Fermi energy ($3h_{(1)}$). Because of the localized nature of the trapped state in the CT state these two resonances appear with a reduced spectral width.

As for the Co^{2+} $3d^8L$ CT state no FANO transition and no spectator decay are observed at the Co L_3 edge it is in a HS state. Only the Co^{3+} $3d^7L$ CT state is in a LS state to facilitate the FANO resonance.

The identification of the two CT bands by the (S+P) Auger decay demonstrates the existence small Polarons in the band gap. This has to be taken into account for proposing a band scheme and deducing the electronic band gap for Co-PI.

4.3.4 Band scheme

Because of the (S+P) Auger decay an underestimated CBM is found at lower values close to the Fermi energy. Here a low intensity band tail from the (S+P) Auger decay is starting at the Fermi energy. The (S+P) Auger decay in Co-PI is an evidence of an oxygen to metal charge transfer state. Lattice distortion is localizing the O2p hole. This self-trapped hole can trap the resonantly excited core electron and from a self-trapped Exciton. STHs and STXs are in-gap states, which have to be considered in the band scheme.

From the combination of core level, valence band, XAS, resPES and partial density of states measurements the band diagram of the Co-PI catalyst layers can be constructed (Figure 4.12).

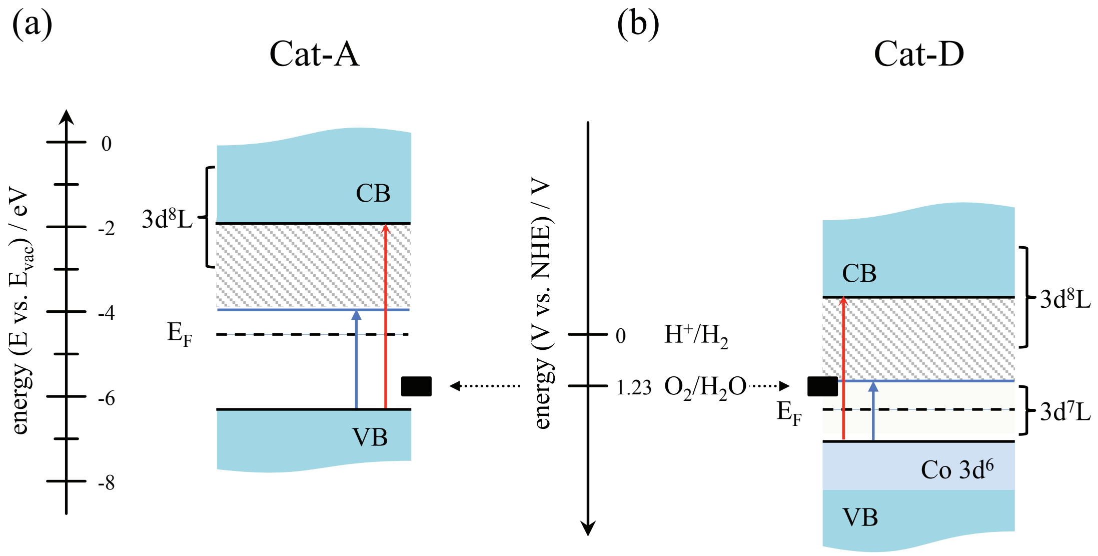

Figure 4.12: *Schematic band diagram of (a) the surface Co-PI catalyst with a mean oxidation state of* Co^{2+} *(Cat-A) and of (b) bulk Co-PI catalyst with an oxidation state mixture of* Co^{2+} *and* Co^{3+} *(Cat-D). The red arrows indicate the band gap without taking into account the (S+P) Auger* ($3d^8L$) *(electronic band gap: 4.4 eV for Cat-A and 3.4 eV for Cat-D) and the blue arrows the band gap with consideration of the FWHM of the (S+P) Auger* ($3d^8L$) *(optical band gap): 2.4 eV for Cat-A (a) and 1.4 eV for Cat-D (b). The work functions for CoO (Cat-A) of 4.6 eV and for* Co_3O_4 *(Cat-D) of 6.3 eV were taken from [GRE12]. The approximate position of the* $E^0(O_2/H_2O)$ *potential is indicated by black boxes.*

The $3d^8L$ state of Co^{2+} gives rise to an (S+P) Auger decay at the conduction band minimum. Due to the increase of the cobalt valency both $3d^8L$ CT and $3d^7L$ CT states are observed for Cat-D. The latter give rise to a second (S+P) Auger decay at the Fermi energy.

Accurately, the position of the real CBM is given by the starting point of the normal spectator Auger decay (two-hole final state), which can be determined by the rising edge of the main resonance at 538 eV in the oxygen XAS spectrum (Figure 3.30b).

With a CBM value of 534.2 eV for Cat-A, 533.6 eV for Cat-D, the corresponding binding energy of the O1s core level as the reference position for E_F, and the VBM (Table 3.8) the band gap E_{gap} for the surface Co-PI catalyst (Cat-A) is 4.4±0.2 eV and 3.4±0.2 eV for the bulk Co-PI catalyst (Cat-D) (Figure 4.12, red arrow). The difference in the band gap between surface and bulk can be ascribed to the increase in Co valency from Co^{2+} to Co^{3+}.

CoO (Co^{2+}) and Co_3O_4 (Co^{2+} and Co^{3+}) have a band gap of 2.2 – 2.8 eV and 1.4 – 1.8 eV, respectively [WOL03]. These values are around 1.5 eV smaller than the values reported herein. This discrepancy can be explained by taking into account the FWHM of the $3d^8L$ CT state, which is around 2 eV. The smaller band gaps obtained from this lower CBM by considering the FWHM of the (S+P) decay are then comparable to the reported band gap values of CoO and Co_3O_4 (Figure 4.12, blue arrow).

Under consideration of the these band gaps the Cat-A Co^{2+} layer would be more n-type and the Cat-D Co^{3+} layer would be intrinsic (slight p-type). Surface and bulk Co-PI in contact could then be considered as a pn-junction. A utilization for improved solar-to-hydrogen efficiency is conceivable.

Taking into account the $E^0(O_2/H_2O)$ level for OER relative to the vacuum level (-4.5 eV-1.23 eV= -5.73 eV [BAK02]) and a general work function for CoO of about 4.6 eV and about 6.3 eV for Co_3O_4 [GRE12] the $E^0(O_2/H_2O)$ level is found to be about 0.7 eV above the VBM for Cat-A and about 1.4 eV above the VBM for Cat-D. Hence, in case of Cat-D the $E^0(O_2/H_2O)$ level is in the Co^{3+} $3d^7L$ CT band with a LS configuration of (s= 1/2) for Cat-D (compare to Figure 4.12). Only the $3d^7L$ (s= 1/2) CT of Co^{3+} at E_F will therefore contribute via polarization to a reduced overpotential in the OER.

Therefore this $3d^7L$ (s= 1/2) CT state is considered to be most important for the catalysts activity.

Finally it has to be noted that the intensity of the (S+P) Auger decay at 530 eV at the O1s edge is still rather weak. As it is a measure for cobalt atoms with a $3d^7L$ configuration an even better performance is expected if the intensity of these states could be increased by optimizing the preparation parameters.

4.3.5 Conclusion - Co-PI

Co-PI catalysts were successful deposited on oxidized Nickel substrates using electrochemical deposition from Co^{2+} containing potassium-phosphate electrolyte.

By performing resPES and core level PES on Co-PI a HS Co^{2+} state $3d^7$ (s= 3/2) and a $3d^8L$ CT state (s= 1) is found for the initial thin layers with a low deposited charge concentration (0.26 C/cm^2). The spin state of Co and its CT states (special class of Polaron and exciton states in TM-oxides) could be identified by resPES using systematic findings in the resonant Auger decay process.

Depending on the deposited amount of Co-PI catalyst (charge density) a change in band gap, a shift of the Fermi energy and an increase of the cobalt oxidation state is found. The evolution of the Co2p core level and XAS spectra for higher amounts of deposited Co-PI catalyst (4.5 C/cm^2) suggests that for high deposited charge concentrations the Co^{2+} Co-PI gets a reasonable amount of Co^{3+} admixture. A high deposited charge concentration (Cat-D) has additional LS Co^{3+} states $3d^6$ (s= 0) and a $3d^7L$ CT state (s= 1/2).

From atomic concentration of the elements (Co, O, K, and P), determined by XPS, of both surface and bulk Co-PI the edge sharing molecular cobaltate structure is favoured. Bulk (high deposited charge concentration of 4.5 C/cm^2) Co-PI has higher surface-volume ratio with decreased particle size beneficial for catalysis.

These results are important in order to comprehend the successful catalysation of the oxidation reaction of water by these cobalt-based catalysts and their good stability as reported by Nocera et al. [ESS11], [REE11], [SUR09]. For the catalysis of the water oxidation a high surface area is necessary. In the oxidation cycle – KOK's basic reaction cycle [KOK70] – four oxidizing equivalents have to be stored by oxidizing the metal complex (Co), which is facilitated by the ligand charge transfer states as observed in the thick Co-PI films (Co^{3+} $3d^7L$).

The proposed pathway for the OER of the Co-PI catalyst involves a Co^{3+}/Co^{4+} redox reaction with a four electron transfer and a Co^{2+} final state after the desorption of O_2 (Figure 1.10) [SUR10]. For the catalytic activity – i.e. the oxygen reduction and OER – in the Co-PI catalysts the oxidation state of cobalt should be equal or greater than Co^{2+} [CAL11], [MCA10], [MCA11]. Insofar, the ability of the Co-PI catalyst to have both, the divalent and the trivalent oxidation state is of importance. The (s= 1/2) LS state of Co^{3+} on the other hand should be beneficial during the water adsorption and oxidation reaction. The HS Co^{2+} state facilitates desorption of oxygen because the back-reaction is spin-forbidden [BUC96], [MIN10], [ZHU13].

For Cobalt-oxide the existence of two multiple hole Auger decays at the O1s edge, here a combined (S+P) decay as evident by a slope of 67.5° in the corresponding resPES diagram (Figure 3.33), could identify two CT bands (small Polarons): $3d^8L$ and $3d^7L$. Here the Co^{3+} LS (s= 1/2) $3d^7L$ is considered to most significant for the OER reaction as the $E^0(O_2/H_2O)$ potential is located in this charge transfer band which can store the four oxidizing equivalents needed in the oxidation cycle.

Chapter 5 Conclusion and Outlook

The main topic of this thesis is to identify localized states within the band gap of organic semiconductors, of Graphene systems, and of transition metal oxide water splitting catalysts (Co-PI).
Therefor the experimental available method of resPES was systematically applied.
It has been possible to identify Excitons, Polarons, and CT states. The localized states cause the appearance of multiple Auger processes right at the core level absorption resonance. For each of the new combination of multiple Auger decays models have been developed and established to identify the +3h (S+P), +4h (S+S), and -4h (S+S)* Auger processes.
Besides these localization effects causing defect states in the band gap, an analysis of the spin state could also be demonstrated by using resPES.

Reviewing the results of the three different material classes:

Firstly, the organic semiconductors rr-P3HT and PCBM, as used for organic solar cells, exhibit a strong singlet excitonic transition just below the CBM in the C1s resPES profile. The singlet Exciton gives rise to a combined spectator-participator (S+P) Auger decay in the π^*-band. In contrast, for rr-P3HT, 2D-Polarons and triplet Excitons do not exhibit any Auger decay. The binding energy of these Polarons and triplet Excitons is too high to have a significant overlap with the CB. Only for singlet Excitons the binding energy is in the same order as the one of its FWHM. Hence, singlet Excitons can act as localized traps for resonantly excited electrons and enable the core hole to decay, via a combined (S+P) Auger decay which happens only in the π^*-band.

Secondly, Graphene systems exhibit likewise a strong excitonic resonance in the C1s resPES profile. Here the Exciton is accompanied by a FANO transition, which is used as a fingerprint for the existence of singlet Excitons. The singlet Excitons have a suitable lifetime and overlap with the CB. Interlayer interaction (van der Waals force for HOPG), substrate interaction, and screening (i.e. monolayer Graphene on metal substrates) modify the properties of the Exciton. In monolayer Graphene no interlayer interaction is present and the lifetime of the singlet Exciton is slightly reduced.

As a result an (S+P) Auger decay is observed only for interlayer interaction (HOPG and multilayer Graphene). For monolayer Graphene the singlet Excitons give rise to a combination of a double spectator Auger decay (S+S) and a double spectator Auger-Gain decay (S+S)*. Both, the (S+S) and (S+S)* decay, are considered to be characteristic for free-standing monolayer Graphene. The scattering time of the spectator Auger electrons with the singlet Exciton is also another parameter responsible for the decay via an (S+P) or (S+S) Auger process. An upper limit for the scattering time is the lifetime of the Exciton with about 0.5 fs deduced for Graphene.

Screening by the substrate and hybridization of the carbon π-system with substrate valence band states diminish the Auger decay in the Graphene π-system. Instead, a characteristic pre-edge resonance indicates a substrate-Graphene hybridization.

Thirdly, the multiple Auger combination models can also be applied on TM-oxides. Because of a charge transfer from oxygen to metal VB states and delocalization of the oxygen hole states by lattice distortion localized self-trapped holes exist in TM-oxides. A resonantly excited core electron can get trapped in these STHs out of which a self-trapped Exciton is formed. These STXs are identified by their (S+P) Auger decay in the O1s resPES profile.

Co-PI as a TM-oxide and catalyst for the oxygen evolution reaction in photo-electrochemical cells was investigated under this aspect. In this case two STH states (CT bands) could be identified. The Co^{3+} $3d^7L$ and Co^{2+} $3d^8L$ CT states are found as in-gap states reducing the electronic band gap by about 2 eV. Only the Co^{3+} $3d^7L$ STH state is found at the $E^0(O_2/H_2O)$ redox potential and is relevant for the water splitting catalysis.

Especially by using systematic findings of the resonant Auger decay process, the spin state of cobalt and its charge transfer state was identified by the analysis of the Auger decay profile at the Co2p and O1s edge.

Summarizing, resonant photoemission at the core level threshold provides a powerful tool to learn about the existence of localized in-gap states – Polarons and Excitons – and the spin state of the particular material by the analysis of the combined Auger decay processes at resonance. In our group this technique has been applied to characterize single crystal oxides, to distinguish between optical and electronic band gap, or to explain resistive switching devices.

References

[ALZ09] A.Z. AlZahrani, G.P. Srivastava, "*Graphene to graphite: electronic changes within DFT calculations.*", Braz. J. Phys. 39 (2009) 694–698.

[ANT06] T.D. Anthopoulos, B. Singh, N. Marjanovic, N.S. Sariciftci, A.M. Ramil, H. Sitter, M. Colle, D.M. de Leeuw, *"High performance n-channel organic field-effect transistors and ring oscillators based on C_{60} fullerene films."*, Appl. Phys. Lett. 89 (2006) 213504.

[ARY12] K. Aryanpour, S. Mazumdar, H. Zhao, *"Triplet Excitations in Carbon Nanostructures."*, Phys. Rev. B 85 (2012) 085438.

[BAE90] P. Bätz, D. Schmeiβer, W. Gopel, *"Polaron-induced metallic polypyrrole."*, Solid State Commun. 74 (1990) 461–464.

[BAK02] T. Bak, J. Nowotny, M. Rekas, C.C. Sorrell, *"Photo-electrochemical hydrogen generation from water using solar energy Materials-related aspects."*, Int. J. Hydrogen Energ. 27 (2002) 991–1022.

[BAT12] M. Batzill, *"The surface science of graphene: Metal interfaces, CVD synthesis, nanoribbons, chemical modifications, and defects."*, Surf. Sci. Rep. 67 (2012) 83–115.

[BEL01] D. Beljonne, J. Cornil, H. Sirringhaus, P. Brown, M. Shkunov, R. Friend, J. Bredas, *"Optical signature of delocalized polarons in conjugated polymers."*, Adv. Funct. Mater. 11 (2001) 229–234.

[BRA81] S.A. Brazovskii, N.N. Kirova, *"Excitons, polarons, and bipolarons in conducting polymers."*, JETP Lett. 33 (1981) 4–8.

[BRE85] J.L. Bredas, G.B. Street, *"Polarons, Bipolarons, and Solitons in conducting polymers.",* Acc. Chem. Res. 18 (1985) 309–315.

[BRE87] J.L. Bredas, F. Wudl, A. Heeger, *"Polarons and Bipolarons in doped polythiophene - a theoretical investigation."*, Solid State Commun. 63 (1987) 577–580.

[BRO10] K. Broczkowska, J. Klocek, D. Friedrich, K. Henkel, K. Kolanek, A. Urbanowicz, D. Schmeißer, M. Miller, E. Zschech, *"Fullerene based materials for ultra-Iow-k application."*, 2010 International Students and Young Scientists Workshop "Photonics and Microsystems" (2010) 39–43.

[BRU95] P.A. Brühwiler, A. Maxwell, C. Puglia, A. Nilsson, S. Andersson, N. Mårtensson, *"π* and σ* Excitons in C 1s Absorption of Graphite."*, Phys. Rev. Lett. 74 (1995) 614–617.

[BRU02] P.A. Brühwiler, O. Karis, N. Mårtensson, *"Charge-transfer dynamics studied using resonant core spectroscopies."*, Rev. Mod. Phys. 74 (2002) 703–740.

[BRU08] W. Brutting, W. Riess, *"Grundlagen der organischen Halbleiter."*, Physik Journal 7 (2008) 33–38.

[BUC96] A.L. Buchachenko, V.L. Berdinsky, *"Spin Catalysis of Chemical Reactions."*, J. Phys. Chem. 100 (1996) 18292–18299.

[BUC04] A.L. Buchachenko, V.L. Berdinsky, *"Spin catalysis as a new type of catalysis in chemistry."*, Russ. Chem. Rev. 73 (2004) 1033–1039.

[BUR06] T. Burnus, Z. Hu, M. Haverkort, J. Cezar, D. Flahaut, V. Hardy, A. Maignan, N. Brookes, A. Tanaka, H. Hsieh, H.J. Lin, C. Chen, L. Tjeng, *"Valence, spin, and orbital state of Co ions in one-dimensional $Ca_3Co_2O_6$: An X-ray absorption and magnetic circular dichroism study."*, Phys. Rev. B 74 (2006) 245111.

[CAL11] F. Calle-Vallejo, J.I. Martínez, J. Rossmeisl, *"Density functional studies of functionalized graphitic materials with late transition metals for oxygen reduction reactions."*, Phys. Chem. Chem. Phys. 13 (2011) 15639–15643.

[CAR95] J.A. Carlisle, E.L. Shirley, E. Hudson, L.J. Terminello, T.A. Callcott, J.J. Jia, D.L. Ederer, R.C.C. Perera, F.J. Himpsel, *"Probing the graphite band-structure with resonant soft-X-ray fluorescence."*, Phys. Rev. Lett. 74 (1995) 1234–1237.

[CAR99] J.A. Carlisle, E.L. Shirley, L.J. Terminello, J.J. Jia, T.A. Callcott, D.L. Ederer, R.C.C. Perera, F.J. Himpsel, *"Band-structure and core-hole effects in resonant inelastic soft-x-ray scattering: Experiment and theory."*, Phys. Rev. B 59 (1999) 7433–7445.

[CAR00] J.A. Carlisle, S.R. Blankenship, L.J. Terminello, J.J. Jia, T.A. Callcott, D.L. Ederer, R.C.C. Perera, F.J. Himpsel, *"Crystal-momentum-resolved electronic structure of solids using resonant soft-X-ray fluorescence spectroscopy."*, J. Electron. Spectrosc. 110-111 (2000) 323–334.

[CAS09] A.H. Castro Neto, N.M.R. Peres, K.S. Novoselov, A.K. Geim, *"The electronic properties of graphene."*, Rev. Mod. Phys. 81 (2009) 109–162.

[CHA11] D.-H. Chae, T. Utikal, S. Weisenburger, H. Giessen, K.V. Klitzing, M. Lippitz, J. Smet, *"Excitonic Fano Resonance in Free-Standing Graphene."*, Nano Lett. 11 (2011) 1379–1382.

[CHI77] C. Chiang, C. Fincher, Y. Park, A. Heeger, H. Shirakawa, E. Louis, S. Gau, A. MacDiarmid, *"Electrical Conductivity in Doped Polyacetylene."*, Phys. Rev. Lett. 39 (1977) 1098–1101.

[CHI10] G. Chidichimo, L. Filippelli, *"Organic Solar Cells: Problems and Perspectives."*, Int. J. Photoenergy 2010 (2010) 123534.

[CHO12] M. Chowdhury, R. Saito, M. Dresselhaus, *"Polarization dependence of x-ray absorption spectra in graphene."*, Phys. Rev. B 85 (2012) 115410.

[CLE01] B. Cleff, W. Mehlhorn, *"On the angular distribution of Auger electrons following impact ionization."*, J. Phys. B: at. Mol. Phys. 7 (2001) 593–604.

[COS35] D. Coster, R. Kronig, *"A new type of Auger effect and its influence on the x-ray spectrum."*, Physica 2 (1935) 13–24.

[COW00] D. Coward, S. Thurgate, "Post collision interaction in the L_3-$M_{4,5}M_{4,5}$ Auger spectra in solid state copper.", J. Electron Spectrosc. 107 (2000) 193–199.

[CSI05] S. Csiszar, M. Haverkort, Z. Hu, A. Tanaka, H. Hsieh, H.J. Lin, C. Chen, T. Hibma, L. Tjeng, *"Controlling Orbital Moment and Spin Orientation in CoO Layers by Strain."*, Phys. Rev. Lett. 95 (2005) 187205.

[CUD10] P. Cudazzo, C. Attaccalite, I.V. Tokatly, A. Rubio, *"Strong Charge-Transfer Excitonic Effects and the Bose-Einstein Exciton Condensate in Graphane."*, Phys. Rev. Lett. 104 (2010) 226804.

[DAN93] P. Dannetun, M. Boman, S. Stafstrom, W. Salaneck, R. Lazzaroni, C. Fredriksson, J. Bredas, R. Zamboni, C. Taliani, *"The chemical and electronic-structure of the interface between aluminum and polythiophene semiconductors."*, J. Chem. Phys. 99 (1993) 664–672.

[DEI10] C. Deibel, D. Mack, J. Gorenflot, A. Schoell, S. Krause, F. Reinert, D. Rauh, V. Dyakonov, *"Energetics of excited states in the conjugated polymer poly(3-hexylthiophene)."*, Phys. Rev. B 81 (2010) 085202.

[DEN09] G. Dennler, M.C. Scharber, C.J. Brabec, *"Polymer-Fullerene Bulk-Heterojunction Solar Cells."*, Adv. Mater. 21 (2009) 1323–1338.

[ESS11] A.J. Esswein, Y. Surendranath, S.Y. Reece, D.G. Nocera, *"Highly active cobalt phosphate and borate based oxygen evolving catalysts operating in neutral and natural waters."*, Energ. Environ. Sci. 4 (2011) 499–504.

[FAN66] U. Fano, *"Effects of Configuration Interaction on Intensities and Phase Shifts."*, Phys. Rev. 124 (1961) 1866–1878.

[FAN11] M. Fang, Z. Tang, H. Lu, S. Nutt, *"Multifunctional superhydrophobic composite films from a synergistic self-organization process."*, J. Mater. Chem. 22 (2011) 109–114.

[FEL09] M.P. Felicissimo, D. Jarzab, M. Gorgoi, M. Forster, U. Scherf, M.C. Scharber, S. Svensson, P. Rudolf, M.A. Loi, *"Determination of vertical phase separation in a polyfluorene copolymer: fullerene derivative solar cell blend by X-ray photoelectron spectroscopy."*, J. Mater. Chem. 19 (2009) 4899–4901.

[FEN07] D.-Q. Feng, A.N. Caruso, Y.B. Losovyj, D.L. Shulz, P.A. Dowben, *"Identification of the possible in poly(3-hexylthiophene) thin defect states films."*, Polym. Eng. Sci. 47 (2007) 1359–1364.

[FOE02] A. Föhlisch, O. Karis, M. Weinelt, J. Hasselstrom, A. Nilsson, N. Mårtensson, *"Auger resonant Raman scattering in itinerant electron systems: Continuum excitation in Cu."*, Phys. Rev. Lett. 88 (2002) 027601.

[FOE06] A. Föhlisch, *"Ultrafast charge transfer and nuclear dynamics studied with resonant X-ray spectroscopy."*, Appl. Phys. A, 85 (2006) 351–359.

[FOL01] R. Follath, *"The versatility of collimated plane grating monochromators."*, Nucl. Instrum. Methods Phys. Res. A 467-468 (2001) 418–425.

[FUJ90] H. Fujimoto, U. Nagashima, H. Inokuchi, K. Seki, Y. Cao, H. Nakahara, J. Nakayama, M. Hoshino, K. Fukuda, *"Ultraviolet photoemission-study of oligothiophenes: π-band evolution and geometries."*, J. Chem. Phys. 92 (1990) 4077–4092.

[GAR11] M. García-Mota, A. Vojvodic, H. Metiu, I.C. Man, H.-Y. Su, J. Rossmeisl, J.K. Nørskov, *"Tailoring the Activity for Oxygen Evolution Electrocatalysis on Rutile* $TiO_2(110)$ *by Transition-Metal Substitution."*, ChemCatChem 3 (2011) 1607–1611.

[GEI07] A.K. Geim, K.S. Novoselov, *"The rise of graphene."*, Nat. Mater. 6 (2007) 183–191.

[GEI11] A.K. Geim, *"Nobel Lecture: Random walk to graphene."*, Rev. Mod. Phys. 83 (2011) 851–862.

[GEI12] A.K. Geim, *"Graphene prehistory."*, Phys. Scripta T146 (2012) 014003.

[GER09] D.S. Germack, C.K. Chan, B.H. Hamadani, L.J. Richter, D.A. Fischer, D.J. Gundlach,D.M. DeLongchamp, *"Substrate-dependent interface composition and charge transport in films for organic photovoltaics."*, Appl. Phys. Lett. 94 (2009) 233303.

[GHI96] J. Ghijsen, R. Lazzaroni, V. Parente, J. Bredas, A. Lachkar, A. Selmani, R. Johnson, *"Photoemission study of copper deposition on the conjugated polymer poly-3-hexylthiophene and comparison with quantum-chemical calculations."*, J. Electron Spectrosc. 78 (1996) 355–358.

[GIO07] G. Giovannetti, P. Khomyakov, G. Brocks, P. Kelly, J. van den Brink, *“Substrate-induced band gap in graphene on hexagonal boron nitride: Ab initio density functional calculations.”*, Phys. Rev. B 76 (2007) 073103.

[GLA09] P. Glatzel, M. Sikora, M. Fernandez-Garcia, *“Resonant X-ray spectroscopy to study K absorption pre-edges in 3d transition metal compounds.”*, Eur. Phys. J.-Spec. Top. 169 (2009) 207–214.

[GRE12] M.T. Greiner, L. Chai, M.G. Helander, W.-M. Tang, Z.-H. Lu, *“Transition Metal Oxide Work Functions: The Influence of Cation Oxidation State and Oxygen Vacancies.”*, Adv. Funct. Mater. 22 (2012) 4557–4568.

[GUO09] J. Guo, H. Ohkita, H. Benten, S. Ito, *“Near-IR Femtosecond Transient Absorption Spectroscopy of Ultrafast Polaron and Triplet Exciton Formation in Polythiophene Films with Different Regioregularities.”*, J. Am. Chem. Soc. 131 (2009) 16869–16880.

[HAV06] M. Haverkort, Z. Hu, J. Cezar, T. Burnus, H. Hartmann, M. Reuther, C. Zobel, T. Lorenz, A. Tanaka, N. Brookes, H. Hsieh, H.J. Lin, C. Chen, L. Tjeng, *“Spin State Transition in* $LaCoO_3$ *Studied Using Soft X-ray Absorption Spectroscopy and Magnetic Circular Dichroism.”*, Phys. Rev. Lett. 97 (2006) 176405.

[HEE88] A.J. Heeger, J.R. Schrieffer, W.P. Su, *“Solitons in conducting polymers.”*, Rev. Mod. Phys. 60 (1988) 781–850.

[HEE01] A.J. Heeger, *“Nobel Lecture: Semiconducting and metallic polymers: The fourth generation of polymeric materials.”*, Rev. Mod. Phys. 73 (2001) 681–700.

[HOR02] J. van der Horst, P. Bobbert, W. Pasveer, M. Michels, G. Brocks, P. Kelly, *“Excitons in conjugated polymers from first principles.”*, Comp. Phys. Commun. 147 (2002) 331–334.

[HU04] Z. Hu, H. Wu, M. Haverkort, H. Hsieh, H. Lin, T. Lorenz, J. Baier, A. Reichl, I. Bonn, C. Felser, A. Tanaka, C. Chen, L. Tjeng, *“Different Look at the Spin State of* Co^{3+} *Ions in a* CoO_5 *Pyramidal Coordination.”*, Phys. Rev. Lett. 92 (2004) 207402.

[HUE03] S. Hüfner, *“Photoelectron spectroscopy.”*, Springer Verlag, 2003.

[IWA11] T. Iwasaki, H.J. Park, M. Konuma, D.S. Lee, J.H. Smet, U. Starke, *“Long-Range Ordered Single-Crystal Graphene on High-Quality Heteroepitaxial Ni Thin Films Grown on MgO(111).”*, Nano Lett. 11 (2011) 79–84.

[JAN06] C. Janowitz, V. Scherer, M. Mohamed, A. Krapf, H. Dwelk, R. Manzke, Z. Galazka, R. Uecker, K. Irmscher, R. Fornari, M. Michling, D. Schmeißer, J.R. Weber, J.B. Varley, C.G.V. de Walle, *“Experimental electronic structure of* In_2O_3 *and* Ga_2O_3*.”*, New J. Phys. 13 (2011) 085014.

[JAN10] A. Janotti, J.B. Varley, P. Rinke, N. Umezawa, G. Kresse, C.G. Van de Walle, *“Hybrid functional studies of the oxygen vacancy in* TiO_2*.”*, Phys. Rev. B 81 (2010) 085212.

[JIA02] X. Jiang, R. Osterbacka, O. Korovyanko, C. An, B. Horovitz, R. Janssen, Z. Vardeny, *“Spectroscopic studies of photoexcitations in regioregular and regiorandom polythiophene films.”*, Adv. Funct. Mater. 12 (2002) 587–597.

[JOS09] S. Joshi, P. Pingel, S. Grigorian, T. Panzner, U. Pietsch, D. Neher, M. Forster, U. Scherf, *“Bimodal Temperature Behavior of Structure and Mobility in High Molecular Weight P3HT Thin Films.”*, Macromolecules 42 (2009) 4651–4660.

[KAM08] N. Kameda, S. Nakabayashi, *“Shape Dynamics of Nanobubbles Located on Bunched and Wide Terraces at Highly Oriented Pyrolytic Graphite/Water–Ethanol Interface.”*, Jpn. J. Appl. Phys. 47 (2008) 1065–1067.

[KAN08a] M.W. Kanan, D.G. Nocera, *"In situ formation of an oxygen-evolving catalyst in neutral water containing phosphate and* Co^{2+}*."*, Science 321 (2008) 1072–1075.

[KAN08b] M.W. Kanan, Y. Surendranath, D.G. Nocera, *"Cobalt–phosphate oxygen-evolving compound."*, Chem. Soc. Rev. 38 (2008) 109–114.

[KAN10] M.W. Kanan, J. Yano, Y. Surendranath, M. Dincă, V.K. Yachandra, D.G. Nocera, *"Structure and Valency of a Cobalt−Phosphate Water Oxidation Catalyst Determined by in Situ X-ray Spectroscopy."*, J. Am. Chem. Soc. 132 (2010) 13692–13701.

[KAR03] N. Karl, *"Charge carrier transport in organic semiconductors."*, Synth. Met. 133 (2003) 649–657.

[KAR11] P.G. Karagiannidis, S. Kassavetis, C. Pitsalidis, S. Logothetidis, *"Thermal annealing effect on the nanomechanical properties and structure of P3HT:PCBM thin films."*, Thin Solid Films 519 (2011) 4105–4109.

[KEA90] M.P. Keane, S. Svensson, A. Naves De Brito, N. Correia, S. Lunell, B. Sjögren, O. Inganäs, W. Salaneck, *"Gas-phase x-ray photoelectron spectroscopy of model molecules relating to the thermochromism in poly(3-alkylthiophene)."*, J. Chem. Phys. 93 (1990) 6357–6362.

[KIM03] J.-Y. Kim, J.H. Park, B.G. Park, H.J. Noh, S.J. Oh, J. Yang, D.H. Kim, S. Bu, T.W. Noh, H.J. Lin, H.H. Hsieh, C. Chen, *"Ferromagnetism Induced by Clustered Co in Co-Doped Anatase* TiO_2 *Thin Films."*, Phys. Rev. Lett. 90 (2003) 017401.

[KLO12a] J. Klocek, K. Henkel, K. Kolanek, E. Zschech, D. Schmeißer, Spectroscopic and capacitance–voltage characterization of thin aminopropylmethoxysilane films doped with copper phthalocyanine, tris(dimethylvinylsilyloxy)–POSS and fullerene cages, Appl. Surf. Sci, 258 (2012) 4213–4221.

[KLO12b] J. Klocek, K. Henkel, K. Kolanek, K. Broczkowska, D. Schmeißer, M. Miller, E. Zschech, *"Studies of the chemical and electrical properties of fullerene and 3-aminopropyltrimethoxysilane based low-k materials."*, Thin Solid Films 520 (2012) 2498–2504.

[KOE09] A. Köhler, H. Bässler, *"Triplet states in organic semiconductors."*, Mat. Sci. Eng. R 66 (2009) 71–109.

[KOK70] B. Kok, B. Forbush, M. McGloin, *"Cooperation of charges in photosynthetic* O_2 *evolution–I. A linear four step mechanism."*, Photochem. Photobiol. 11 (1970) 457–475.

[KOL06] C. Kolczewski, R. Puttner, M. Martins, A.S. Schlachter, G. Snell, M.M. Sant'Anna, K. Hermann, G. Kaindl, *"Spectroscopic analysis of small organic molecules: A comprehensive near-edge x-ray-absorption fine-structure study of* C_6*-ring-containing molecules"*, J. Chem. Phys. 124 (2006) 034302.

[KOO34] T. Koopmans, *"Über die Zuordnung von Wellenfunktionen und Eigenwerten zu den Einzelnen Elektronen Eines Atoms."*, Physica 1 (1934) 104–113.

[KOS06] L. Koster, V. Mihailetchi, P. Blom, *"Ultimate efficiency of polymer/fullerene bulk heterojunction solar cells."*, Appl. Phys. Lett. 88 (2006) 093511.

[KRA79a] M.O. Krause, *"Atomic radiative and radiationless yields for K and L shells."*, J. Phys. Chem. Ref. Data 8 (1979) 307–327.

[KRA79b] M.O. Krause, J.H. Oliver, *"Natural widths of atomic K and L levels, Kα X-ray lines and several KLL Auger lines."*, J. Phys. Chem. Ref. Data 8 (1979) 329.

[KWO12] K.C. Kwon, K.S. Choi, S.Y. Kim, *"Increased Work Function in Few-Layer Graphene Sheets via Metal Chloride Doping."*, Adv. Funct. Mater. 22 (2012) 4724–4731.

[LIA11] Y. Liang, S. Huang, L. Yang, *“Many-electron effects on optical absorption spectra of strained graphene.”*, J. Mater. Res. 27 (2011) 403–409.

[LOP91] G. Lopez, D. Castner, B. Ratner, *“XPS O1s Binding-Energies for Polymers Containing Hydroxyl, Ether, Ketone and Ester Groups.”*, Surf. Interface Anal. 17 (1991) 267–272.

[LUI11] C.H. Lui, Z. Li, K.F. Mak, E. Cappelluti, T.F. Heinz, *“Observation of an electrically tunable band gap in trilayer graphene.”*, Nat. Phys. 7 (2011) 944–947.

[MA99] Q. Ma, R. Rosenberg, *“Core and valence level characterization of the interfacial reaction between partially oxidized Ti films and graphite.”*, Appl. Surf. Sci. 140 (1999) 83–89.

[MA05] W. Ma, C. Yang, X. Gong, K. Lee, A. Heeger, *“Thermally stable, efficient polymer solar cells with nanoscale control of the interpenetrating network morphology.”*, Adv. Funct. Mater. 15 (2005) 1617–1622.

[MAK11] K.F. Mak, J. Shan, T. Heinz, *“Seeing Many-Body Effects in Single- and Few-Layer Graphene: Observation of Two-Dimensional Saddle-Point Excitons.”*, Phys. Rev. Lett. 106 (2011) 046401.

[MCA10] J.G. McAlpin, Y. Surendranath, M. Dincă, T.A. Stich, S.A. Stoian, W.H. Casey, D.G. Nocera, R.D. Britt, *“EPR Evidence for Co(IV) Species Produced During Water Oxidation at Neutral pH.”*, J. Am. Chem. Soc. 132 (2010) 6882–6883.

[MCA11] J.G. McAlpin, T.A. Stich, C.A. Ohlin, Y. Surendranath, D.G. Nocera, W.H. Casey, R.D. Britt, *“Electronic Structure Description of a* $[Co(III)_3Co(IV)O_4]$ *Cluster: A Model for the Paramagnetic Intermediate in Cobalt-Catalyzed Water Oxidation.”*, J. Am. Chem. Soc. 133 (2011) 15444–15452.

[MCG72] E.J. McGuire, *“Photoabsorption cross section of titanium to cobalt.”*, J. Phys. Chem. Sol. 33 (1972) 577–580.

[MCK12] K.P. McKenna, M.J. Wolf, A.L. Shluger, S. Lany, A. Zunger, *“Two-Dimensional Polaronic Behavior in the Binary Oxides m-*HfO_2 *and m-*ZrO_2*.”*, Phys. Rev. Lett. 108 (2012) 116403.

[MED09] R.E. Medjo, B.T. Sendja, J.M. Mane, P.O. Ateba, *“XAS study of the orientation of oriented carbon nanotube films.”*, Phys. Scripta 80 (2009) 055602.

[MIC90] R. Micnas, J. Ranninger, S. Robaszkiewicz, *“Superconductivity in narrow-band systems with local nonretarded attractive interactions.”*, Rev. Mod. Phys. 62 (1990) 113–171.

[MIN10] B. Minaev, *“Environment Friendly Spin-Catalysis for Dioxygen Activation.”*, Chemistry & Chemical Technology 4 (2010) 1–16.

[MIT11] F. Mittendorfer, A. Garhofer, J. Redinger, J. Klimeš, J. Harl, G. Kresse, *“Graphene on Ni(111): Strong interaction and weak adsorption.”*, Phys. Rev. B 84 (2011) 201401.

[MUE08] S. Müller, D. Schmeißer, *“Deposition of reactive and non-reactive metals on titanium dioxide - Chromium and cobalt.”*, 2008 International Students and Young Scientists Workshop “Photonics and Microsystems,” (2008) 53–58.

[MUE10] S. Müller, *“Synchrotron radiation spectroscopy studies of the initial interaction of Chromium and Cobalt with the surface of Titanium Dioxide.”*, BTU Cottbus, 2010.

[MUK12] S. Mukherjee, J.A. Stull, J. Yano, T.C. Stamatatos, K. Pringouri, T.A. Stich, K.A. Abboud, R.D. Britt, V.K. Yachandra, G. Christou, *“Synthetic model of the asymmetric [Mn_3CaO_4] cubane core of the oxygen-evolving complex of photosystem II.”*, Proc. Natl. Acad. Sci. 109 (2012) 2257–2262.

[NAI08] R.R. Nair, P. Blake, A.N. Grigorenko, K.S. Novoselov, T.J. Booth, T. Stauber, N.M.R. Peres, A.K. Geim, *“Fine Structure Constant Defines Visual Transparency of Graphene.”*, Science 320 (2008) 1308–1308.

[NAP08] J.M. Napoles-Duarte, M. Reyes-Reyes, J.L. Ricardo-Chavez, R. Garibay-Alonso, R. Lopez-Sandoval, *“Effect of packing on the cohesive and electronic properties of methanofullerene crystals.”*, Phys. Rev. B 78 (2008) 035425.

[NEG06] H. Negishi, S. Negishi, K. Shimada, T. Narimura, A. Higashiguchi, H. Namatame, M. Taniguchi, K. Kobayashi, K. Sugihara, H. Oshima, *“Electronic structures of HOPG and stage-2 IBr-GIC studied by angle resolved photoemission.”*, J. Phys. Chem. Sol. 67 (2006) 1145–1148.

[NEW12] J. Newman, P.G. Hoertz, C.A. Bonino, J.A. Trainham, *“Review: An Economic Perspective on Liquid Solar Fuels.”*, J. Electrochem. Soc. 159 (2012) A1722–A1729.

[NIC03] K.T. Nicholson, T.K. Minton, S.J. Sibener, *“Temperature-dependent morphological evolution of HOPG graphite upon exposure to hyperthermal atoms.”*, Progress in Organic Coatings 47 (2003) 443–447.

[NOW89] M. Nowak, D. Spiegel, S. Hotta, A. Heeger, P. Pincus, *“Charge storage on a conducting polymer in solution.”*, Macromolecules 22 (1989) 2917–2926.

[OHK08] H.H. Ohkita, S.S. Cook, Y.Y. Astuti, W.W. Duffy, S.S. Tierney, W.W. Zhang, M.M. Heeney, I.I. McCulloch, J.J. Nelson, D.D.C.D. Bradley, J.R.J. Durrant, *“Charge carrier formation in polythiophene/fullerene blend films studied by transient absorption spectroscopy.”*, J. Am. Chem. Soc. 130 (2008) 3030–3042.

[OHN01] M. Ohno, *“Inherent post-collision interaction in spectator Auger-transitions in metals and charge-transfer systems.”*, J. Electron Spectrosc. 120 (2001) 33–45.

[OKA92a] K. Okada, A. Kotani, *“Complementary Roles of Co2p X-Ray Absorption and Photoemission Spectra in CoO.”*, J. Phys. Soc. Jpn. 61 (1992) 449–453.

[OKA92b] K. Okada, A. Kotani, *“Interatomic and Intra-Atomic Configuration Interactions in Core-Level X-ray Photoemission Spectra of Late Transition-Metal Compounds.”*, J. Phys. Soc. Jpn. 61 (1992) 4619–4637.

[OPE08] M. Opel, K.W. Nielsen, S. Bauer, S.T.B. Goennenwein, J.C. Cezar, D. Schmeißer, J. Simon, W. Mader, R. Gross, *“Nanosized superparamagnetic precipitates in cobalt-doped ZnO.”*, Eur. Phys. J. B 63 (2008) 437–444.

[OST00] R. Österbacka, C. An, X. Jiang, Z. Vardeny, *“Two-dimensional electronic excitations in self-assembled conjugated polymer nanocrystals.”*, Science 287 (2000) 839–842.

[OST01] R. Österbacka, C. An, X. Jiang, Z. Vardeny, *“Delocalized polarons in self-assembled poly(3-hexyl thiophene) nanocrystals.”*, Synth. Met. 116 (2001) 317–320.

[OST03] R. Österbacka, M. Wohlgenannt, M. Shkunov, D. Chinn, Z. Vardeny, *“Excitons, polarons, and laser action in poly(p-phenylene vinylene) films.”*, J. Chem. Phys. 118 (2003) 8905–8916.

[PAC08] D. Pacile, M. Papagno, A.F. Rodríguez, M. Grioni, L. Papagno, Ç.Ö. Girit, J.C. Meyer, G.E. Begtrup, A. Zettl, *"Near-edge X-ray absorption fine-structure investigation of graphene."*, Phys. Rev. Lett. 101 (2008) 66806.

[PEI55] R.E. Peierls, *"Quantum theory of solids, Clarendon"*, Oxford, 1955.

[PET98] L. Pettersson, H. Agren, Y. Luo, L. Triguero, *"Benzene adsorbed on Cu(110): Theoretical X-ray absorption, emission and shake calculations."*, Surf. Sci. 408 (1998) 1–20.

[PET08] S.C. Petitto, E.M. Marsh, G.A. Carson, M.A. Langell, *"Cobalt oxide surface chemistry: The interaction of CoO(100), Co_3O_4(110) and Co_3O_4(111) with oxygen and water."*, J. Mol. Catal. A: Chem. 281 (2008) 49–58.

[POZ11] Z.D. Pozun, G. Henkelman, *"Hybrid density functional theory band structure engineering in hematite."*, J. Chem. Phys. 134 (2011) 224706.

[PRE09] A. Preobrajenski, M. Ng, A. Vinogradov, N. Mårtensson, *"Controlling graphene corrugation on lattice-mismatched substrates."*, Phys. Rev. B 78 (2008) 073401.

[PRE10] M. Presselt, M. Baerenklau, R. Roesch, W.J.D. Beenken, E. Runge, S. Shokhovets, H. Hoppe, G. Gobsch, *"Subbandgap absorption in polymer-fullerene solar cells."*, Appl. Phys. Lett. 97 (2010) 253302.

[PSI09] D. Psiachos, S. Mazumdar, *"Correlated-electron description of the photophysics of thin films of π-conjugated polymers."*, Phys. Rev. B 79 (2009) 155106.

[PUT04] R. Puttner, C. Kolczewski, M. Martins, A. Schlachter, G. Snell, M. Sant'Anna, J. Viefhaus, K. Hermann, G. Kaindl, *"The C1s NEXAFS spectrum of benzene below threshold: Rydberg or valence character of the unoccupied σ-type orbitals",* Chem. Phys. Lett. 393 (2004) 361–366.

[QUI08] K.L. Quick, S.S. Ali, R. Arch, C. Xiong, D. Wozniak, L.L. Dugan, *"A carboxyfullerene SOD mimetic improves cognition and extends the lifespan of mice."*, Neurobiol. Aging 29 (2008) 117–128.

[REE11] S.Y. Reece, J.A. Hamel, K. Sung, T.D. Jarvi, A.J. Esswein, J.J.H. Pijpers, D.G. Nocera, *"Wireless Solar Water Splitting Using Silicon-Based Semiconductors and Earth-Abundant Catalysts."*, Science 334 (2011) 645–648.

[REI02] S. Reich, J. Maultzsch, C. Thomsen, P. Ordejón, *"Tight-binding description of graphene."*, Phys. Rev. B 66 (2002) 035412.

[RIE10] C. Riedl, *"Epitaxial Graphene on Silicon Carbide Surfaces: Growth, Characterization, Doping and Hydrogen Intercalation."*, Friedrich-Alexander-Universität Erlangen-Nürnberg, 2010.

[RIS09a] M. Risch, F. Ringleb, V. Khare, P. Chernev, I. Zaharieva, H. Dau, *"Characterisation of a water-oxidizing Co-film by XAFS."*, J. Phys.: Conf. Ser. 190 (2009) 012167.

[RIS09b] M. Risch, V. Khare, I. Zaharieva, L. Gerencser, P. Chernev, H. Dau, *"Cobalt−Oxo Core of a Water-Oxidizing Catalyst Film."*, J. Am. Chem. Soc. 131 (2009) 6936–6937.

[ROB91] J. Robertson, *"Hard amorphous (diamond-like) carbons."*, Prog. Solid St. Chem. 21 (1991) 199–333.

[ROB02] J. Robertson, *"Diamond-like amorphous carbon."*, Mat. Sci. Eng. R 37 (2002) 129–281.

[RUT11] G.M. Rutter, S. Jung, N.N. Klimov, D.B. Newell, N.B. Zhitenev, J.A. Stroscio, *"Microscopic polarization in bilayer graphene."*, Nat. Phys. 7 (2011) 649–655.

[SAI98] R. Saito, G. Dresselhaus, M.S. Dresselhaus, *"Physical Properties of Carbon Nanotube."*, Imperial College Press, 1998.

[SAL88] W. Salaneck, O. Inganas, B. Themans, J.O. Nilsson, B. Sjogren, J.E. Österholm, J.L. Brédas, S. Svensson, *"Thermochromism in Poly(3-Hexylthiophene) in the Solid-State: A Spectroscopic Study of Temperature-Dependent Conformational Defects."*, J. Chem. Phys. 89 (1988) 4613–4619.

[SAR92] N. Sariciftci, L. Smilowitz, A. Heeger, F. Wudl, *"Photoinduced Electron-Transfer From a Conducting Polymer to Buckminsterfullerene."*, Science 258 (1992) 1474–1476.

[SCH03] D. Schmeißer, *"Valence states of poly(3-hexyl-thiophene) as probed by photoelectron spectra at resonant excitation."*, Synth. Met. 138 (2003) 135–140.

[SCH10] D. Schmeißer, S. Schmidt, G. Seibold, G. Cherkashinin, W. Jaegermann, *"Localized Gap States in LiCoO2 and Their Influence on the Transport Properties in Li Ion Batteries."*, ECS Transactions 25 (2010) 37–45.

[SCHU11] B.J. Schultz, C.J. Patridge, V. Lee, C. Jaye, P.S. Lysaght, C. Smith, J. Barnett, D.A. Fischer, D. Prendergast, S. Banerjee, *"Imaging local electronic corrugations and doped regions in graphene."*, Nat. Commun. 2 (2011) 372.

[SCHU12] B.J. Schultz, C. Jaye, P.S. Lysaght, D.A. Fischer, D. Prendergast, S. Banerjee, *"On chemical bonding and electronic structure of graphene–metal contacts."*, Chem. Sci. 4 (2012) 494–502.

[SCHM12] S. Schmidt, D. Schmeißer, *"Electronic structure of cobalt–nickel mixed oxides."*, Solid State Ionics 225 (2012) 737–741.

[SET08] K. Sethuraman, S. Ochiai, K. Kojima, T. Mizutani, *"Performance of poly(3-hexylthiophene) organic field-effect transistors on cross-linked poly(4-vinyl phenol) dielectric layer and solvent effects."*, Appl. Phys. Lett. 92 (2008) 183302.

[SHA05] Y. Shao, Y. Yang, *"Efficient organic heterojunction photovoltaic cells based on triplet materials."*, Adv. Mater. 17 (2005) 2841–2844.

[SHE07] C.X. Sheng, M. Tong, S. Singh, Z.V. Vardeny, *"Experimental determination of the charge/neutral branching ratio η in the photoexcitation of π-conjugated polymers by broadband ultrafast spectroscopy."*, Phys. Rev. B 75 (2007) 085206.

[SIE75] H. Siegbahn, L. Asplund, P. Kelfve, *"The Auger electron spectrum of water vapour."*, Chem. Phys. Lett. 35 (1975) 330–335.

[STO03] J. Stöhr, *"NEXAFS Spectroscopy (Springer Series in Surface Sciences)"*, 2nd ed. Springer, Heidelberg, 2003.

[SU79] W.P. Su, J.R. Schrieffer, A.J. Heeger, *"Solitons in Polyacetylene."*, Phys. Rev. Lett. 42 (1979) 1698–1701.

[SUB02] S. Subbiah, R. Mokaya, *"Transparent thin films and monoliths synthesized from fullerene doped mesoporous silica: evidence for embedded monodispersed C_{60}."*, Chem. Commun. (2002) 92–93.

[SUB12] R. Subbaraman, D. Tripkovic, K.-C. Chang, D. Strmcnik, A.P. Paulikas, P. Hirunsit, M. Chan, J. Greeley, V. Stamenkovic, N.M. Markovic, *"Trends in activity for the water electrolyser reactions on 3d M(Ni,Co,Fe,Mn) hydr(oxy)oxide catalysts."*, Nat. Mater. 11 (2012) 550–557.

[SUR09] Y. Surendranath, M. Dincă, D.G. Nocera, *"Electrolyte-Dependent Electrosynthesis and Activity of Cobalt-Based Water Oxidation Catalysts."*, J. Am. Chem. Soc. 131 (2009) 2615–2620.

[SUR10] Y. Surendranath, M.W. Kanan, D.G. Nocera, *"Mechanistic Studies of the Oxygen Evolution Reaction by a Cobalt-Phosphate Catalyst at Neutral pH."*, J. Am. Chem. Soc. 132 (2010) 16501–16509.

[TAN94] S. Tanuma, C.J. Powell, D.R. Penn, *"Calculations of electron inelastic mean free paths V Data for 14 organic compounds over the 50-2000 eV range."*, Surf. Interface Anal. 21 (1994) 165–176.

[TOU88] G. Tourillon, C. Mahatsekake, C. Andrieu, G. Williams, R. Garrett, W. Braun, *"Electronic-structure and orientation studies of undoped poly-3-alkyl thiophenes electrochemically deposited on Pt as studied by NEXAFS."*, Surf. Sci. 201 (1988) 171–184.

[TUR64] W. Turner, W. Reese, G. Pettit, *"Exciton Absorption and Emission in InP."*, Phys. Rev. 136 (1964) A1467–A1470.

[UMB84] E. Umbach, Z. Hussain, *"Angle-Dependent Changes of Auger Line Shapes from Adsorbed Molecules."*, Phys. Rev. Lett. 52 (1984) 457–460.

[VAN10] M. Vanin, J.J. Mortensen, A.K. Kelkkanen, J.M. Garcia-Lastra, K.S. Thygesen, K.W. Jacobsen, *"Graphene on metals: A van der Waals density functional study."*, Phys. Rev. B 81 (2010) 081408.

[VAR08] A. Varykhalov, J. Sánchez-Barriga, A. Shikin, C. Biswas, E. Vescovo, A. Rybkin, D. Marchenko, O. Rader, *"Electronic and Magnetic Properties of Quasifreestanding Graphene on Ni."*, Phys. Rev. Lett. 101 (2008) 157601.

[VAR12] A. Varykhalov, D. Marchenko, J. Sánchez-Barriga, M. Scholz, B. Verberck, B. Trauzettel, T. Wehling, C. Carbone, O. Rader, *"Intact Dirac Cones at Broken Sublattice Symmetry: Photoemission Study of Graphene on Ni and Co."*, Phys. Rev. X 2 (2012) 041017.

[VARL12] J.B. Varley, A. Janotti, C. Franchini, C.G. Van de Walle, *"Role of self-trapping in luminescence and p-type conductivity of wide-band-gap oxides."*, Phys. Rev. B 85 (2012) 081109.

[WAN05] B. Wang, *"Recent development of non-platinum catalysts for oxygen reduction reaction."*, J Power Sources 152 (2005) 1–15.

[WAT06] B. Watts, L. Thomsen, P. Dastoor, *"Methods in carbon K-edge NEXAFS: Experiment and analysis."*, J. Electron Spectrosc. 151 (2006) 105–120.

[WAT11] B. Watts, S. Swaraj, D. Nordlund, J. Luening, H. Ade, *"Calibrated NEXAFS spectra of common conjugated polymers."*, J. Chem. Phys. 134 (2011) 024702.

[WEI12] W. Wei, T. Jacob, *"Strong charge-transfer excitonic effects in C_4H-type hydrogenated graphene."*, Phys. Rev. B 86 (2012) 165444.

[WEI13] W. Wei, T. Jacob, *"Strong excitonic effects in the optical properties of graphitic carbon nitride g-C_3N_4 from first principles."*, Phys. Rev. B 87 (2013) 085202.

[WOL03] J. Wöllenstein, M. Burgmair, G. Plescher, T. Sulima, J. Hildenbrand, H. Böttner, I. Eisele, *"Cobalt oxide based gas sensors on silicon substrate for operation at low temperatures."*, Sensor. Actuat. B 93 (2003) 442–448.

[XU09] Z. Xu, L.-M. Chen, M.-H. Chen, G. Li, Y. Yang, *"Energy level alignment of poly(3-hexylthiophene): [6,6]-phenyl C-61 butyric acid methyl ester bulk heterojunction."*, Appl. Phys. Lett. 95 (2009) 013301.

[XU13] K. Xu, C. Zeng, Q. Zhang, R. Yan, P. Ye, K. Wang, A.C. Seabaugh, H.G. Xing, J.S. Suehle, C.A. Richter, D.J. Gundlach, N.V. Nguyen, *"Direct Measurement of Dirac Point Energy at the Graphene/Oxide Interface."*, Nano Lett. 13 (2013) 131–136.

[YAM98] T. Yamamoto, D. Komarudin, M. Arai, B.-L. Lee, H. Suganuma, N. Asakawa, Y. Inoue, K. Kubota, S. Sasaki, T. Fukuda, H. Matsuda, *"Extensive Studies on π-Stacking of Poly(3-alkylthiophene-2,5-diyl)s and Poly(4-alkylthiazole-2,5-diyl)s by Optical Spectroscopy, NMR Analysis, Light Scattering Analysis, and X-ray Crystallography."*, J. Am. Chem. Soc. 120 (1998) 2047–2058.

[YAN96] C. Yang, F. Orfino, S. Holdcroft, *"A phenomenological model for predicting thermochromism of regioregular and nonregioregular poly(3-alkylthiophenes)."*, Macromolecules 29 (1996) 6510–6517.

[YAN09] L. Yang, J. Deslippe, C.-H. Park, M. Cohen, S. Louie, *"Excitonic Effects on the Optical Response of Graphene and Bilayer Graphene."*, Phys. Rev. Lett. 103 (2009) 186802.

[YEH85] J. Yeh, I. Lindau, *"Atomic subshell photoionization cross sections and asymmetry parameters: 1 Z 103."*, Atomic Data and Nuclear Data Tables 32 (1985) 1–155.

[YOU10] E.R. Young, D.G. Nocera, V. Bulovic, *"Direct formation of a water oxidation catalyst from thin-film cobalt."*, Energ. Environ. Sci. 3 (2010) 1726–1728.

[ZAK05] T.Y. Zakharian, A. Seryshev, B. Sitharaman, B.E. Gilbert, V. Knight, L.J. Wilson, *"A Fullerene−Paclitaxel Chemotherapeutic: Synthesis, Characterization, and Study of Biological Activity in Tissue Culture."*, J. Am. Chem. Soc. 127 (2005) 12508–12509.

[ZHO07] S.Y. Zhou, G.H. Gweon, A.V. Fedorov, P.N. First, W.A. de Heer, D.H. Lee, F. Guinea, A.H. Castro Neto, A. Lanzara, *"Substrate-induced bandgap opening in epitaxial graphene."*, Nat. Mater. 6 (2007) 770–775.

[ZHU11] X. Zhu, A. Kahn, *"Electronic Structure and Dynamics at Organic Donor/Acceptor Interfaces."*, Mrs Bull. 35 (2011) 443–448.

[ZHU13] H. Zhu, S.J. Paddison, T.A. Zawodzinski Jr, *"The effects of the ligand, central metal, and solvent on the O_2 binding of non-precious metal catalyst model systems: An ab initio study."*, Electrochim. Acta 101 (2013) 293–300.

[ZOO09] A.P. Zoombelt, M. Fonrodona, M.M. Wienk, A.B. Sieval, J.C. Hummelen, R.A.J. Janssen, *"Photovoltaic Performance of an Ultrasmall Band Gap Polymer."*, Org. Lett.,11 (2009) 903–906.

List of Publications

Parts of this Thesis were published in:

[Ric12]	M. Richter, D. Friedrich, and D. Schmeißer, *"Valence and Conduction band states of PCBM as probed by photoelectron spectroscopy at resonant excitation."*, BioNanoScience 2 (2012) 59-65. DOI: 10.1007/s12668-011-0034-1
[Ric13a]	M. Richter, D. Friedrich, D. Schmeißer, *"Interlayer-Exciton mediated three-hole-Auger-decay in the π*–band of Highly Oriented Pyrolytic Graphite."*, Physica E 56 (2014) 441-446. DOI: 10.1016/j.physe.2013.01.015
[Ric13b]	*M. Richter* and D. Schmeißer, *"The Co2p Oxidation State In Co-PI Catalysts"*, ECS Transactions 50(49) (2013) 113-126. DOI: 10.1149/05049.0113ecst
[Ric13c]	M. Richter, I. Paloumpa, D. Friedrich, and D. Schmeißer, *"Multiple Auger Decay At Resonant Photo-Excitation In Carbon Thin Films."*, ECS Transactions 50(20) (2013) 9-21. DOI: 10.1149/05020.0009ecst
[Ric13d]	M. Richter and D. Schmeißer, *"Spin states in Co-PI catalysts."*, Applied Physics Letters 102 (2013) 253904. DOI: 10.1063/1.4811748
[Ric13e]	M. Richter, U. Starke, and D. Schmeißer, *"Multiple Auger processes in Graphene."*, Journal Of Electron Spectroscopy And Related Phenomena 192 (2014) 1-6. DOI: 10.1016/j.elspec.2013.12.009
[Mue12a]	K. Müller, M. Richter, S. Philip, M. Kunst, and D. Schmeißer, *"Excited states in P3HT and P3HT/PCBM blends."*, BioNanoScience 2 (2012) 42-51. DOI: 10.1007/s12668-011-0031-4

Other Publications:

[Frie11] D. Friedrich, K. Henkel, M. Richter, and D. Schmeißer, *"Fullerenol as probed by Synchrotron X-ray Photoemission and Absorption Spectroscopy."*, BioNanoScience 1 (2011) 218-223.
DOI: 10.1007/s12668-011-0025-2

[Mue12b] K. Müller, M. Richter, D. Friedrich, I. Paloumpa, U.I. Kramm, and D. Schmeißer, *"Spectroscopic characterization of Cobalt-Phthalocyanine electrocatalysts for fuel cell applications."*, Solid State Ionics 216 (2012) 78-82.
DOI: 10.1016/j.ssi.2011.12.013

[Fis13] C. B. Fischer, M. Rohrbeck, S. Wehner, M. Richter, and D. Schmeißer, *"Interlayer formation of diamond-like carbon coatings on industrial polyethylene: thickness dependent surface characterization by SEM, AFM and NEXAFS."*, Applied Surface Science 271 (2013) 381- 389.
DOI: 10.1016/j.apsusc.2013.01.210

[Hae13] J. Haeberle, M. Richter, Z. Galazka, C. Janowitz, and D. Schmeißer, *"Resonant Photoemission at the O1s threshold to characterize* In_2O_3 *single crystals."*, Thin Solid Films, accepted.
DOI: 10.1016/j.tsf.2013.03.036

[Stae13] M. Städter, K. Müller, F. Rachow, M. Richter, and D. Schmeißer, *"Ambient pressure thermal desorption spectroscopy (AP-TDS) of* NiO/SiO_2 *catalysts."*,
Environmental Earth Sciences 70(8) (2013) 3779-3784.
DOI: 10.1007/s12665-013-2835-8

Conference and Meeting contributions:

DPG Spring Meeting, Dresden (Germany), 22.03. – 27.03.2009

"Temperature dependence of organic solar cell parameters.", M. Richter, K. Müller, S. Philip, I. Paloumpa, K. Henkel, and D. Schmeißer. Poster SYOP 4.2.Verhandlungen der DPG (VI) 44, 5/2009 (2009) 671, ISSN 0420-0195.

4. AFM-Workshop, Dresden-Moritzburg (Germany), 08.05. – 09.05.2009

"AFM investigations of ferroelectric and organic materials.", D. Schmeißer, D. Friedrich, K. Müller, I. Paloumpa, M. Richter, and M. Städter. Poster.

E-MRS 2009 Spring Meeting, Strasbourg (France), 08.06. – 12.06.2009

"Influence of preparation parameters on the performance of P3HT/PCBM solar cells.", K. Müller, M. Richter, S. Philip, I. Paloumpa, K. Henkel, and D. Schmeißer. Poster AP1.19.

First Joint BERII and BESSY II Users' Meeting, Berlin-Adlershof (Germany), 12.11. – 13.11.2009

"Study of P3HT, PCBM and C_{60} based films by NEXAFS.", M. Richter, D. Friedrich, J. Klocek, and D. Schmeißer. Poster.

DPG Spring Meeting, Regensburg (Germany), 21.03. – 26.03.2010

"Study of P3HT/PCBM based films by NEXAFS.", M. Richter, D. Friedrich, S. Philip, I. Paloumpa, K. Müller, and D. Schmeißer. Talk DF 7.4. Verhandlungen der DPG (VI) 45, 3/2010 (2010) 194, ISSN 0420-0195.

"Performance of organic solar cells with a ferroelectric component.", K. Kachel, M. Richter, S. Philip, I. Paloumpa, K. Müller, and D. Schmeißer. Poster CPP 27.6. Verhandlungen der DPG (VI) 45, 3/2010 (2010) 153, ISSN 0420-0195.

"Spectroscopic investigations of P3HT/PCBM films for organic BHJ solar cells.", S. Philip, M. Richter, D. Friedrich, I. Paloumpa, K. Müller, and D. Schmeißer. Poster CPP 27.7. Verhandlungen der DPG (VI) 45, 3/2010 (2010) 153, ISSN 0420-0195.

10. Schwarzheider Kunstoffkolloquium des Kunststoffverbundes Brandenburg-Berlin (KuVBB), Schwarzheide (Germany), 08.09. – 09.09.2010

"Electrical and spectroscopic characterization of organic BJH solar cells.", M. Richter, K. Müller, and D. Schmeißer. Poster.

"Optimization of BJH organic solar cell parameters.", S. Philip, M. Richter, I. Paloumpa, K. Müller, and D Schmeißer. Poster.

Second Joint BERII and BESSY II Users' Meeting, Berlin-Adlershof (Germany), 09.12. – 10.12.2010

"Latest activities at our chair (Polyimide, P3HT:PCBM, (Co,Ni)-oxides and ALD).", M. Richter, D. Friedrich, M. Michling, S. Schmidt, M. Tallarida, and D. Schmeißer. Poster.

DPG Spring Meeting, Dresden (Germany), 13.03. – 18.03.2011

"Investigation of new Catalysts for PEM Fuel Cells.", R. Mbua, U. Kramm, K. Müller, M. Richter, K. Henkel, I. Paloumpa, and D. Schmeißer. Poster O 60.119. Verhandlungen der DPG (VI) 46, 1/2011 (2011) 483, ISSN 0420-0195.

"ResPES to determine the abundance of aromatic carbon bonds in a-C films.", D. Hoffmannbeck, M. Richter, M. Städter, I. Paloumpa, K. Henkel, and D. Schmeißer. Poster O 60.123. Verhandlungen der DPG (VI) 46, 1/2011 (2011) 483, ISSN 0420-0195.

"Electronic structure and optical properties of P3HT - Evidence of 2D-Polarons in P3HT.", M. Richter and D. Schmeißer. Talk DS 64.3. Verhandlungen der DPG (VI) 46, 1/2011 (2011) 311, ISSN 0420-0195.

E-MRS 2011 Spring Meeting, Nice (France), 09.05. – 13.05.2011

"2D-Polarons in the electronic structure of P3HT.", M. Richter and D. Schmeißer. Poster S P7_15.

German Polish Conference on Crystal Growth (GPCCG) 2011, Frankfurt (Oder) / Slubice (Germany / Poland), 14.03. – 18.03.2011

"Ferroelectric layers in organic solar cells.", K. Müller, M. Richter, S. Philip, K. Kachel, K. Henkel, I. Paloumpa, and D. Schmeißer. Invited Talk.

3rd Bilateral Estonian-German Workshop, Cottbus (Germany), 13.06. – 15.06.2011

"2D-Polarons in the electronic structure of P3HT formed by interface doping.",
M. Richter and D. Schmeißer. Poster.

12th European Conference on Organized Films (ECOF 12), Sheffield (GB), 17.07. – 20.07.2011

"Fullerene and its derivatives as probed by X-ray Absorption Spectroscopy.",
D. Friedrich, K. Henkel, M. Richter, and D. Schmeißer. Poster P34.

"2D-Polarons in the electronic structure of rr-P3HT formed by interface doping.",
M. Richter, D. Friedrich, and D. Schmeißer. Talk O30.

28th European Conference on Surface Science (ECOSS-28), Wrocław (Poland), 28.08. – 02.09.2011

"ResPES to determine the abundance of aromatic carbon bonds in a-C films.",
D. Friedrich, M. Michling, M. Richter, and D. Schmeißer. Poster.

"Resonant Photoemission at the carbon K-edge of rr-P3HT.",
M. Richter, D. Friedrich, and D. Schmeißer. Talk.

8th European Congress of Chemical Engineering (ECCE), Berlin (Germany), 25.09. – 29.09.2011

"Spectroscopic characterization of Cobalt-Phthalocyanine electrocatalysts.",
K. Müller, R. Mbua, I. Paloumpa, M. Richter, U. Kramm, and D. Schmeißer.
Poster P12.14.

Third Joint BERII and BESSY II Users' Meeting, Berlin-Adlershof (Germany), 30.11. – 02.12.2011

"HOPG and Graphene as probed by Synchrotron X-ray photoemission and Absorption Spectroscopy.", M. Richter, D. Friedrich, G. Beuckert, I. Paloumpa, M. Kraatz, and D. Schmeißer. Poster.

DPG Spring Meeting, Berlin (Germany), 25.03. – 30.03.2012

"Study of excited states and a model for Exciton-Polaron interaction in P3HT", S. Philip, K. Müller, M. Richter, M. Kunst, and D. Schmeißer. Poster DS 44.31.

"3h-Auger decay in the π-band of HOPG.", M. Richter, D. Friedrich, and D. Schmeißer. Talk DS 35.4.

"Diamond-Like Carbon Coatings on Selected Plastic Materials.", C.B. Fischer, M. Rohrbeck, S. Wehner, M. Richter, and D. Schmeißer. Talk O 66.9.

"Diamond-Like Carbon Coatings on Industrial Polyethylene Surfaces", M. Rohrbeck, C.B. Fischer, S. Wehner, M. Richter, and D. Schmeißer. Poster O 35.28.

E-MRS 2012 Spring Meeting, Strasbourg (France), 14.05. – 18.05.2012

"Three-Hole-Auger in the π–band of carbon thin films.", M.Richter, and D. Schmeißer. Talk R8 9.

"Excited states in P3HT and model for Exciton-Polaron interaction", K. Müller, M. Richter, S. Philip, M. Kunst, and D. Schmeißer. Poster.

Frontiers in Electronic Materials: Correlation Effects and Memristive Phenomena, Aachen (Germany), 17.06. – 20.06.2012

"Intrinsic defects in TiO2 to explain resistive switching devices.", D. Schmeißer, M. Richter, and M. Tallarida. Nanosession.

Annual World Conference on Carbon 2012 (Carbon 2012), Krakow (Poland), 17.06. – 22.06.2012

"Improving selected plastic materials with diamond-like carbon (DLC) coatings.", C. B. Fischer, M. Rohrbeck, S. Wehner, M. Richter, and D. Schmeißer. Talk ID 343.

12. Interantionale Konferenz "Electronic spectroscopy and structure" (ICESS 2012), Saint-Malo (France), 16.09. – 21.09.2012

"Defect Exciton induced multiple Auger decay.", M. Richter, M. Städter, and D. Schmeißer. Poster SM-3-PO-RIC-01.

"The electronic structure of Ga2O3 and In2O3 transparent conductive oxides.", M. Richter, M. Michling, J. Haeberle, Z. Galaazka, and D. Schmeißer. Poster SM-3-PO-SCH-01.

Pacific Rim Meeting on Electrochemical and Solid-State Science (PRiME 2012) 222nd Meeting of ECS – The Electrochemical Society, Honolulu (Hawaii-USA), 7.10. – 12.10.2012

"Multiple Auger decay at resonant photo-excitation in carbon thin films.", M. Richter, D. Friedrich, and D. Schmeißer. Poster.

"The Co2p oxidation state in Co-PI catalysts.", M. Richter, and D. Schmeißer. Poster.

4. Internationales Symposium "Transparent Conductive Materials" (TCM 2012), Hersonissos (Greece), 21.10. – 26.10.2012

"Defects in the electronic structure of Ga2O3 and In2O3 transparent conductive oxides.", D. Schmeißer, and M. Richter. Talk ID 112.

4th Joint BER II and BESSY II Users' Meeting, Berlin-Adlershof (Germany), 12.12. – 14.12.2012

"The spin and oxidation state in Co-PI catalysts.", M. Richter, and D. Schmeißer. Poster.

"Multiple Auger Decay at resonant photo-excitation in carbon thin films.", M. Richter, M. Städter, I. Paloumpa, D. Friedrich, and D. Schmeißer. Poster.

"Interlayer formation of hard Diamond-Like Carbon Coatings on soft Polyethylene material.", C.B. Fischer, M. Rohrbeck, S. Wehner, M. Richter, M. Städter, and D. Schmeißer. Poster.

DPG Spring Meeting, Regensburg (Germany), 10.03 – 15.03.2013

"Multiple Auger Decay at resonant photo-excitation in carbon thin films.", M. Richter, M. Städter, I. Paloumpa, and D. Schmeißer. Talk HL 52.6.

"The Co2p spin and oxidation state in Co-PI catalysts.", M. Richter, and D. Schmeißer. Talk DS 35.9.

"Fano-Profiles in HOPG and Graphene flakes.", M. Städter, M. Richter, and D. Schmeißer. Talk HL 52.5.

"Resonant Photoemission at the O1s threshold to characterize In2O3 single crystals.", J. Haeberle, M. Richter, D. Schmeißer, Z. Galazka, and C. Janowitz. Poster MM 15.57.

"Interlayer formation of Diamond-Like Carbon Coatings on Polyethylene Plastic Material.", C. B. Fischer, M. Rohrbeck, S. Wehner, M. Richter, M. Städter, and D. Schmeißer. Talk O33.4.

Graphene Week 2013, Chemnitz (Germany), 02.06. – 07.06.2013

"Metal imposed localization of free carriers in Graphene.", M. Richter, M. Städter, U. Starke, and D. Schmeißer. Poster GW2013-61.

"Fano resonances in multilayer Graphene flakes.", M. Städter, M. Richter, and D. Schmeißer. Poster GW2013-316.

"Graphene films on insulating oxidic substrates: PES and Raman studies.", S. Brizzi, D. Friedrich, M. Richter, K. Henkel, M. Tallarida, and D. Schmeißer. Poster GW2013-314.

International Symposium "Flexible Electronics", Erlangen (Germany), 19.06. – 21.06.2013

"Multiple Auger processes to identify pure Graphene.", M. Richter, M. Städter, U. Starke, and D. Schmeißer, Poster (accepted).

"Resonant Photoemission to characterize In2O3 single crystals.", J. Haeberle, M. Richter, and D. Schmeißer, Poster (accepted).

20th International Conference on Electronic Properties of Two-Dimensional Systems (EP2DS-20)", Wrocław (Poland), 01.07. – 05.07.2013

"Multiple Auger processes in Graphene.", M. Richter, M. Städter, U. Starke, and D. Schmeißer. Poster (accepted).

International Conference on Diamond and Carbon Materials,
Riva del Garda (Italy), 02.09. – 05.09.2013

"Interlayer and substrate screening in Graphene as revealed by resPES.", M. Richter, M. Städter, U. Starke, and D. Schmeißer. Talk (accepted).

European Conference on Materials & Technologies for Sustainable Growth (Eco MaTECH), Bled (Slovenia), 19.09. – 21.09.2013

"Electrode interface engineering and analysis using in-situ ALD and SR based spectroscopies.", D. Schmeißer, M. Tallarida, C. Das, M. Richter, and U.I. Kramm. Invited Talk IN-TH11.

Frequently used abbreviations and symbols

AFM	Atomic Force Microscopy
AO-2	Graphene flakes type AO-2
AO-4	Graphene flakes type AO-4
CB(M)	Conduction Band (Minimum)
CFS	Constant Final State
CIS	Constant Initial State
Co-PI	Cobalt based OER Catalyst
CT	Charge Transfer
DOS	Density Of States
EXAFS	Extended X-ray Absorption Fine Structure
FWHM	Full Width at Half Maximum
HOMO	Highest Occupied Molecular Orbital
HOPG	Highly Ordered Pyrolytic Graphite
HS	High Spin
LS	Low Spin
LUMO	Lowest Unoccupied Molecular Orbital
MCC	Molecular Cobaltate Cluster
MCP	Multi Channel Plate
ML	Mono Layer
NEXAFS	Near Edge X-ray Absorption Fine Structure
OER	Oxygen Evolution Reaction
OFET	Organic Field Effect Transistors
P3HT	Poly(3-hexylthiophene-2,5-diyl)
PCBM	Phenyl-C61-butyric acid methyl ester
PCI	Post Collision Interaction
pDOS	partial Density Of States
PES	Photoelectron Spectroscopy
PEY	Partial Electron Yield
resPES	resonant Photoemission
RIXS	Resonant Inelastic X-ray Scattering
rr-P3HT	regioregular-P3HT
rra-P3HT	regiorandom-P3HT
SEO	Secondary Electron Onset
SR-PES	Synchrotron Radiation Photoemission
STE	Self-Trapped Electron
STH	Self-Trapped Hole
STX	Self-Trapped Exciton
TEY	Total Electron Yield
TFY	Total Fluorescence Yield
TM	Transition Metal
VB(M)	Valence Band (Minimum)
XAS	X-ray Absorption Spectroscopy
XPS	X-ray Photoemission Spectroscopy
XRD	X-ray Diffraction

Curriculum Vitae

Since October 2009	Ph.D. student and Academic assistant, Chair of Applied Physics/Sensors, BTU Cottbus
September 2008 to October 2009	Diploma student, Chair of Applied Physics/Sensors, BTU Cottbus
August 2007 to September 2007	Internship at IHP GmbH Frankfurt/Oder, glucose sensor project
October 2004 to October 2009	Regular study course of Physics, BTU Cottbus, finished with degree Diplom-Physiker
August 2003 to May 2004	Civil Service
June 2003	Abitur at the protestant secondary school "Johanneum" in Hoyerswerda

Erklärung

Hiermit versichere ich, dass ich die vorliegende Arbeit selbständig und ohne unerlaubte Hilfsmittel angefertigt habe. Alle verwendeten Quellen habe ich angegeben.

Cottbus im Juni 2013

Acknowledgements

First of all I would like to acknowledge my supervisor Prof. Dr. Dieter Schmeißer, who gave me the possibility to work on this wonderful topic, for his useful hints and excellent advices, for frequent discussions, and for the opportunity of the participation in a lot of conferences and workshops around the globe.

Secondly, I greatly like to thank Prof. Marcus Bär and Prof. Ulrich Starke for their readiness to act as referees.

Below, I like to acknowledge my friends, my former, and my present colleagues:

- Many thanks to an all long good comrade and BESSY buddy Stephan Schmidt †.
- I thank Matthias Städter for the long MONSTER discussions about the four letters.
- Beamline "minion" and lost in sun Daniel Friedrich as a good friend and BESSY instructor.
- Marcel Michling for (w)hole multiple hole discussions.
- Proposal writer and inspector Dr. Karsten Henkel. Thank you a lot for fruitful discussions and critical readings of my work.
- Jörg Haeberle for the discussions on small trapped rusted spirits.
- Talkative and one hour early but on the time Ioanna Paloumpa for helping and giving wonderful advises.
- Chittaranjan Das, Sakeb Hasan Choudhury, and Simone Maria Brizzi for quality balcony time and multiple somethings.
- Fabian Rachow for being a very good friend all these years.
- Shine Philip for discussions, help, and as a very good friend.
- Bite the apple man Dr. Massimo Tallarida for attending nice conferences together. Aloha!
- Sebastian Müller as the SPECS guy who you can call when BESSY is broken again.
- Guido Beuckert for the grandiose support and for keeping everything running.
- Dr. Klaus Müller for discussions and critical readings.
- Dr. Ulrike Kramm for discussions and help in the electrochemical way of life.

- Our secretaries: Karla Kersten, Susanne Masch, Angelika Breu, and Annette Kallweit for the all-round carefree package.
- Dr. Patrick Hoffmann for the excellent support at the beamline at BESSY II in my early days.
- Dr. Jolanta Klocek, Dr. Krzysztof Kolanek, David Hoffmannbeck, and Carola Schwiertz for being very nice colleagues.
- And of course the BESSY staff for helping even in the darkest hours.

I like to thank the following people for supplying samples or providing me with measurement data of my samples:

- Prof. Dr. Ulrich Starke (MPI Stuttgart) for the preparation and supply of the ML Graphene on Ni(111) and QFBLG on SiC.
- Prof. Dr. Marcus Bär and Dr. Regan Wilks (HZB) for the RIXS measurements on P3HT.
- Daniel Friedrich (BTUC) for his measurements on HOPG.
- Mathias Kappa (BTUC) for XRD measurements of the organic semiconductors.
- Shine Philip (BTUC) for UV-Vis on P3HT and PCBM.

In addition I like to thank the German Research Foundation (DFG) for financial support within priority program SPP 1459 (Schm 745/23-1).

And my parents for supporting me all these years, for giving me a place to relax and making it possible for me to study in Cottbus.